

596

Price 596 SAI
T&MSS
LIBRARY

SANDIA REPORT SAND84-0860 • Unlimited Release • UC-70
Printed February 1985

Preliminary Characterization of the Petrologic, Bulk, and Mechanical Properties of a Lithophysal Zone Within the Topopah Spring Member of the Paintbrush Tuff

R. H. Price, F. B. Nimick, J. R. Connolly, K. Keil,
B. M. Schwartz, S. J. Spence

Prepared by
Sandia National Laboratories
Albuquerque, New Mexico 87185 and Livermore, California 94550
for the United States Department of Energy
under Contract DE-AC04-76DP00789

Issued by Sandia National Laboratories, operated for the United States Department of Energy by Sandia Corporation.

NOTICE: This report was prepared as an account of work sponsored by an agency of the United States Government. Neither the United States Government nor any agency thereof, nor any of their employees, nor any of their contractors, subcontractors, or their employees, makes any warranty, express or implied, or assumes any legal liability or responsibility for the accuracy, completeness, or usefulness of any information, apparatus, product, or process disclosed, or represents that its use would not infringe privately owned rights. Reference herein to any specific commercial product, process, or service by trade name, trademark, manufacturer, or otherwise, does not necessarily constitute or imply its endorsement, recommendation, or favoring by the United States Government, any agency thereof or any of their contractors or subcontractors. The views and opinions expressed herein do not necessarily state or reflect those of the United States Government, any agency thereof or any of their contractors or subcontractors.

Printed in the United States of America
Available from
National Technical Information Service
U.S. Department of Commerce
5285 Port Royal Road
Springfield, VA 22161

NTIS price codes
Printed copy: A06
Microfiche copy: A01

SAND84-0860
Unlimited Release
Printed February 1985

*Preliminary Characterization of the
Petrologic, Bulk, and Mechanical Properties of a
Lithophysal Zone Within the
Topopah Spring Member of the Paintbrush Tuff*

R. H. Price¹, F. B. Nimick², J. R. Connolly³, K. Kell³,
B. M. Schwartz², and S. J. Spence¹

¹ Geomechanics Division,
Sandia National Laboratories, Albuquerque, NM 87185

² Geotechnical Projects Division,
Sandia National Laboratories, Albuquerque, NM 87185

³ Department of Geology, Institute of Meteoritics,
University of New Mexico, Albuquerque, NM 87131

**SAI
T&MSS
LIBRARY**

ABSTRACT

Ten large samples of lithophysal tuff were studied as part of the nuclear waste repository project at Yucca Mountain in southern Nevada. Macroscopic and microscopic examination led to division of the tuff into three components: (1) a very fine-grained, relatively nonporous, feldspar- and cristobalite-rich matrix, and (2) a coarser, more porous, feldspar- and tridymite-rich vapor-phase-altered material usually found encircling (3) lithophysae, which are cavities often lined with tridymite and occasionally contain carbonate-rich fillings. Results from mechanical tests provided compressive strengths which are lower, and Young's moduli which are higher, than values predicted from effective porosity.

Contents

	Page
INTRODUCTION	7
Sample Description	8
PETROLOGIC PROPERTIES	8
Petrography	9
X-Ray Powder Diffraction	11
Microanalysis	13
Relevance to Analysis of Mechanical Test Results	18
MODAL ANALYSIS	19
Point Counting	19
Planimetry	20
BULK PROPERTIES	21
Discussion	21
Relevance to Analysis of Mechanical Test Results	22
MECHANICAL PROPERTIES	23
Experimental Techniques	23
Experimental Results	24
Discussion	25

CONCLUSIONS	29
REFERENCES	31
TABLES	35
FIGURES	42
APPENDIX A	58
APPENDIX B	72
APPENDIX C	74
APPENDIX D	77
DISTRIBUTION LIST	105

Tables

	Page
Table 1. Symbols, Abbreviations, Definitions, and Units	35
Table 2. Volume Fraction Results of Point Counting Study	37
Table 3. Volume Fraction Results of Planimetry Study	37
Table 4. Bulk Properties of Lithophysal Samples	38
Table 5. Effect of Grain Density Variation on Calculated Properties	39
Table 6. Mechanical Properties of Lithophysal Topopah Spring Tuff	40
Table 7. Relative Proportions of Porosity from the Three Material Components .	41

Figures

	Page
Figure 1. Location map of the Nevada Test Site, Yucca Mountain, and Busted Butte.	42
Figure 2. Stratigraphy of Yucca Mountain	43
Figure 3. Measured section of the tuffs at the sample outcrop on the southeast flank of Busted Butte.	44
Figure 4. Photomicrograph of devitrified shard matrix, showing strong preferred orientation and deformation, indicative of moderate to dense welding. Sample 2a-1; plane polarized, transmitted light.	45
Figure 5. Photomicrograph of polished thin section of lithophysal tuff, showing a central lithophysa (L) with a rim of vapor-deposited tridymite (T), a zone of vapor-phase alteration (A) and darker devitrified shard matrix (M). Note the abundant porosity in the vapor-phase-altered matrix and deformation of shard matrix around the lithophysa and altered zone. Sample 1B-1; plane polarized, transmitted light.	46
Figure 6. Hand specimen of lithophysal tuff from Busted Butte, showing macroscopic appearance of lithophysae.	47
Figure 7. SEM secondary electron image of a polished section of the vapor-phase-altered matrix around a lithophysa. Darker areas are pores. Sample 8F-1.	48
Figure 8. SEM secondary electron image of a polished section of devitrified matrix. Note absence of porosity in the 5 μ m range relative to Figure 7. Sample 8F-1.	48
Figure 9. Photomicrographs of devitrified matrix. [A] Relict shard texture and deformation around rigid feldspar phenocryst (F). Sample 8A-1. Plane polarized, transmitted light. [B] Axiolitic devitrification of shards and local spherulite development in same area as A. Sample 8A-1. Crossed polarizers, transmitted light.	49
Figure 10. Photomicrographs showing types of crystallization in lithophysal tuff. Light area on left is vapor-phase-altered matrix around a lithophysa. Darker area is devitrified shard matrix. Note presence of vapor phase altered "lenses" within the devitrified matrix. Sample 1D-1. [A] Plane polarized, transmitted light. [B] Crossed polarizers, transmitted light.	50

Figure 11. Photomicrograph of vapor-phase-altered matrix, showing vapor-deposited tridymite (T) around a cavity rim and in pores in altered material. Sample 1D-1. Plane polarized, transmitted light.	51
Figure 12. Vapor-deposited tridymite in lithophysal tuff from 153.8 m (504.6 ft) depth in drill hole USW G-1. SEM secondary electron images of the wall of a lithophysal cavity.	52
Figure 13. Photomicrographs of surface-deposited fill material in lithophysal cavity including coarsely crystalline (Cc) and finely crystalline (Cf) calcite, and opal CT (O). Sample 2A-1. [A] Plane polarized, transmitted light. [B] Crossed polarizers, transmitted light.	53
Figure 14. Diagram of mechanical property test apparatus, including the relative size and location of the sample, and the location of the data acquisition devices.	54
Figure 15. A plot of ultimate stress as a function of effective porosity for both the nonlithophysal and lithophysal tuff.	55
Figure 16. A plot of Young's modulus as a function of effective porosity for both the nonlithophysal and lithophysal tuff.	56
Figure 17. A plot of Poisson's ratio as a function of effective porosity for both the nonlithophysal and lithophysal tuff.	57

INTRODUCTION

Yucca Mountain, located near the southwest margin of the Nevada Test Site (NTS) in southern Nevada, is being evaluated as a potential site for underground disposal of nuclear wastes. Yucca Mountain primarily consists of layered volcanic tuff (Bish et al., 1981). At present, physical, thermal, and mechanical properties of rocks from the Topopah Spring Member of the Paintbrush Tuff are being determined as part of the Nevada Nuclear Waste Storage Investigations (NNWSI) Project, which is administered by the Nevada Operations Office of the U.S. Department of Energy. The rocks studied here are from a section of the Topopah Spring Member informally known as the upper lithophysal zone, and were taken from an outcrop on Busted Butte. Figure 1 shows the geographic locations of NTS, Yucca Mountain, and Busted Butte; and Figure 2 the stratigraphic setting of the Topopah Spring Member.

As shown in Figure 2, the average thickness of rock between the proposed repository horizon and the upper lithophysal zone is large. The relationship of the present study to an analysis of the suitability of the proposed repository horizon for waste disposal is the potential effect on repository design. The tuff units at Yucca Mountain generally dip to the east (Scott et. al., 1983). If welded tuff containing a high percentage of lithophysae, such as the zone discussed in this report, is determined to present problems in mineability or ground support, then the area available for waste emplacement in a horizontal repository design will be limited to the east by the eastward-dipping lithophysae-rich zone.

The petrology/mineralogy and bulk properties of samples of lithophysal tuff were studied and then the samples were tested in deformation experiments. As mentioned above, the mechanical property data contained in this report will ultimately be used to aid in assessing mineability and stability of underground openings in the Topopah Spring Member, and to evaluate predicted near- and far-field responses to the presence of a repository within the unit. In earlier analyses of the mechanical data from experiments on Yucca Mountain silicic tuffs (Olsson and Jones, 1980; Price, 1983), it became apparent that bulk properties (specifically porosity and average grain density) and mineralogy (especially clay and zeolite content) are dominant rock characteristics affecting mechanical properties (e.g., failure strength and elastic moduli). Mineralogy and porosity data also may be useful in the interpretation and application of thermal and hydrologic properties in the site evaluation process.

All symbols and abbreviations used in this report are listed in Table 1. The terms are defined, conventions explained, and standard units assigned.

Sample Description

Rocks for this study were collected as large (up to 6 m³), irregular blocks from an outcrop on the southeastern flank of Busted Butte, in the southwest corner of NTS, just east of the southern end of Yucca Mountain (Figure 1). The outcrop is located very close to north latitude 36°46'19", west longitude 116°25'28". Figure 3 summarizes a measured section of the tuff exposures at the sample location.

Cylindrical samples with diameters of 305 mm (12 in) were cored from the large blocks. These samples were then cut and machined to right-circular cylinders 266.7 ± 0.25 mm (10.5 ± 0.10 in) in diameter and 533.4 ± 2.0 mm (21.0 ± 0.080 in) in length. Pieces cut from the sample ends were used in the mineralogy and bulk property studies, and the finished cylinders were the mechanical test specimens.

Macroscopically, samples from the upper lithophysal zone consist of three components. Large lithophysae (L), which are cavities often lined with tridymite and occasionally with carbonate-rich fillings, are present throughout the unit and are the distinctive feature for which the zone is named. Surrounding the lithophysae are gray regions of varying size, henceforth called vapor-phase-altered material (A). Lithophysae and altered regions are enclosed in the third component, a fine-grained matrix (M) identifiable by its darker, generally purple or reddish-brown color. Small patches of the altered material also occur in the matrix without accompanying lithophysae.

PETROLOGIC PROPERTIES

A detailed study of the mineralogy and petrology of the lithophysae-bearing material was undertaken for a number of reasons. The most general reason was to ensure that the material used for the mechanical test samples, collected from a surface outcrop, had not been altered significantly, and thus, would not be different from equivalent material occurring underground. In addition, characterization of microscopic fabrics, porosity size and distribution, and general mineralogy provides data that aid in the interpretation of mechanical test results. The petrologic information also adds to the data base pertinent to a comparison of the Topopah Spring Member with the Grouse Canyon Member of the

Belted Range Tuff (Connolly et. al., 1983; Connolly and Keil, in prep.), which is exposed within G-Tunnel in the north central region of the Nevada Test Site (Figure 1). Such a comparison is made as part of a discussion of applicability of *in situ* mechanical test data taken in the Grouse Canyon Member to the planning of similar tests in the Topopah Spring Member.

Petrography

Nineteen polished thin sections were prepared from ten samples taken from the ends of the large diameter cores. The following discussion summarizes petrographic data for these sections, obtained from examination using a petrographic microscope. For the purpose of this discussion, lithophysae are taken to include only the central void (lithophysal cavity) and any vapor or groundwater deposited material within the cavity.

Welding : Welding is generally moderate to dense, based on petrographic criteria outlined in Carroll, Caporuscio, and Bish (1981). Shard outlines show notable preferred orientation, tight apical angles, and deformation around rigid phenocrysts and lithic fragments, indicative of a high degree of welding compaction (Figure 4). Local deformation of the matrix around lithophysae and associated altered regions implies high vapor pressures within these regions during formation, and that the matrix was not completely rigid during this vapor phase activity (Figure 5). Distortion of the matrix fabric around lithophysae is generally less than would be expected from cavity sizes, indicating that, although locally high vapor pressures existed, diffusion through the rock matrix did occur.

Porosity : At least four size classes of pores are evident in these samples:

1. Large lithophysal cavities. Size range is from a few millimeters to several centimeters (Figure 6).
2. Small pores in the vapor-phase-altered zones around lithophysae and in lensoid areas in the matrix. These pores are generally under 0.2 mm (0.01 in) in diameter, are largest and most numerous around lithophysae, and are locally partly to completely filled with vapor deposited tridymite (Figures 5 and 6).
3. 1-5 μm intergranular pores in vapor-phase-altered zones around lithophysae (Figure 7).
4. Submicroscopic intergranular pores in the devitrified matrix. These are probably submicrometer in size (Figure 8).

Crystallization/Devitrification : All samples are holocrystalline, although this crystallization is locally on a very fine scale, with individual crystals much less than 5 μm in size. Several types or styles of crystallization are evident:

1. **Axiolitic crystallization (Figure 9).** Generally very fine-scale shard replacement. Pumice fiamme are replaced locally, although fiamme (elongate dark lenticles formed by collapse of pumice fragments during welding) are rare in these samples. This type of devitrification only rarely crosses shard boundaries, allowing recognition of original forms. A reddish-brown color, due to a disseminated Fe_2O_3 phase, is characteristic.
2. **Spherulitic crystallization.** Areas of fine spherulitic crystallization, showing reddish-brown color, are common in the matrix (Figure 9B). Spherulites tend to cross shard boundaries, and tend to be best developed in "pressure shadows" around rigid phenocrysts and where shards are very tightly compressed. Areas of coarse spherulitic crystallization are confined to zones of vapor phase crystallization, are gradational with more equigranular vapor phase crystallization, and tend to be most well-developed around lithophysae.
3. **Vapor phase crystallization.** Equigranular to spherulitic crystallization of generally coarser alkali feldspar, tridymite, and quartz (maximum 50 μm (0.002 in)) aggregates occurs most prominently around lithophysae as zones from a few millimeters to a few centimeters thick, and as small lensoid patches in the matrix (Figure 10). These zones are gray (colorless in thin section) and apparently do not contain the disseminated Fe_2O_3 characteristic of the devitrified shard matrix. Vapor phase crystallization characteristically destroys shard outlines, and gradational contacts with the matrix indicate that vapor phase crystallization followed the devitrification discussed above.
4. **Vapor Deposited Material.** Tridymite occurs most abundantly in small pores in vapor-phase-altered zones around lithophysae and lining lithophysal cavities (Figures 11 and 12). It is also present locally in minor amounts in lensoid vapor phase altered zones in the matrix. Different sections show variable amounts of tridymite. It is impossible to determine on what scale this variation occurs and whether or not the sections may be representative of the entire length of core. Sections made from cores 3A, 8C, 8E, and 8F contain abundant pore-filling tridymite, whereas sections from cores 1B, 1D, 2A, 8A, 8B, and 8D contain less tridymite.
5. **Surface deposited fill.** Some lithophysal cavities are partly filled by dirty to well-crystallized carbonate, opaline silica and argillaceous material (Figure 13). This

filling apparently is due to short-term precipitation and shallow infiltration of rain water followed by local evaporation under arid climate conditions, which typically produces caliche in the upper few meters of desert soil horizons.

Phenocrysts : Modal phenocryst percentages do not exceed 5 percent in any of the samples. Alkali feldspar and plagioclase are dominant; quartz is rare. Opaque phases include magnetite, ilmenite, and secondary (?) hematite. Dark brown to almost opaque biotite is present in most sections. A honey-brown to dark brown ubiquitous minor phase optically resembling allanite is Ti-rich chevkinite, as indicated by electron microprobe analyses. A few hornblende and clinopyroxene grains are present in some sections.

The phenocrysts are assumed to have formed by crystallization in the parent magma, and microanalytical data support this assumption. Some calcic plagioclase xenocrysts were probably added to the magma by wallrock contamination prior to eruption. Feldspar phenocrysts larger than 100 μm are easily distinguished from coarse, authigenic, vapor-phase crystallized feldspar by their larger size, and the presence of euhedral crystal outlines, local overgrowth rims and/or broken edges. Smaller phenocrysts may be difficult to distinguish from coarsely crystallized material, but are usually distinguished by one or more of these textures. Oxide and ferromagnesian phenocrysts are typically small (less than 100 μm), but are present in both finely and coarsely crystallized material, arguing against an *in situ* origin.

X-Ray Powder Diffraction

X-ray powder diffraction (XRD) was used for qualitative mineral identification of finely crystalline authigenic phases in the devitrified matrix, vapor-phase-altered material and carbonate-rich lithophysal cavity fill. Samples were scraped from cut core, and obvious phenocryst phases were removed during examination with a binocular microscope. Samples were crushed to a fine powder and made into an aqueous suspension which was spread evenly on a microscope slide and allowed to dry. X-ray diffraction patterns were obtained with nickel-filtered $\text{CuK}\alpha$ radiation, and x-ray peaks (in degrees 2θ) were recorded by using an automated goniometer and strip chart recorder. Mineral identification was made by comparison with mineral standard patterns contained in the JCPDS powder diffraction file.

The low abundance of phenocrysts in the samples, in addition to the separation procedures used, resulted in XRD patterns due primarily to fine-grained phases formed by *in situ* crystallization of the tuff. Estimated abundances are qualitative but are based

in part on empirical relations between XRD peak intensities and concentration (K factors) for minerals in NTS tuff samples derived by Pawloski (1983) for quantitative XRD. XRD data are presented in outline form in Appendix A, Table A-1.

Phases identified in the devitrified matrix include cristobalite, one or two feldspars, and quartz. Peak intensities suggest that cristobalite is the dominant phase, feldspars are subordinate, and quartz is relatively minor. Peak overlap prohibits identification of specific feldspars, but the dominant peaks suggest that both Na-rich and K-rich varieties are present.

Phases identified in the vapor-phase-altered material include tridymite, possibly with some cristobalite, anorthoclase feldspar, a subordinate K-rich feldspar and minor quartz. Minor calcite is present locally, and optical microscopy suggests that it formed by surficial deposition. The low intensity of the 200 (4.27 Å) peak of tridymite and the tendency for the 0020 (4.08 Å) peak to be intermediate between tridymite and cristobalite suggests that the dominant silica phase is a disordered tridymite-cristobalite, rather than well-ordered tridymite. Based on relative peak intensities, tridymite-cristobalite appears to be dominant, and quartz and feldspars are somewhat less abundant. In two of four samples, quartz is minor or absent, whereas in the other two samples quartz is prominent, though less abundant than tridymite.

Clay minerals (detection limit is about 5 percent) were not found either in vapor-phase-altered material or in the devitrified matrix, whereas 5-10 percent montmorillonite-smectite clays were reported from lithophysal horizons in the USW G-1 drillhole (Bish et al., 1981; Carroll, Caporuscio, and Bish, 1981), NTS (Figure 1). Their estimates of the abundance of other minerals are similar to ours, suggesting that the difference in clay contents is not an artifact of the analysis. Petrographic examination of several USW G-1 samples in which clays are clearly present, supports this conclusion.

The major difference between the vapor-phase-altered material and the devitrified matrix is the dominance of tridymite and quartz in the former, and the dominance of cristobalite and quartz in the latter. Although authigenic alkali feldspar is present in matrix and altered material, differences in x-ray peak locations indicate that feldspar compositions and/or structural states are different in the two matrix types.

Carbonate-rich material locally lining and filling cavities in lithophysae is dominated by calcite, with a significant but subordinate amount of cristobalite-opal (Opal-CT of Jones and Segnit, 1971). A weak 12 Å peak along with subordinate minor peaks in one of the two samples analyzed appears to be due to a poorly crystalline mixed-layer clay. This material appears to have been deposited by surficial processes, chiefly short-term precipitation, leaching by acidic rain water, and subsequent evaporation within

the upper few meters of the ground surface. This type of process is responsible for the silica-carbonate "caliche" typical of desert soil horizons in which evaporation exceeds infiltration.

Microanalysis

Electron microprobe analyses were made with an automated five spectrometer JEOL 733 Superprobe by means of wavelength-dispersive analysis. The instrument was operated at 15-kV acceleration potential and varying beam currents. Feldspar and matrix analyses were made with currents of 0.01 μA and mafic silicates and oxides were analyzed with 0.02 μA current. A broad (10 μm to 15 μm diameter) electron beam was used for most analyses to minimize sample heating and volatilization of alkalis and water during analysis. Oxide weight percentages reported in the data tables in Appendix A were corrected using the method of Bence and Albee (1967), as incorporated in the SANDIA TASK-83 electron microprobe automation package (Chambers, 1983). Variability estimates are one standard deviation (n-1 weighting) for the number of analyses averaged. For averaged matrix and vapor-phase-altered material analyses, standard deviations are indicative of variations in crystal size. The larger deviations imply average crystal sizes larger than the 10 μm beam used in the analyses, whereas the smaller deviations imply a predominance of smaller crystals and more homogeneous compositions relative to the 10 μm beam diameter.

Optical microscopy suggests that the vapor-phase-altered material originated as shard matrix. Comparison of the compositions of feldspar phenocryst populations between the two materials supports this conclusion. In addition, comparison of feldspar with bulk matrix compositions is useful in understanding the crystal-liquid fractionation trends for the magma of the Topopah Spring Member, and facilitates comparison with other tuff units (e.g., the Grouse Canyon Member of the Belted Range Tuff), in which thermomechanical experiments in support of NNWSI are being conducted.

Feldspar Phenocrysts : Two feldspar phenocryst phases are present in all samples. Alkali feldspar (Table A-2; average composition $\text{An}_3\text{Ab}_{47}\text{Or}_{50}$) is the most abundant, and plagioclase (Table A-3; average composition $\text{An}_{18}\text{Ab}_{73}\text{Or}_9$) is slightly less abundant. Oscillatory zoning is common in plagioclase and is reflected in the analyses by relatively minor variations in the Ab-Or proportions (± 2 to 3). Systematic zoning is not notable, but there is a slight tendency for Na_2O (Ab) to be enriched in phenocryst rims (particularly alkali feldspars) relative to K_2O (Or). Rare phenocrysts show optically distinctive cores of Ca-rich ($\text{An} > 35$) and K-poor ($\text{Or} < 4$) plagioclase (Table A-3, Analyses 2, 7, 10 and 13), overgrown by plagioclase or alkali feldspar similar in composition to the typical phenocryst

Analysis 11). This plagioclase is less calcic and more sodic than that in the Busted Butte samples. Comparison of measured section data obtained by us with core logs of USW G-1 (Spengler, Byers, and Warner, 1981) and other measured section data (Lipman, Christiansen, and O'Connor, 1966), suggest that the USW G-1 sample analyzed is from a higher stratigraphic level than the Busted Butte samples. The data are consistent with the upward increase in Ab/Or ratios in alkali feldspar phenocrysts and the upward decrease in An/Ab ratios in plagioclase noted by Lipman, Christiansen, and O'Connor (1966).

When applied to the average plagioclase and alkali feldspar phenocryst compositions, the two-feldspar geothermometer of Stormer (1975) yields an equilibration temperature (at $P=1$ kb) of approximately 790°C . The graphic two-feldspar geothermometer of Brown and Parsons (1981) yields an equilibration temperature of about 750°C (at $P=1$ kb). Uncertainties regarding mixing behavior of ternary alkali feldspars with high Ca contents and ternary plagioclases with high K contents make these temperatures only approximate, but substantial agreement with Fe-Ti oxide equilibration temperatures discussed below suggests magmatic temperatures close to 800°C .

Mafic Silicate Phenocrysts : Mafic silicate phenocrysts are rare in all samples, with modal abundances much less than 0.5 %. Biotite (Table A-4, Analyses 1, 2, and 3) is most abundant. It is typically dark brown to almost opaque, and close examination in reflected light and by energy dispersive analysis (EDS) indicates the presence of lamellae of Ti-magnetite parallel to cleavage planes (001) of the biotite laths. Compositions determined by electron microprobe are typical for igneous biotites and are similar to those from a quartz latite from the San Juan Region of Colorado cited by Deer, Howie, and Zussman (1962). Alteration, producing exsolution of an oxide phase and resulting in semiopaque optics, is typical of biotites in extrusive igneous rocks (Deer, Howie, and Zussman, 1962) and is probably related to instability at the low pressure-temperature/high oxygen fugacity conditions just before (and after?) eruption of the tuff.

Rare clinopyroxene phenocrysts are present in several sections. The one grain analyzed (Table A-4, Analysis 4) is an augite which is atypical only in its low Al_2O_3 content.

A very minor but ubiquitous dark brown, prismatic mineral is present in almost all sections. Crystal dimensions average no more than $50\ \mu\text{m}$, making optical identification difficult. Based on previous work (Bish et al., 1981, Carroll et al., 1981) it was initially assumed that this phase was the light REE enriched Ca-Al silicate allanite. However, electron microprobe analyses (Table A-5) indicate that the mineral is chevkinite, a light REE enriched Fe-Ti-Ca silicate. Chevkinite has previously been reported from NTS tuffs (Young and Powers, 1960) and from several airfall tuff deposits in the western United States (Izett and Wilcox, 1968). Chevkinite is also present in a sample from the quartz

(Table A-4, Analysis 4) is an augite which is atypical only in its low Al_2O_3 content.

A very minor but ubiquitous dark brown, prismatic mineral is present in almost all sections. Crystal dimensions average no more than $50\ \mu\text{m}$, making optical identification difficult. Based on previous work (Bish et al., 1981, Carrol et al., 1981) it was initially assumed that this phase was the light REE enriched Ca-Al silicate allanite. However, electron microprobe analyses (Table A-5) indicate that the mineral is chevkinite, a light REE enriched Fe-Ti-Ca silicate. Chevkinite has previously been reported from NTS tuffs (Young and Powers, 1960) and from several airfall tuff deposits in the western United States (Izett and Wilcox, 1968). Chevkinite is also present in a sample from the quartz latite caprock of the Topopah Spring Member in USW G-1 and may be widespread in other tuff units at Yucca Mountain as well.

Fe-Ti Oxides : The iron-titanium oxides magnetite and ilmenite are ubiquitous minor phases in all sections of lithophysal tuff. Exsolution of a Ti-rich ilmenite from magnetite and Ti-poor magnetite from ilmenite is characteristic of slowly cooled Fe-Ti oxides, and most oxides in the samples examined show some exsolution. Analyses of oxides from one sample with exsolved and homogeneous phases are presented in Table A-6.

Fe-Ti oxide equilibration temperatures and oxygen fugacities for unexsolved magnetite-ilmenite pairs were calculated by a computer program from the microprobe data using several mixing models (Stormer, 1983). Data calculated using all possible combinations of oxide pairs with recalculated analytical totals (after partitioning iron into FeO and Fe_2O_3) of between 98 and 102% (Table A-6, Analyses 1, 2, 4, with 6, 7, 8) yielded temperatures between 730 and 846°C (average 782 to 791°C , depending on the mixing model) and oxygen fugacities of $10^{-14.7}$ and $10^{-11.8}$ atm (average $10^{-13.5}$ to $10^{-13.1}$ atm depending on the mixing model). The close agreement with temperatures calculated from feldspar phenocryst geothermometry suggests magmatic equilibration of oxides and feldspars near 800°C .

Although analytical data are not as good for exsolved phenocrysts, temperatures and oxygen fugacities calculated for exsolved host and exsolution lamellae range from 676 to 784°C (average 726 to 762°C) and $10^{-13.8}$ to $10^{-11.2}$ atm (average $10^{-12.9}$ to $10^{-12.5}$ atm), respectively. Though subject to uncertainties due to the low angle of intersection of the mixing curves and lower analytical totals, in general these temperatures are substantially lower and oxygen fugacities substantially higher than for unexsolved pairs.

Discrete, very small euhedral lath-shaped opaque oxide grains averaging 8 by $25\ \mu\text{m}$ are a ubiquitous minor constituent of the vapor-phase-altered material. Analyses (Table A-6, Analysis 9) are high in iron, manganese and magnesium relative to the phenocryst

oxide phases, and only yield good analytical totals ($> 98\%$) when all iron is calculated as Fe_2O_3 and all manganese as MnO_2 , implying a very high oxygen fugacity during vapor phase crystallization. The difference in color between the reddish-brown devitrified shard matrix and the gray vapor-phase-altered material may be most reasonably accounted for by abundant disseminated Fe_2O_3 in the former and recrystallization into small discrete Fe_2O_3 -rich grains by vapor phase alteration in the latter. The overall gray color of the vapor-phase-altered material should not be used to infer more reducing conditions during vapor phase crystallization.

Matrix Analyses : Broad beam analyses of devitrified matrix (Table A-7) and vapor-phase-altered material (Table A-8) were made to ascertain if any major element migration occurred as a result of vapor-phase-alteration, on what scale that migration occurred, and if any difference in porosity could be noted based on variations in analytical totals or reaction of the sample to the electron beam.

Several textural types are observed in the devitrified matrix. These include crypto- to micro-crystalline "dusty" material between shards, axiolitic replacement of individual shard forms, and spherulitic replacement of clusters of shards which cross cut shard boundaries. Within the limits of analytical error, there is no difference between the average compositions of these different textural types (Table A-7, Analyses 1 and 2), suggesting that the textural variations are not related to major element composition. The cryptocrystalline and axiolitic shard matrices are probably the result of primary textural differences, the former having crystallized from fine dust and the latter from glass shards. As noted in the section on petrography, spherulites tend to be most extensive in "pressure shadows" around rigid phenocrysts, suggesting that spherulitic crystallization occurred in regions of relatively low stress, subsequent to welding.

Dark reddish-brown fiamme, typically dominated by crystallization of many small spherulites and locally by a greatly increased modal percentage of feldspar phenocrysts, are relatively rare in these samples. Spherulites in the fiamme (Table A-9) are distinctly less silicic, more aluminous, and more iron-rich than the devitrified matrix in the same samples. In terms of bulk composition, these fiamme resemble the less silicic rhyolite and silicic quartz latite caprock found near the top of the Topopah Spring Member. However, $\text{CaO-Na}_2\text{O-K}_2\text{O}$ ratios are similar to the host rock matrix. This suggests an origin by an *in situ* differentiation process, rather than mixing of different magma components or exotic contamination.

Quantitative comparison of analyses of devitrified matrix and vapor-phase-altered material is difficult because of limitations in obtaining reliable average compositions and because of generally low analytical totals in the altered material. The larger crystal sizes

in the vapor-phase-altered regions result in variations in amounts of individual oxides generally two to five times larger than variations in the very finely crystalline devitrified matrix. During analysis of randomly selected points in the vapor-phase-altered material, the degradation of the polished surface by destruction of pores is typical and in general, the greater the surface degradation, the lower are the analytical totals. This suggests that the low totals are produced primarily by the presence of extensive porosity on a scale smaller than the $10\mu\text{m}$ electron beam, and observation of this degradation during analysis suggests a general size range of 1 to $3\mu\text{m}$.

When analyses are normalized to 100 percent to minimize porosity effects, comparison of analyses of devitrified matrix and vapor-phase-altered material suggests that SiO_2 and Al_2O_3 contents are generally the same within limits of analytical errors. In individual analyses of both materials, there is generally an inverse relationship between SiO_2 and Al_2O_3 , K_2O , Na_2O , and CaO . This is particularly pronounced in the more coarsely crystalline vapor-phase-altered material and is probably due to analytical points being within silica (cristobalite/tridymite/quartz) or feldspar dominated areas. In general, molecular $\text{CaO-Na}_2\text{O-K}_2\text{O}$ proportions tend to show a slight enrichment in CaO and Na_2O in vapor-phase-altered material in comparison to slight K_2O enrichment in the devitrified matrix. Iron content (as FeO) tends to be higher by a factor of two to five in devitrified matrix relative to the vapor-phase-altered material. As noted in a previous section, most of this may be accounted for by the presence of discrete Fe-Ti-Mn oxide crystals produced during vapor phase alteration which are not included in the averages for the altered material. It should be noted that these minor compositional variations are observed in both vapor-phase-altered material and in patches of texturally similar vapor-phase-altered matrix occurring as lensoid zones in the devitrified matrix. However, porosity in the latter is similar to that in devitrified matrix.

Analyses of matrix and alkali feldspar phenocrysts show fractionation of Al_2O_3 , CaO , Na_2O , K_2O , and BaO into the feldspar, leaving a rhyolitic matrix enriched in SiO_2 and FeO . It is notable, however, that the $\text{CaO-Na}_2\text{O-K}_2\text{O}$ proportions and agpaitic indices (molecular $[\text{Na}_2\text{O}+\text{K}_2\text{O}]/\text{Al}_2\text{O}_3$) are very similar in alkali feldspars and matrix, with agpaitic indices and $\text{CaO-Na}_2\text{O}$ proportions generally slightly higher in matrix than phenocrysts. This is in marked contrast to the peralkaline Grouse Canyon Member, in which agpaitic indices are much higher for the matrix, and Na_2O and CaO are greatly enriched in the phenocrysts relative to the matrix (Connolly et. al., 1983; Connolly and Keil, in prep.). Thus, although the present bulk compositions of the Topopah Spring Member and the Grouse Canyon Member are not greatly different, it is evident that the processes of magmatic fractionation were considerably more extreme in the Grouse Canyon Member.

Comparison With USW G-1 Lithophysal Tuff Samples : Lithophysal tuff samples from the Topopah Spring Member in drillhole USW G-1 were obtained from drill depths of 124 m (407 ft), 137 m (449 ft) and 154 m (505 ft). Polished thin sections of the USW G-1 samples were examined with the optical microscope, and limited feldspar phenocryst and matrix analyses were obtained with the electron microprobe to facilitate comparison with data obtained from the Busted Butte samples. Devitrified matrix and vapor-phase-altered material are texturally identical in the two sample suites, and pore size and pore distribution also appear to be identical, based on optical examination and behavior of the samples under the electron beam during microanalysis. One of the USW G-1 samples (124 m) is crystal rich (10% phenocrysts), but the two deeper samples have phenocryst modal percentages similar to those of the Busted Butte samples. The most notable difference is the presence of a few percent clay minerals disseminated in the matrix and vapor-phase-altered material in one drillhole sample (137 m). The patchy distribution of this material suggests origin by alteration rather than by primary devitrification or vapor-phase alteration. The clay mineral development is not evident in the deeper USW G-1 sample (154 m), nor is it noted in any of the Busted Butte samples. Another minor but notable difference is that tridymite filling in pores appears slightly more abundant in the USW G-1 samples than in the Busted Butte samples. As discussed in the microanalysis section, the feldspar phenocryst compositions and matrix "bulk" compositions in the suite of Busted Butte samples are only slightly different than in the USW G-1 samples.

Relevance to Analysis of Mechanical Test Results

The petrologic characterization of the lithophysal tuff samples presented in the preceding sections provides a base of data to assist in comparison of these rocks with similar samples obtained from the subsurface. Outlined below are several aspects of the petrology which are relevant to interpretation of the bulk properties and mechanical test data presented in the following sections of this report.

First, comparison of the samples studied here with lithophysal tuffs from drillhole USW G-1 indicates that the surface samples are essentially the same as those expected to be encountered underground at Yucca Mountain. The similarity is very strong in terms of the fabric of both devitrified matrix and vapor-phase-altered material, the presence of vapor-deposited tridymite in both lithophysae and larger pores in the vapor-phase-altered material, and porosity size characteristics and distribution between the three major components of the tuff (matrix, vapor-phase-altered material, and lithophysae). There are no detectable amounts of clay minerals in these samples, and there is no notable

alteration of the primary components of the tuff except for partial filling of some of the lithophysae by silica-carbonate surface-deposited material (caliche). Local subsurface alteration of devitrified and vapor-phase-altered matrix to clay minerals is evident in some samples of USW G-1 core which is not evident in the Busted Butte samples, and the caliche fill present at Busted Butte is not evident in any samples from USW G-1.

Second, the distribution of porosity in the lithophysal tuff samples is unlike that in most other tuffs from Yucca Mountain with similar bulk density and total porosity. In the lithophysal samples, the vast majority of the porosity is concentrated in lithophysae and surrounding vapor-phase-altered material, whereas in the nonlithophysal tuffs porosity is more evenly distributed throughout the sample matrix (Lappin et. al., 1982; Connolly et. al., 1984). The matrix of the lithophysal samples is devitrified to a mixture of alkali feldspar, cristobalite and quartz in a tight interlocking network of crystals in which the average crystal size is well under 10 μm . The matrix fabric is microscopically identical to that of moderately to densely welded nonlithophysal tuff.

MODAL ANALYSIS

The proportions of the three components (matrix, vapor-phase-altered material, and lithophysae) in the mechanical test samples were estimated by point counting of all ten and by planimetry of three samples. The results of these studies are discussed separately.

Point Counting

Point counts were performed using four axial traverses of each sample. The traverse lines were located at approximately 90° intervals around the cylinder. Components were counted at 6 mm (0.25 in) increments along each line except where sample labeling prevented component identification. The theoretical number of counts per sample, based on the sample size, is 336, whereas the actual number counted was slightly less than that.

Table 2 provides point count data for the lithophysal samples. Listed variances were calculated in the manner described in Appendix B.

Since all ten samples were taken from a single outcrop of lithophysal tuff and each may be assumed to be a random sample of lithophysal material, means and standard deviations of the volume fractions of each component can be calculated assuming independent sampling. The results for the three components are as follows: 0.545 ± 0.045

for the matrix, 0.289 ± 0.041 for the vapor-phase-altered regions, and 0.167 ± 0.035 for the voids.

Planimetry

Planimetric analysis of areal percentages of the three components was performed on photographs of samples 8A, 8B, and 8F. Unfortunately, useful photographs of the pre-deformed samples were available only for the ends of the samples, so a direct comparison between planimetry and point counting on the same area is not possible for these rocks.

The planimetry results are summarized in Table 3. The data are estimated to have a high precision, based upon a statement by Mathieu, Hoppeler, and Weibel (1980) that planimetry and point counting have comparable precisions when a large number of points are counted. Calculation of accuracy is not possible from the planimetry data on the lithophysal samples, but Haug (1981) suggests that planimetry is two to five times more accurate than point counting, which suggests accuracies of $\pm 0.011-0.028$ for the matrix, $\pm 0.009-0.027$ for the altered regions, and $\pm 0.007-0.023$ for the voids.

For two samples (8A and 8F), data were obtained on the elongation of the lithophysae (L) and surrounding altered region (A). For both samples, the average ratio of long axes to short axes of measured areas was 2.28 to 2.29 for the lithophysae, and 1.80 to 1.85 for the altered regions. The end samples were generally cut at a low angle to layering, and thus elongation is lower than what would be expected perpendicular to layering. However, the data indicate that both the lithophysae and altered regions are elongate and that the elongation of lithophysae is notably longer.

Comparison of data in Tables 2 and 3 for samples 8A, 8B, and 8F indicates that six of the nine planimetry values fall within the 95 percent confidence intervals of the corresponding values derived from point counting. The three exceptions are the matrix and altered region percentages for 8B and the void percentage for 8A.

Several explanations of the discrepancies are possible. One is the difference in the areas sampled by the two techniques, as mentioned earlier. Another possibility is that the planimetry results in some cases may be slightly affected by a lack of visual contrast between the components in the photographs. If small voids and small altered regions are obscure in a photograph, the matrix percentage would be higher in the planimetry measurements than found by point counting, as seen in Tables 2 and 3. The same explanation might serve for the low void value found by planimetry for 8A.

Based on the small number of data available, planimetry and point counting are judged to provide similar data on the modal percentages of the components of the lithophysal samples. If comparable work is to be performed on other samples in the future, planimetry is probably a better method to use because of the ability to analyze component shapes as well as areas. Efforts should be made, however, to analyze the sides of the samples in addition to, or instead of, the ends.

BULK PROPERTIES

A more complete understanding of mechanical test results on samples of lithophysal Topopah Spring Member depends, in part, on consideration of possible effects of grain density and porosity (Price, 1983). In order to fully characterize the bulk properties of the test samples, the grain density and porosity of the matrix and the vapor-phase-altered material must be known, as well as the porosity contributed by the lithophysae.

Before mechanical testing, all of the test samples were water saturated (the saturation procedure is described in Appendix C). The saturated weights were combined with measured volumes to provide saturated bulk densities of the samples. Bulk sample grain density, matrix grain density, and matrix porosity were measured on pieces of scrap taken from the end of each sample during the machining process. The remainder of the bulk properties were calculated from these measured properties and the modal percentages obtained from point counting. The calculated properties include total porosity and the porosity and grain density of the vapor-phase-altered material. A detailed discussion of the methods used to obtain all of these properties is presented in Appendix C. The results are compiled in Table 4.

Discussion

In order to determine the reasonableness of the results for the calculated parameters listed in Table 4, an independent estimate of the parameters is required. The best independent estimate can be made for the grain density of the altered material. Based on microscopic examination and XRD analysis, the material is predominantly a mixture of tridymite and alkali feldspar, with minor quartz. The density of tridymite is 2.26 g/cm^3 , the density of quartz is 2.65 g/cm^3 , and a representative density for alkali feldspar is 2.57 g/cm^3 . Mineral norms calculated for the broad beam microprobe analyses of altered material in five samples (1B, 1D, 8C, 8E, and 8F) are at least 96% feldspar and silica.

Norms vary somewhat, but all fall in the range of 50 to 90 percent feldspar (averaging 60-70%), and 10 to 50 percent SiO₂ phase (averaging 30-40%). Based on XRD peak intensity ratios, it is estimated that 20 percent of the SiO₂ phase is quartz and the remainder tridymite. Calculated grain densities using these assumptions vary between 2.45 g/cm³ (50% SiO₂ phase) and 2.55 g/cm³ (10% SiO₂ phase), and for an average 65 percent feldspar, 35% SiO₂ composition, the grain density is 2.49 g/cm³. Based on this estimate, the calculated parameters for 8A, 8C, and 8F appear to be high, and those for 1B, 1D, and 8B appear too low, suggesting the possibility of error in either the measured properties or in the assumptions used in the calculations.

In order to examine the effects of experimental error on the calculated parameters, the values of the overall grain densities of the six samples for which the grain densities of the altered material seemed incorrect were changed by 0.02 g/cm³ (the experimental error in the grain density), the direction of the change being determined by whether a sample's grain density was too high or too low.

The new values of the ten parameters are given in Table 5. The calculated grain densities are within the expected range except for samples 1B and 1D, which have slightly low grain densities. Given the assumptions involved in using the chosen values of input parameters as well as the simplifications in calculating the expected range of grain densities, the variances between the calculated and theoretical grain densities are not thought to be significant.

Comparison of values calculated for the total porosity and the porosity of the matrix shows little change between Tables 4 and 5. Calculations involving changes in other input parameters within their ranges of experimental error also result in little change in calculated porosities. Thus, the values of the calculated porosities are probably close to actual values.

Relevance to Analysis of Mechanical Test Results

Of the data discussed in the previous section, the total porosities of the test samples are the most useful in analysis of mechanical test results, based on the findings of Price (1983). The values for the total porosity of the ten samples are provided in Table 5, and used in the analysis of the mechanical properties (see next section). Porosities of the individual components also may be useful to future analysis of mechanical test results by allowing a more detailed analysis of test results based on the mechanical behavior of the different components.

MECHANICAL PROPERTIES

This section presents the results from deformation experiments on 10 water saturated samples. The tests were performed in compression at atmospheric confining pressure, room temperature (23°C), and a nominal strain rate of 10^{-5} s^{-1} . Previous mechanical tests conducted on intact samples of the Topopah Spring Member of the Paintbrush Tuff have been reported by Olsson and Jones, 1980; Price, Nimick and Zirzow, 1982; and Price, Spence and Jones, 1984.

Experimental Techniques

The mechanical experiments were performed on a load frame (Figure 14) with a maximum load capacity of 5.0 MN ($1.1 \times 10^6 \text{ lb}$). A constant displacement rate of the loading piston was achieved by servo-control of the hydraulic loading ram while monitoring a linear variable displacement transformer (LVDT) connected between the frame and the lower sample assembly end cap.

Throughout this test series, axial stresses (σ_{ax}) were calculated by dividing the forces, measured on a standard load cell, by the original cross-sectional area of the sample (i.e., engineering stress). Axial strains (ϵ_{ax}) were calculated by dividing the measured displacements on the LVDT mounted to the lower endcap (minus machine and loading column displacements) by the original sample length (i.e., engineering strain). Lateral (transverse) displacements were measured across two sample diameters (located at forty percent of the sample length from each end) by a ring gage (as described by Holcomb and McNamee, 1984). Lateral strains (ϵ_{lat}) were then obtained by dividing the lateral displacements by the original diameter of the test specimen. Axial force, axial displacement, transverse displacement and time data were collected, reduced and plotted by a mini-computer, and then stored on floppy disks.

The test system load cell is calibrated once a year against a standard transducer, which is traceable to the National Bureau of Standards (NBS). The most recent load cell evaluation prior to this test series was performed on May 2, 1983 (i.e., approximately 6 months prior to the mechanical tests). The axial displacement LVDT and the two transverse displacement LVDT's were calibrated with a standard micrometer head (also

traceable to the NBS) just prior to the test series. Calibration data for the load cell, axial LVDT and ring LVDT's are listed in Table D-1 (Appendix D, Table 1).

Calibrations of the experimental methods and the entire instrumentation setup were obtained prior to and following the experiments by testing a 6061-T651 aluminum cylinder (266.7 by 533.4 mm) of known mechanical properties (Young's modulus, E , of 69.7 GPa and a Poisson's ratio, ν , of .33). The aluminum calibration test data are listed in Table D-2 and plotted in Figure D-1. The limited amount of lateral strain data in the pretest series calibration (Table D-2) is due to a failure in the computer data-collection system, resulting in the acquisition of lateral and axial strain data on different backup time-based plotters.

The test samples were water saturated by the method described in Appendix C. Each saturated sample weighed approximately 580 N; consequently, they were carefully lifted out of the saturation tank and carried over to the test apparatus with an overhead crane. Each sample was then positioned between steel end pieces (caps), the sample assembly placed between the loading ram and the load cell, the axial LVDT and ring gages mounted, and the mechanical experiment begun.

Experimental Results

Summaries of the mechanical property results are given in Table 6. The ranges of Young's moduli, Poisson's ratios, unconfined strengths and axial strains at failure are 10.9 to 21.5 GPa, 0.13 to 0.21, 10.3 to 27.8 MPa and .0010 to .0015, respectively.

The differential stress-axial strain curves are presented in Figure D-2. The general shapes of the stress-strain curves are very similar to previously reported unconfined test results on samples of welded, nonlithophysal Topopah Spring Tuff (Price, Nimick and Zirzow, 1982; Price, Spence and Jones, 1984) and on samples of other Yucca Mountain silicic tuffs (Price, Jones and Nimick, 1982; Price and Nimick, 1982; Price and Jones, 1982). In general, the curves exhibit an initial concave-upward portion, a linear region, a concave-downward portion and a downward break. These curve characteristics are interpreted to reflect crack closure and/or pore collapse, elastic deformation, material yield and macroscopic failure of the test specimen, respectively. Stress-strain results from all of the lithophysal samples (this report) and higher porosity nonlithophysal samples (earlier reports listed above) tend to reflect macroscopic sample failure by a gradual decrease in the slope of the stress-strain curve beginning at approximately 75-90 percent of ultimate stress, and then strain soften sharply following the ultimate stress. This is in

contrast to the curves from lower porosity tuff samples that usually remain relatively linear up to ultimate stress, and then have an immediate total loss of load-bearing capability. Also, the data on lithophysal samples reported here do not have the initial concave-upward curvature as those previously reported for nonlithophysal samples of equivalent porosity. This is probably due to the difference in the distribution of the porosity in the two sample types, the strong (low porosity) matrix material not allowing the large lithophysae to collapse, while the weaker (high porosity) matrix allowing pumice fragments to collapse in the high-porosity, nonlithophysal samples. Another difference in the curve characteristics is exhibited in three lithophysal sample results (1B, 1D and 8D). These offsets in the stress-strain curves show short-term, recoverable losses of strength during loading, corresponding to the formation of mesoscopic fractures within the sample (releasing strain energy), which then lock-up and allow the bulk sample to load again (building up strain energy) until the sample macroscopically fails at the approximately the ultimate stress.

In the initial stages of each experiment, very little was visually or audibly observed, because the samples were only elastically deforming. However, later in the test (i.e., beginning at approximately 75 to 80 percent of the ultimate sample strength), cracks formed that were observed readily because water drained freely from them. In addition, audible acoustic emissions from the formation of fractures were heard without amplification. They were isolated at first (up to about 75 percent of ultimate strength), increasing in frequency and amplitude up to macroscopic rock failure. This sample behavior was also observed in the lateral strain-axial strain curves, which are presented in Figure D-3. At low strains, the curves are characteristically linear with an increase in the negative slope of the curves at approximately one-half to two-thirds of the axial strain at ultimate stress. Increases in the lateral strain values, relative to the axial strains, are indicative of bulk sample dilation due to the formation of fractures. The relationship between sample dilation, fracture formation and acoustic emissions has been carefully studied by others, including Scholz (1968).

Discussion

An empirical relationship between ultimate stress and porosity for samples from several Yucca Mountain silicic, nonlithophysal tuff units was first reported by Olsson and Jones (1980), and then expanded to include montmorillonite volume in an 'effective' porosity by Price (1983). Figure 15 presents the ultimate stress versus effective porosity results from this study plotted with the data for nonlithophysal Yucca Mountain tuff. In

general, the lithophysal tuff data fall below the nonlithophysal data band. This difference is believed to result from relatively large lithophysal voids common in these samples (most ranging from less than 10 up to 50 mm, with a few as large as 100 mm across), when compared to the sample size (diameter of 267 mm). In retrospect, the sample size chosen was slightly less than optimum for studying intact mechanical properties of this particular rock type. As indicated above, the lithophysal cavity size was in many cases more than the one-tenth of the sample diameter which is the maximum inhomogeneity size to sample size ratio suggested when examining intact rock properties (e.g., see Vutukuri, Lama and Saluja, 1974, p.44). Furthermore, several studies have shown compressive strengths to be dependent on sample size. Hoskins and Horino (1969) have shown for several materials (limestone, marble, sandstone, granite, and plaster of paris) and Alekeev et. al. (1970) for argillite that ultimate stresses in compression tend to be directly related to sample size up to a point, with the trend then reversing, eventually leveling off to a constant with additional increases in sample size. Evidence supporting the conclusion that these samples were somewhat undersized becomes apparent when the ratios of relative proportions of lithophysal porosity ($L \times \phi_L$) to total porosity (ϕ_T) are determined for each sample (Table 7). Of the four samples (3A, 8A, 8D, and 8F) that best fit the nonlithophysal data, three have the lowest lithophysal proportions (3A : 0.350, 8A : 0.361, 8F : 0.346), whereas the worst fitting sample (1D) has the highest lithophysal proportion (0.649). As a result, the lithophysal cavities are either few and small enough to keep from dominating the eventual failure stress of the sample, or else common and large enough to create an unstable situation early in the deformation (when smaller, micro- and mesoscopic fractures are beginning to form). The instabilities were the result of large stress concentrations due to redistribution of stresses around lithophysal cavities.

Price (1983) also observed that Young's modulus is a function of effective porosity. In general, the degradation of the Young's modulus with increasing porosity can be explained analytically; however, the constituent (matrix) material is assumed to be the same in all cases. When data from lithophysal and nonlithophysal samples are plotted together, the data points for lithophysal samples generally fall above the band of nonlithophysal test data (Figure 16). This disparity may be due to a difference in the mechanical behavior of the lithophysal and nonlithophysal matrix materials. The high porosity, nonlithophysal tuffs have matrices which are nonwelded (i.e., the grain to grain contacts are loosely interlocked), and thus provide relatively little resistance to deformation. In contrast, the matrix of the lithophysal samples is a low porosity material in which the grains are densely welded (i.e., firmly annealed). This suggests that the higher Young's moduli of the lithophysal samples may be due to a much more tightly interlocked (stiffer) matrix than is present in the high porosity, nonlithophysal tuffs.

One possible explanation of both the lower strength and higher Young's modulus data is a consequence of higher pore pressure build-up in the large lithophysal cavities, than in the micrometer size cavities of the nonlithophysal samples. Consider the following form of Darcy's law :

$$k = \frac{q \mu l}{A (\Delta p)},$$

where k is permeability, q is volumetric flow rate, μ is fluid viscosity, l is flow length, A is the area perpendicular to the flow direction, and Δp is differential pressure. If the permeability, viscosity, and flow length are held constant, a decrease in the cross-sectional area of the flow implies a decrease in the ratio of the flow rate to differential pressure of the same proportion. The permeabilities of high porosity, nonlithophysal tuffs are one to two orders of magnitude higher than the low porosity, welded tuffs (Duffy, 1984). For the purpose of this analysis, the simplifying assumption will be made that the two tuff types have the same permeability (since the difference in permeabilities would only enhance the effect described here). The fluid in both systems was water, and therefore the viscosities were the same. The flow length of the water in the lithophysal tuff samples was greater in order for the system to reach an equilibrium state (since the distances between lithophysal 'pores' was much larger than between the small pores of the nonwelded tuffs); however, this (again) would only enhance the effect described here. Because there are about three orders of magnitude difference in the pore sizes of the lithophysal samples (at least several millimeters) and the nonlithophysal samples (several micrometers), the surface areas of the respective pores (holding porosity constant) differs by approximately six orders of magnitude. This surface area difference implies a contrast between the lithophysal and nonlithophysal samples of the same order of magnitude in the flow rate, the reciprocal of the differential pressure, or a combination of the two. If the flow rate of the water out of the lithophysal pores was substantially less than out of the micrometer size pores, then, obviously, higher pressures would result in the lithophysal cavities. This implies an increase in the differential pressure, and therefore, the variables are inter-dependent. As a result, the relatively incompressible water would tend to stiffen up the lithophysal samples during elastic deformation (i.e., raise the Young's modulus), and the build-up in pore pressures would lower the local effective confining pressure, enhance fracture formation, and hence lower the strength of the bulk sample.

Poisson's ratio values from the nonlithophysal Yucca Mountain tuff experiments are independent of effective porosity (Figure 17). In general, data from the lithophysal samples are below average, regardless of the range of effective porosities considered. According to

Jaeger and Cook (1976), this relationship would be expected if pores (i.e., lithophysal cavities in this case) were added to the low porosity, nonlithophysal material : "The effective Poisson's ratio of a body containing equidimensional cavities is less than the intrinsic Poisson's ratio of a solid body." (p.33). Conversely though, if the previous suggestion of transient pore pressures creating higher Young's moduli is assumed to be true, then the lithophysal Poisson's ratios should also be relatively high. It must be pointed out that there is less confidence (i.e., more scatter) inherent in the measurements of lateral strains, because the data are obtained only at two diameters, whereas axial strain is a measurement of the average deformation over the entire sample length. However, in support of the lateral strain data, the two diameter results tend to be very similar (Figure D-3), with the largest discrepancy seen on sample 1B (ν 's of 0.11 and 0.18).

CONCLUSIONS

1. **The Topopah Spring lithophysal material from Busted Butte has very similar petrologic characteristics to stratigraphically equivalent samples from the subsurface of Yucca Mountain.**

- a. **Texturally, these surface samples were found to be identical to lithophysal samples found in USW G-1 core material.**

In general, lithophysae formed by separation of a vapor-rich phase from the solid components of the tuff during welding and devitrification. Segregation of the vapor into "pockets" resulted in the formation of lithophysal cavities a few millimeters to several centimeters across, recrystallization of devitrified matrix around the cavities, and deposition of tridymite in cavities and in pores in the altered material. Welding, devitrification, and vapor-phase activity were broadly sequential but show considerable overlap. Rock texture and composition support the conclusion that very little mobilization of original constituents occurred during devitrification. In contrast, vapor-phase recrystallization resulted in a redistribution of constituents into coarser silica, feldspar, and metal oxide phases.

Porosity in the samples can be grouped into four size categories, with most open space being concentrated in areas where vapor was most active, in and around the lithophysae. Total porosity averages 35 percent, of which about 5 percent is in the matrix, 14 percent in the vapor-phase-altered material, and 16 percent in the lithophysal cavities. This pore size distribution is very different from that in other tuffs of similar bulk porosity, in which porosity is much more uniformly distributed throughout the rock.

- b. **Mineralogically, the two sample suites are very similar, with the major difference being the existence of minor amounts of secondary clay minerals in the drillhole samples that were not observed in the surface samples described here.**

In the Busted Butte samples, authigenic phases in the devitrified matrix and the vapor-phase-altered material are chiefly silica polymorphs and alkali feldspars. The major difference is the dominance of cristobalite in the

devitrified matrix and of tridymite in the vapor-phase-altered zones. No clay minerals are present in either.

The tuff is phenocryst-poor (less than five volume percent). Alkali feldspar and plagioclase are the dominant phenocrysts, with minor Fe-Ti oxides, biotite and quartz, and traces of clinopyroxene, amphibole, and chevkinite. Equilibration of phenocrysts in the tuff at $800 \pm 50^\circ\text{C}$ is suggested by feldspar and Fe-Ti oxide geothermometry. Oxygen fugacity appears to have increased progressively by magmatic crystallization, emplacement, welding, devitrification, and vapor-phase-alteration.

2. **The summary mechanical test results for the ten lithophysal samples are :**

Young's modulus : 15.5 ± 3.2 GPa

Poisson's ratio : 0.16 ± 0.03

Unconfined compressive strength : 16.2 ± 5.0 MPa

Axial strain at failure : 0.00123 ± 0.00018

3. **Young's moduli data from the lithophysal samples are, on average, higher and ultimate strength values lower than data for nonlithophysal samples of equivalent effective porosity.**

The high Young's moduli may be due to the lithophysal tuff matrix being a stiffer system than the high porosity, nonlithophysal tuff matrix.

The low strength values of the lithophysal samples are probably a result of the large inhomogeneities (i.e., lithophysae) relative to sample size.

The high Young's moduli and low strengths could also be due to a short-term build-up of pore pressures within the millimeter size lithophysal cavities which were much larger than the pore pressures produced within the micrometer size pores of the nonlithophysal samples.

Poisson's ratio data from the lithophysal samples are, on average, slightly lower than those for nonlithophysal samples.

REFERENCES

- Alekseev, A. D., Zhuravlev, V. I., Yarovaya, L. I., and Molchanenko, V. S.**
Effect of the Geometry and Fracturing of Rock Specimens on Their Strength, *Sov. Min. Sci.*, No. 3, May-June 1970, 281-285.
- Bence, A. E., and Albee, A. L.**
Empirical Correction Factors for the Electron Probe Microanalysis of Silicates and Oxides, *Jour. Geol.*, 76, 1968, 382-403.
- Bish, D. L., Caporuscio, F. A., Copp, J. F., Crowe, B. M., Purson, J. D., Smyth, J. R., and Warren, R. G.**
Preliminary Stratigraphic and Petrologic Characterization of Core Samples from USW-G1, Yucca Mountain, Nevada, Los Alamos National Laboratory Report, LA-8840-MS, 1981.
- Brown, W. L., and Parsons, I.**
Towards a More Practical Two-Feldspar Geothermometer, *Contrib. Mineral. Petrol.*, 76, 1981, 369-377.
- Carroll, P. I., Caporuscio, F. A., and Bish, D. L.**
Further Description of the Petrology of the Topopah Spring Member of the Paintbrush Tuff in Drillholes UE25A#1 and USW G-1 and of the Lithic-Rich Tuff in USW-G1, Yucca Mountain, Nevada, Los Alamos National Laboratories Report, LA-9000-MS, 1981.
- Chambers, W. F.**
SANDIA TASK-83: An Electron Microprobe Automation System, Sandia National Laboratories Report, SAND82-1081, 1983.
- Connolly, J. R., Mansker, W. L., Hicks, R., Allen, C. C., Husler, J., Kell, K., and Lappin, A. R.**
Petrology and Geochemistry of the Grouse Canyon Member of the Belted Range Tuff, Rock Mechanics Drift, U12g Tunnel, Nevada Test Site, Sandia National Laboratories, SAND81-1970, 1983
- Connolly, J. R., and Kell, K.**
Field Relations, Petrology, and Geochemistry of the Grouse Canyon Member of the Belted Range Tuff in the GTUF Rock Mechanics Test Area, U12g Tunnel, Nevada Test Site, Sandia National Laboratories, SAND84-7206, (in preparation)
- Connolly, J. R., Kell, K., Mansker, W. L., Allen, C. C., Husler, J., Lowy, R., Fortney, D. R., and Lappin, A. R.**
Petrology and Geochemistry of Samples from Bed-Contact Zones in Tunnel Bed 5, U12g Tunnel, Nevada Test Site, Sandia National Laboratories, SAND84-1060, 1984

- Deer, W. A., Howle, R. A., and Zussman, J.**
 Rock Forming Minerals, v. 3, Sheet Silicates, Longmans, Green and Co., London, 1962, 55-84.
- Duffy, C. J.**
 Investigations of Possible Matrix Permeability Changes, in : Effects of Long-Term Exposure of Tuffs to High-Level Nuclear Waste-Repository Conditions : Final Report, J. D. Blacic (ed.), 1980, 31-39
- Galehouse, J. S.**
 Point Counting, in Carver, R. E. (ed.), Procedures in Sedimentary Petrology, Chapter 16: Wiley-Interscience, New York, 1971, 385-408.
- Haug, H.**
 On the Proper Use of Point Counting and Semiautomatic Procedures in Stereology, Microscopica Acta, 85 : (2), 1981, 141-152.
- Holcomb, D. J., and McNamee, M. J.**
 Displacement Gage for the Rock Mechanics Laboratory, Sandia National Laboratories Report, SAND84-0651, 1984.
- Hoskins, J. R., and Horino, F. G.**
 Influence of Spherical Head Size and Specimen Diameters on the Uniaxial Compressive Strength of Rocks, U. S. B. M. R. I. 7234, 1969, 16p.
- Izett, G. A., and Wilcox, R. E.**
 Ferrierite, Chevkinite and Allanite in Upper Cenozoic Ash Beds in the Western United States, Amer. Mineral., 53 , 1968, 1558-1567.
- Jaeger, J. C., and Cook, N. G. W.**
 Fundamentals of Rock Mechanics, Chapman and Hall, London, 1976, 585 p.
- Jones, J. B., and Segnit, E. R.**
 The Nature of Opal I. Nomenclature and Constituent Phases, Jour. Geol. Soc. Australia, 18, 1971, 57-68.
- Kelley, J. C.**
 Mathematical Analysis of Point Count Data, in Carver, R. E. (ed.), Procedures in Sedimentary Petrology, Chapter 17: Wiley-Interscience, New York, 1971, 409-425.
- Lapplin, A. R., Van Buskirk, R. G., Enniss, D. O., Butters, S. W., Prater, F. M., Muller, C. B., and Burgosh, J. L.**
 Thermal Conductivity, Bulk Properties, and Thermal Stratigraphy of Silicic Tuffs from the Upper Portion of Hole USW G-1, Yucca Mountain, Nye County, Nevada, Sandia National Laboratories, SAND81-1873, 1982
- Lipman, P. W., Christiansen, R. L., and O'Connor, J. T.**
 A Compositionally Zoned Ash-Flow Sheet in Southern Nevada, U.S. Geol. Survey Prof. Paper 524-F, 1966, 47 p.

Mathieu, O., Hoppeler, H., and Welbel, E. R.

Evaluation of Tracing Device as Compared to Standard Point Counting, *Mikroskopie (Wien)*, **37**, 1980, (Suppl.):413-414.

Nellson, M. J., and Brockman, G. F.

The Error Associated With Point Counting, *Amer. Mineral.*, **62**, 1977, 1238-1244.

Olsson, W. A., and Jones, A. K.

Rock Mechanics Properties of Volcanic Tuffs From the Nevada Test Site, Sandia National Laboratories Report, SAND80-1453, 1980.

Pawloski, G. A.

Quantitative Determination of Minerals in Nevada Test Site Samples by X-Ray Diffraction, Second Symposium on Containment of Underground Nuclear Explosions, Kirtland AFB, Albuquerque, New Mexico, August 2-4, 1983, (UCRL-89414).

Price, R. H.

Analysis of Rock Mechanics Properties of Volcanic Tuff Units From Yucca Mountain, Nevada Test Site, Sandia National Laboratories Report, SAND82-1315, 1983.

Price, R. H., Jones, A. K., and Nimick, K. G.

Uniaxial Compression Test Series on Bullfrog Tuff, Sandia National Laboratories Report, SAND82-0481, 1982.

Price, R. H., and Nimick, K. G.

Uniaxial Compression Test Series on Tram Tuff, Sandia National Laboratories Report, SAND82-1055, 1982.

Price, R. H., and Jones, A. K.

Uniaxial and Triaxial Compression Test Series on Calico Hills Tuff, Sandia National Laboratories Report, SAND82-1314, 1982.

Price, R. H., Nimick, K. G., and Zirzow, J. A.

Uniaxial and Triaxial Compression Test Series on Topopah Spring Tuff, Sandia National Laboratories Report, SAND82-1723, 1982.

Price, R. H., Spence, S. J., and Jones, A. K.

Uniaxial and Triaxial Compression Test Series on Topopah Spring Tuff From USW GU-3, Yucca Mountain, Southern Nevada, Sandia National Laboratories Report, SAND83-1646, 1984.

Scholz, C. H.

Microfracturing and the Inelastic Deformation of Rock in Compression, *Jour. Geoph. Res.*, **73** (4), 1968, 1417-1432.

Schwartz, B. M.

Bulk Properties of Core Samples From Hole USW GU-3, Internal Memo to A. R. Lappin, January 13, 1983.

- Scott, R. B., Spengler, R. W., Diehl, S., Lappin, A. R., and Chovnick, M. P.**
Geologic Character of Tuffs in the Unsaturated Zone at Yucca Mountain, Southern Nevada, in Role of the Unsaturated Zone in Radioactive and Hazardous Waste Disposal, J. Mercer (ed.), Ann Arbor Science, Ann Arbor, MI, 289-335.
- Solomon, M., and Brooks, C.**
Point Counting as a Method of Assaying Wolframite at Story's Creek Mine, Tasmania, Econ. Geol., 61, 1966, 376-384.
- Spengler, R. W., Byers, F. M., Jr., and Warner, J. B.**
Stratigraphy and Structure of Volcanic Rocks in Drillhole USW-G1, Yucca Mountain, Nye County, Nevada, U.S. Geol. Survey Open-File Report, 81-1349, 1981.
- Stormer, J. C., Jr.**
A Practical Two-Feldspar Geothermometer, Amer. Mineral., 60, 1975, 667-674.
- Stormer, J. C., Jr.**
The Effects of Recalculation on Estimates of Temperature and Oxygen Fugacity From Analyses of Multicomponent Iron-Titanium Oxides, Amer. Mineral., 68, 1983, 586-594.
- Van der Plas, L., and Tobl, A. C.**
A Chart for Judging the Reliability of Point Counting Results, Amer. Jour. Sci., 263, 1965, 87-90.
- Vutukuri, V. S., Lama, R. D., and Saluja, S. S.**
Handbook on Mechanical Properties of Rocks-Testing Techniques and Results-Volume I, Series on Rock and Soil Mechanics, V. 2, No. 1, Trans Tech Publications, Clausthal, Germany, 1974.
- Young, E. J., and Powers, H. A.**
Chevkinite in Volcanic Ash, Amer. Mineral., 45, 1960, 875-881.

Table 1. Symbols, Abbreviations, Definitions, and Units

<u>SYMBOL</u>	<u>DEFINITION</u>	<u>UNITS</u>
$\sigma_1, \sigma_2, \sigma_3$	Principal stresses; compressive stresses are positive	MPa
(σ_{ax})	Stress parallel to the sample axis	MPa
$(\sigma_{ax})_u$	Ultimate axial stress	MPa
$\epsilon_1, \epsilon_2, \epsilon_3$	Principal strains; compressive strains are positive	
$\dot{\epsilon}_{ax}$	Axial strain rate (nominal)	s^{-1}
(ϵ_{ax})	Strain parallel to the sample axis	
$(\epsilon_{ax})_u$	Axial strain at ultimate axial stress	
ϵ_{lat}	Strain perpendicular to the sample axis	
E	Elastic constant : Young's modulus	GPa
ν	Elastic constant : Poisson's ratio	
ϕ	Porosity	%
n	Effective porosity (porosity + clay volume)	%
ρ_g	Average grain density	$\frac{g}{cm^3}$
ρ_{db}	Dry bulk density	$\frac{g}{cm^3}$
ρ_{sb}	Saturated bulk density	$\frac{g}{cm^3}$
f	Force	N
	f_a : actual force	
	f_m : measured force	
δ	Displacement	mm
	δ_a : actual displacement	
	δ_m : measured displacement	
e_m	Error of the measured value (e.g., $100 (f_m - f_a)/f_a$)	%
R	Range of a data sample	(varies)
\bar{F}	Mean of a data sample	(varies)
s	Standard deviation of a data sample	(varies)

Table 1. Symbols, Abbreviations, Definitions, and Units (continued)

<u>ABBREVIATION</u>	<u>DEFINITION</u>
P_j	Volume fraction of the j^{th} material component
S_j	Error estimate of the j^{th} material component $j = M, A, \text{ or } L$
M	Matrix material
A	Vapor-phase-altered material
L	Lithophysal material and cavity
T	Total sample ($T = M + A + L$)
EDS	Energy dispersive analysis
JCPDS	Joint Committee on Powder Diffraction Standards
LVDT	Linear variable displacement transducer
NNWSI	Nevada Nuclear Waste Storage Investigations
NTS	Nevada Test Site
NBS	National Bureau of Standards
XRD	X-ray powder diffraction

Table 2. Volume Fraction Results of Point Counting Study

Sample	Counts	P_M	S_M	P_A	S_A	P_L	S_L
1B	323	0.471	0.068	0.356	0.065	0.173	0.052
1D	333	0.462	0.067	0.315	0.062	0.222	0.056
2A	306	0.556	0.070	0.304	0.064	0.141	0.049
3A	322	0.599	0.067	0.261	0.060	0.140	0.047
8A	333	0.586	0.066	0.279	0.060	0.135	0.046
8B	303	0.564	0.070	0.294	0.064	0.142	0.049
8C	336	0.545	0.066	0.277	0.060	0.179	0.051
8D	336	0.545	0.066	0.208	0.054	0.214	0.055
8E	305	0.538	0.070	0.269	0.062	0.193	0.055
8F	334	0.548	0.067	0.326	0.063	0.126	0.044

Notes:

P : Volume fraction

S : Error estimate

M : Matrix

A : Vapor-phase-altered material

L : Lithophysae

Table 3. Volume Fraction Results of Planimetry Study

<u>Sample</u>	<u>P_M</u>	<u>P_A</u>	<u>P_L</u>
8A	0.626	0.306	0.068
8B	0.687	0.201	0.112
8F	0.562	0.323	0.115

Table 4. Bulk Properties of Lithophysal Samples

Sample	P_M	P_A	P_L	$(\rho_{sb})_T$ [$\frac{g}{cm^3}$]	$(\rho_g)_T$ [$\frac{g}{cm^3}$]	$(\rho_g)_M$ [$\frac{g}{cm^3}$]	ϕ_M	ϕ_T	ϕ_A	$(\rho_g)_A$ [$\frac{g}{cm^3}$]
1B	0.471	0.356	0.173	1.99	2.47	2.55	0.089	0.327	0.315	2.33
1D	0.462	0.315	0.222	1.98	2.47	2.55	0.070	0.333	0.251	2.32
2A	0.556	0.304	0.141	2.05	2.52	2.55	0.092	0.309	0.384	2.44
3A	0.599	0.261	0.140	1.93	2.55	2.55	0.069	0.400	0.838	2.55
8A	0.586	0.279	0.135	1.97	2.57	2.55	0.081	0.382	0.715	2.71
8B	0.564	0.294	0.142	2.02	2.50	2.55	0.089	0.320	0.435	2.35
8C	0.545	0.277	0.179	2.03	2.57	2.55	0.079	0.344	0.440	2.63
8D	0.577	0.208	0.214	1.95	2.53	2.55	0.096	0.379	0.527	2.42
8E	0.538	0.269	0.193	2.00	2.55	2.55	0.080	0.355	0.442	2.55
8F	0.548	0.326	0.126	1.98	2.56	2.55	0.091	0.372	0.602	2.60
\bar{x}	0.545	0.289	0.167	1.99	2.53	2.55	0.084	0.352	0.495	2.49
s	0.045	0.041	0.035	0.04	0.04	0.00	0.009	0.030	0.180	0.14

Notes:

P : Volume fraction

M : Matrix

A : Vapor-phase-altered

L : Lithophysae

T : Total

ϕ : Porosity

ρ_{sb} : Saturated bulk density

ρ_g : Grain density

\bar{x} : Mean

s : Standard deviation

Table 5. Effect of Grain Density Variation on Calculated Properties

Sample	P_M	P_A	P_L	$(\rho_{sb})_T$ [$\frac{g}{cm^3}$]	$(\rho_g)_T$ [$\frac{g}{cm^3}$]	$(\rho_g)_M$ [$\frac{g}{cm^3}$]	ϕ_M	ϕ_T	ϕ_A	$(\rho_g)_A$ [$\frac{g}{cm^3}$]
1B	0.471	0.356	0.173	1.99	2.49	2.55	0.089	0.335	0.337	2.38
1D	0.462	0.315	0.222	1.98	2.49	2.55	0.070	0.342	0.278	2.38
2A	0.556	0.304	0.141	2.05	2.52	2.55	0.092	0.309	0.384	2.44
3A	0.599	0.261	0.140	1.93	2.55	2.55	0.069	0.400	0.838	2.55
8A	0.586	0.279	0.135	1.97	2.55	2.55	0.081	0.374	0.687	2.55
8B	0.564	0.294	0.142	2.02	2.52	2.55	0.089	0.329	0.465	2.42
8C	0.545	0.277	0.179	2.03	2.55	2.55	0.079	0.335	0.408	2.55
8D	0.577	0.208	0.214	1.95	2.53	2.55	0.096	0.379	0.527	2.42
8E	0.538	0.269	0.193	2.00	2.55	2.55	0.080	0.355	0.442	2.55
8F	0.548	0.326	0.126	1.98	2.54	2.55	0.091	0.364	0.577	2.43
\bar{x}	0.545	0.289	0.167	1.99	2.53	2.55	0.084	0.352	0.494	2.47
s	0.045	0.041	0.035	0.04	0.02	0.00	0.009	0.027	0.169	0.07

Notes:

P : Volume fraction
M : Matrix
A : Vapor-phase-altered
L : Lithophysae
T : Total

ϕ : Porosity
 ρ_{sb} : Saturated bulk density
 ρ_g : Grain density
 \bar{x} : Mean
s : Standard deviation

Table 6. Mechanical Properties of Lithophysal Topopah Spring Tuff

Sample	$\dot{\epsilon}_{ax}$ [s ⁻¹]	E [GPa]	ν	$(\sigma_{ax})_u$ [MPa]	$(\epsilon_{ax})_u$ [milli]
1B	1.4×10^{-5}	14.2	0.14	14.5	1.09
1D	1.2×10^{-5}	10.9	0.14	10.3	1.01
2A	0.8×10^{-5}	11.9	0.16	12.4	1.20
3A	1.2×10^{-5}	12.9	0.14	12.0	1.09
8A	0.9×10^{-5}	16.6	0.14	18.2	1.35
8B	0.8×10^{-5}	16.8	0.18	17.4	1.49
8C	0.9×10^{-5}	15.8	0.13	18.5	1.29
8D	0.8×10^{-5}	18.3	0.13	17.5	1.10
8E	0.8×10^{-5}	15.8	0.21	13.8	1.16
8F	0.8×10^{-5}	21.5	0.21	27.8	1.53
R	$0.8-1.4 \times 10^{-5}$	10.9-21.5	0.13-0.21	10.3-27.8	1.01-1.53
\bar{x}	0.96×10^{-5}	15.5	0.16	16.2	1.23
s	0.22×10^{-5}	3.2	0.03	5.0	0.18

Notes:

$\dot{\epsilon}_{ax}$: Axial strain rate

E : Young's modulus

ν : Poisson's ratio

$(\sigma_{ax})_u$: Ultimate axial stress

$(\epsilon_{ax})_u$: Axial strain at ultimate axial stress

R : Range

\bar{x} : Mean

s : Standard deviation

Table 7. Relative Proportions of Porosity from the Three Material Components

Sample	ϕ_T	$P_M \times \phi_M$	$\frac{P_M \times \phi_M}{\phi_T}$	$P_A \times \phi_A$	$\frac{P_A \times \phi_A}{\phi_T}$	$P_L \times \phi_L$	$\frac{P_L \times \phi_L}{\phi_T}$
1B	0.335	0.042	0.125	0.120	0.358	0.173	0.516
1D	0.342	0.032	0.094	0.088	0.257	0.222	0.649
2A	0.309	0.051	0.165	0.117	0.379	0.141	0.456
3A	0.400	0.041	0.103	0.219	0.548	0.140	0.350
8A	0.374	0.047	0.126	0.192	0.513	0.135	0.361
8B	0.329	0.050	0.152	0.137	0.416	0.142	0.432
8C	0.335	0.043	0.128	0.113	0.337	0.179	0.534
8D	0.379	0.055	0.145	0.110	0.290	0.214	0.565
8E	0.355	0.043	0.121	0.119	0.335	0.193	0.544
8F	0.364	0.050	0.137	0.188	0.516	0.126	0.346

Notes:

P : Volume fraction
 ϕ : Porosity

M : Matrix
A : Vapor-phase-altered
L : Lithophysae
T : Total

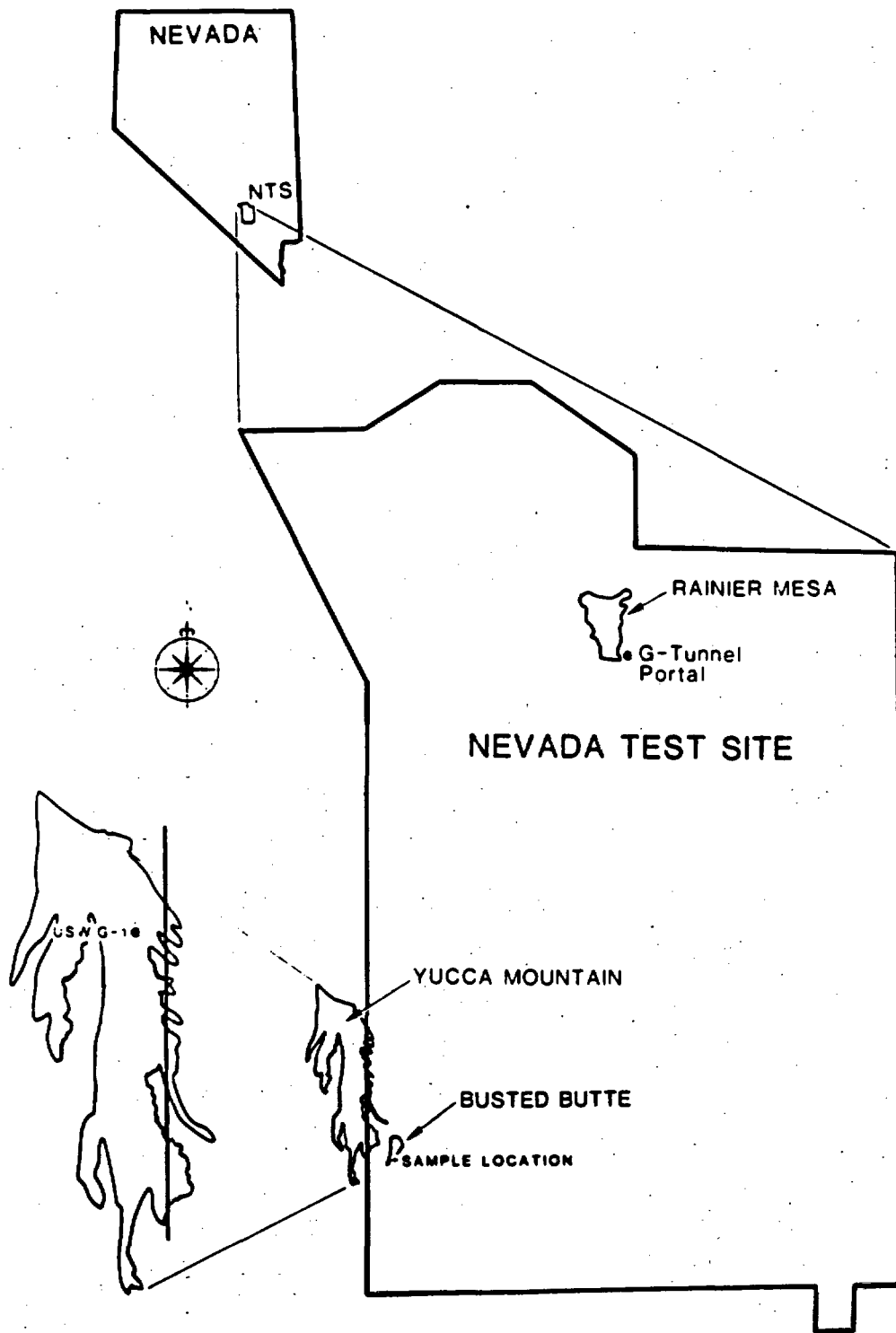


Figure 1.

Location map of the Nevada Test Site, Yucca Mountain, Busted Butte, Rainier Mesa, and G-Tunnel.

FORMATION	MEMBER	LITHOLOGIC SUBUNITS	OBSERVED RANGE OF THICKNESS (meters)	
PAINTBRUSH TUFF	TIVA CANYON		0-129	
	YUCCA MOUNTAIN		0-30	
	PAH CANYON		5-80	
	TOPOPAH SPRING	VITRIC	↑	2-14
		LITHOPHYSAE-RICH		80-244
			
		LITHOPHYSAE-POOR		43-190
		RRRRRRRRRRRR		
VITROPHYRE		11-25		
NONWELDED ASH FLOWS AND BEDDED		14-44		
TUFFACEOUS BEDS OF CALICO HILLS			45-289	

THICKNESS SHOWN IS APPROXIMATELY 767 m

*APPROXIMATE LOCATION OF LITHOPHYSAL HORIZON DISCUSSED IN THIS REPORT

^APPROXIMATE LOCATION OF PROPOSED REPOSITORY HORIZON

Figure 2.
Stratigraphy of Yucca Mountain.

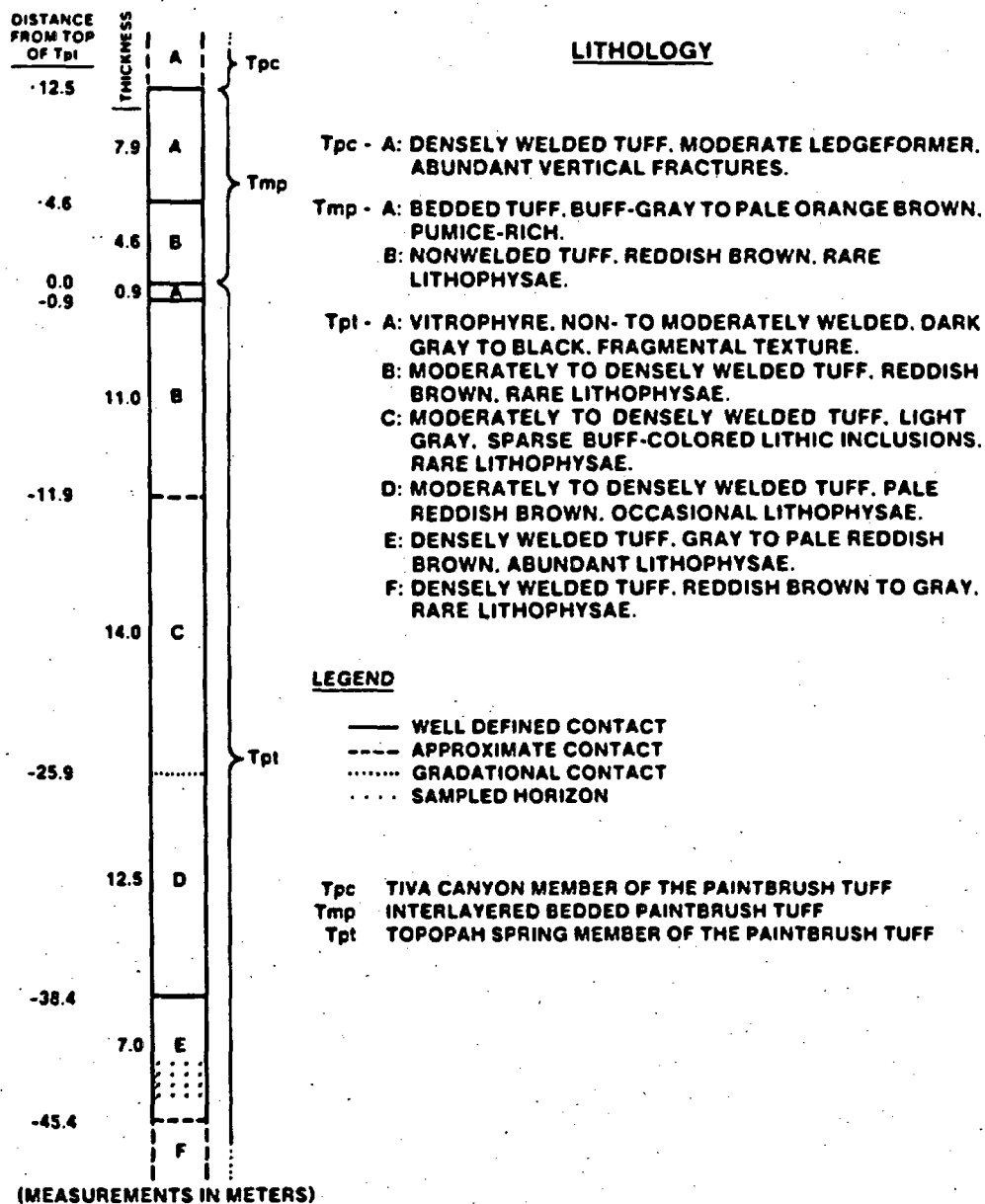


Figure 3.

Measured section of the tuffs at the sample outcrop on the southeast flank of Busted Butte.



Figure 4.

Photomicrograph of devitrified shard matrix, showing strong preferred orientation and deformation, indicative of moderate to dense welding. Sample 2a-1; plane polarized, transmitted light.

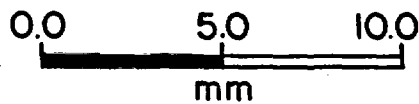
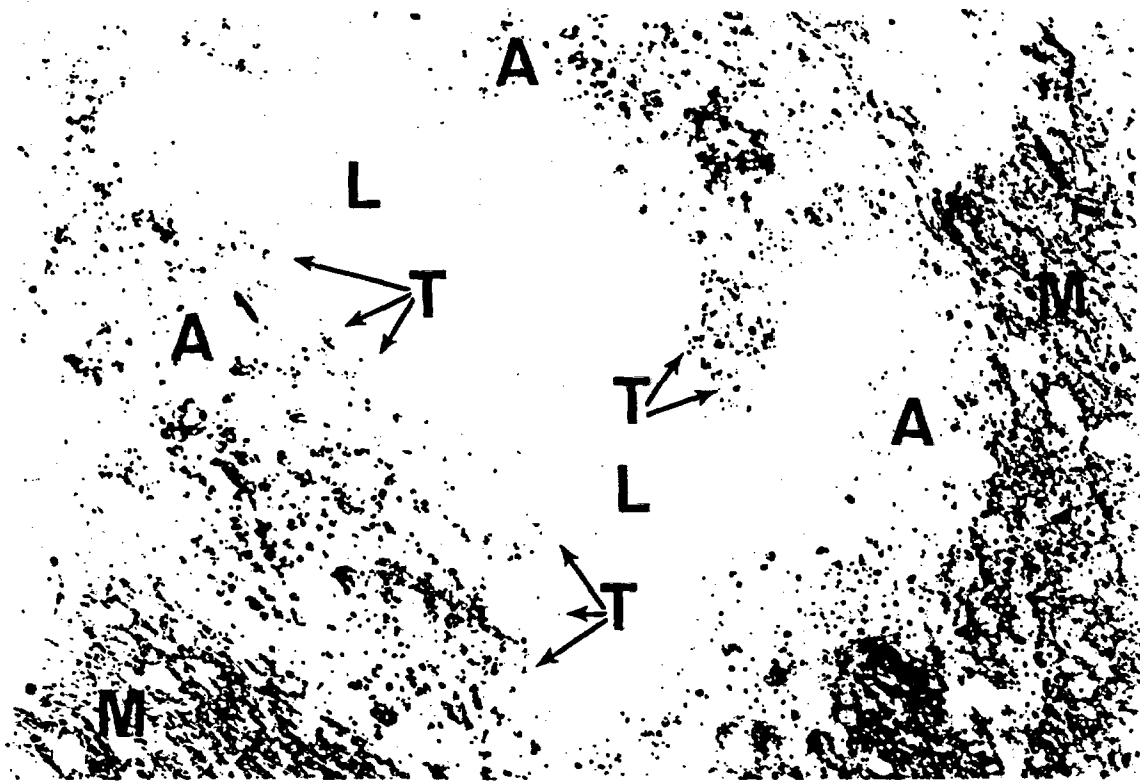


Figure 5.

Photomicrograph of polished thin section of lithophysal tuff, showing a central lithophysa (L) with a rim of vapor-deposited tridymite (T), a zone of vapor-phase-alteration (A) and darker devitrified shard matrix (M). Note the abundant porosity in the vapor-phase-altered matrix and deformation of shard matrix around the lithophysa and altered zone. Sample 1B-1; plane polarized, transmitted light.

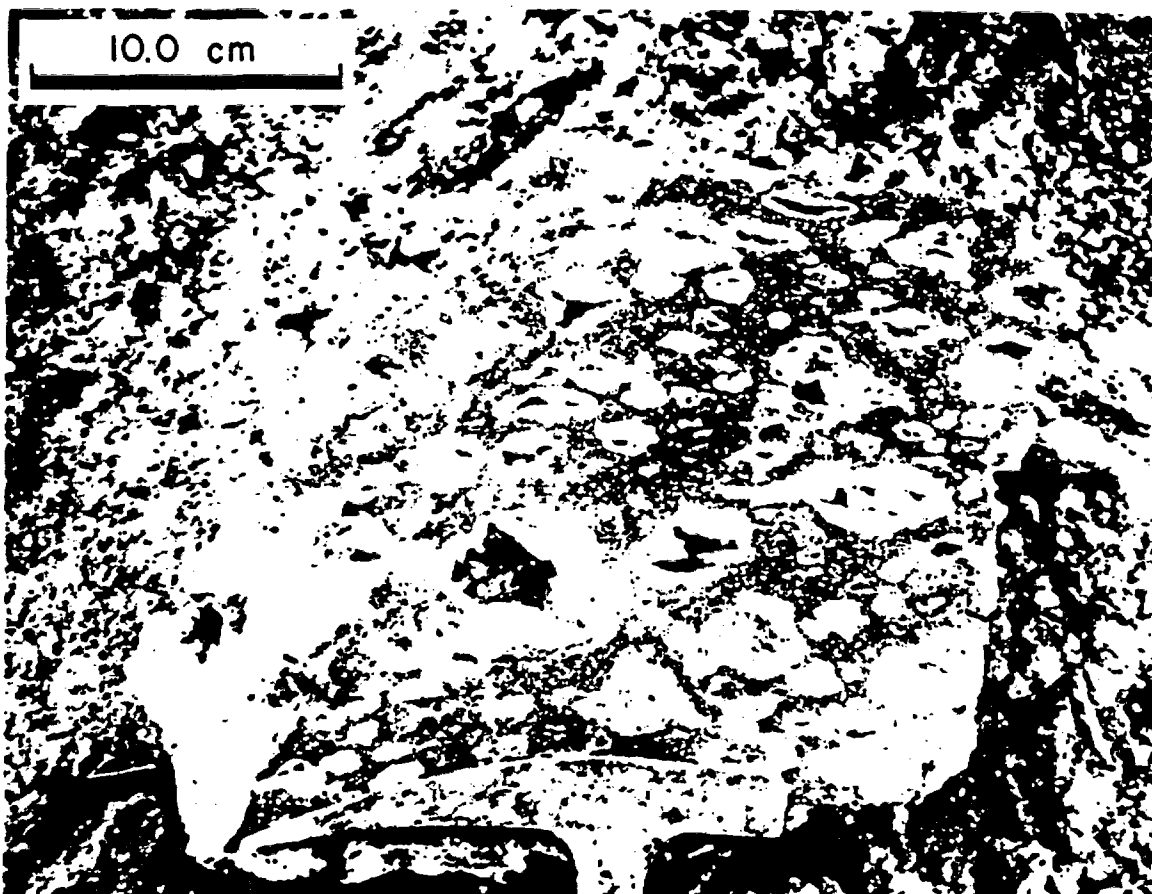


Figure 6.

Hand specimen of lithophysal tuff from Busted Butte, showing macroscopic appearance of lithophysae.

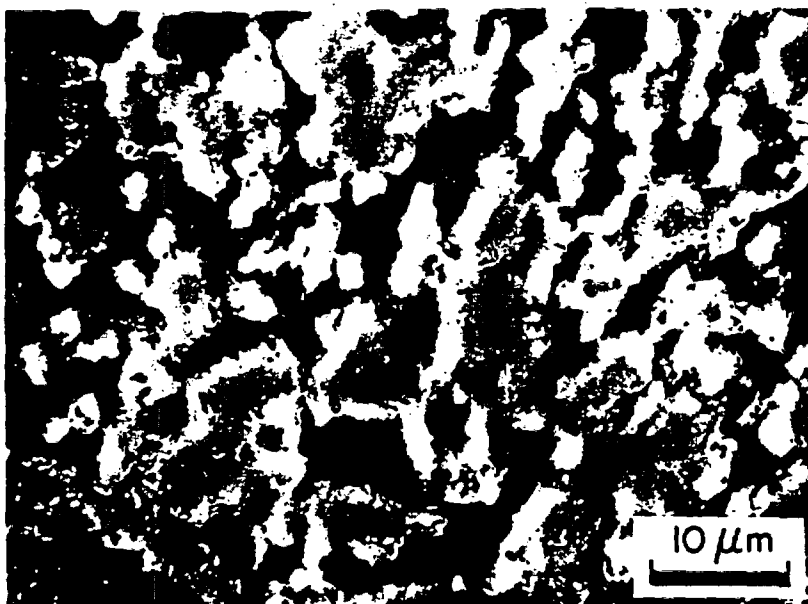


Figure 7.

SEM secondary electron image of a polished section of the vapor-phase-altered matrix around a lithophysa. Darker areas are pores. Sample 8F-1.

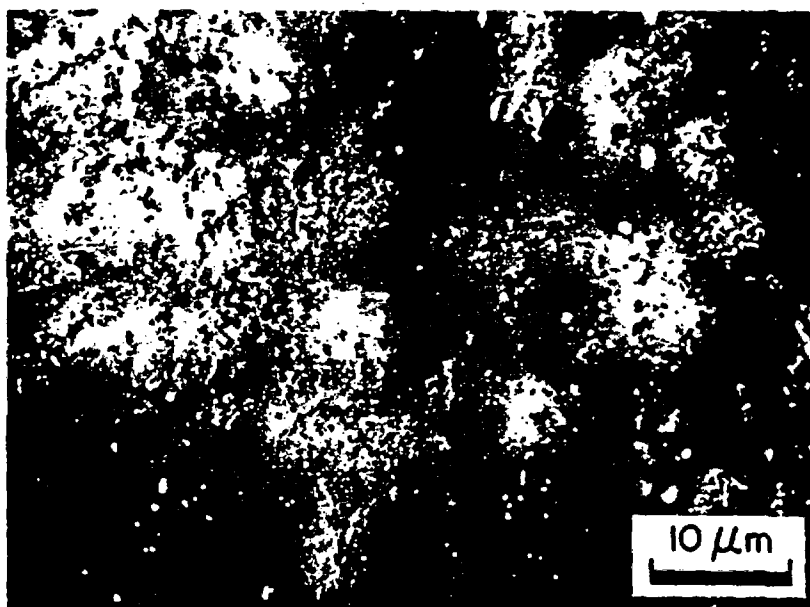


Figure 8.

SEM secondary electron image of a polished section of devitrified matrix. Note absence of porosity in the 5 μm range relative to Figure 7. Sample 8F-1.

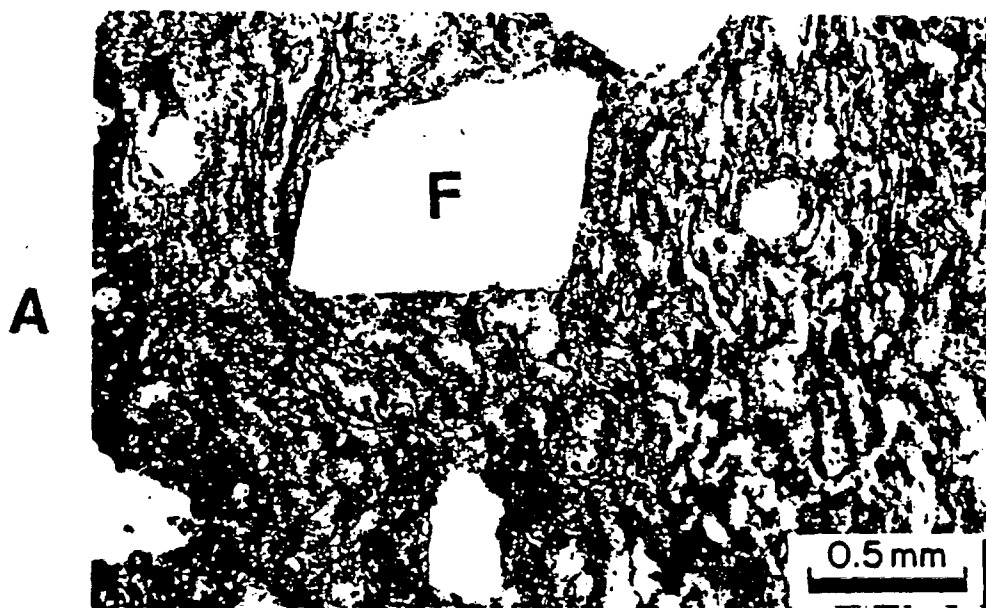


Figure 9.

Photomicrographs of devitrified matrix. [A] Relict shard texture and deformation around rigid feldspar phenocryst (F). Sample 8A-1. Plane polarized, transmitted light. [B] Axiolitic devitrification of shards and local spherulite development in same area as A. Sample 8A-1. Crossed polarizers, transmitted light.

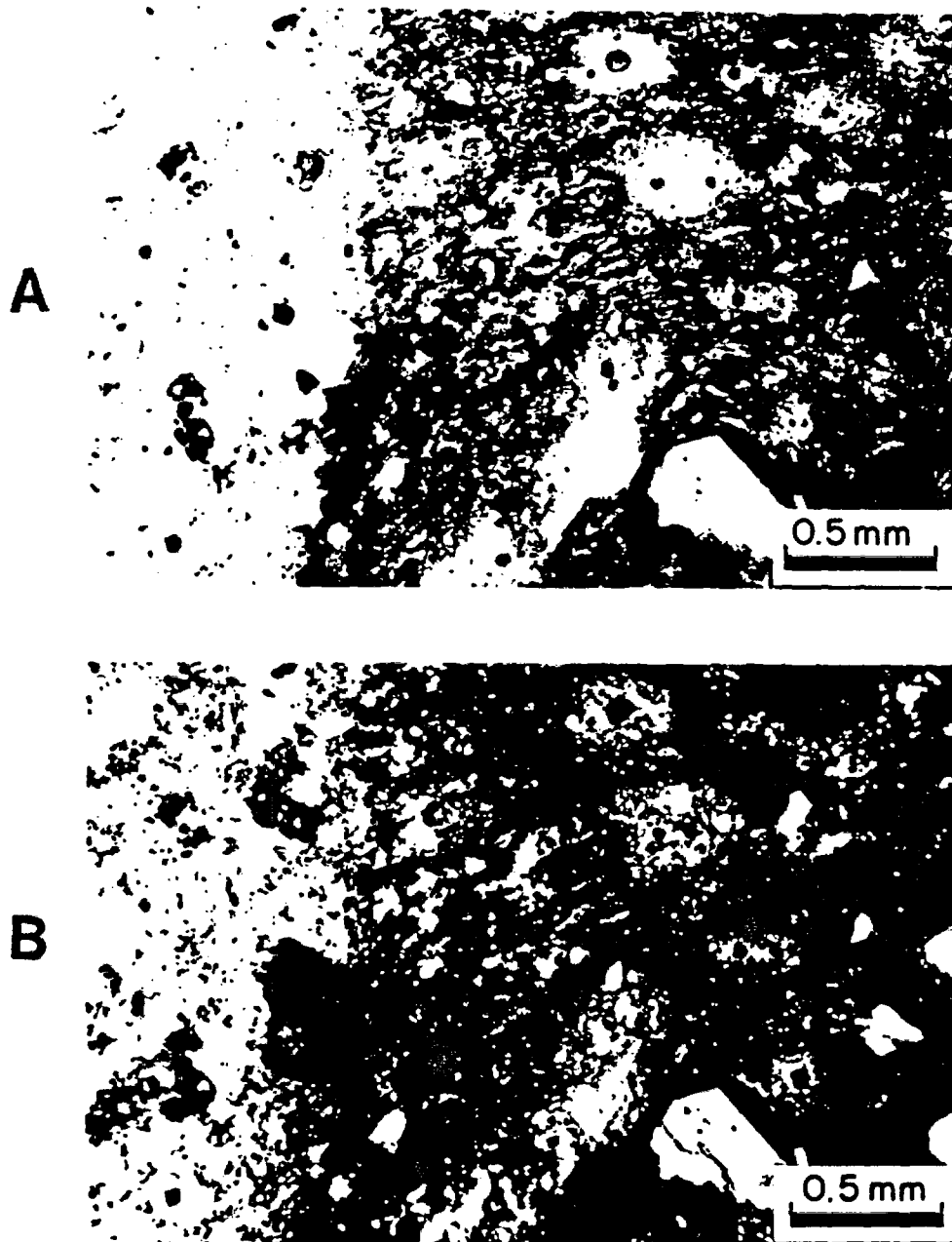


Figure 10.

Photomicrographs showing types of crystallization in lithophysal tuff. Light area on left is vapor-phase-altered matrix around a lithophysa. Darker area is devitrified shard matrix. Note presence of vapor-phase-altered "lenses" within the devitrified matrix. Sample 1D-1. [A] Plane polarized, transmitted light. [B] Crossed polarizers, transmitted light.

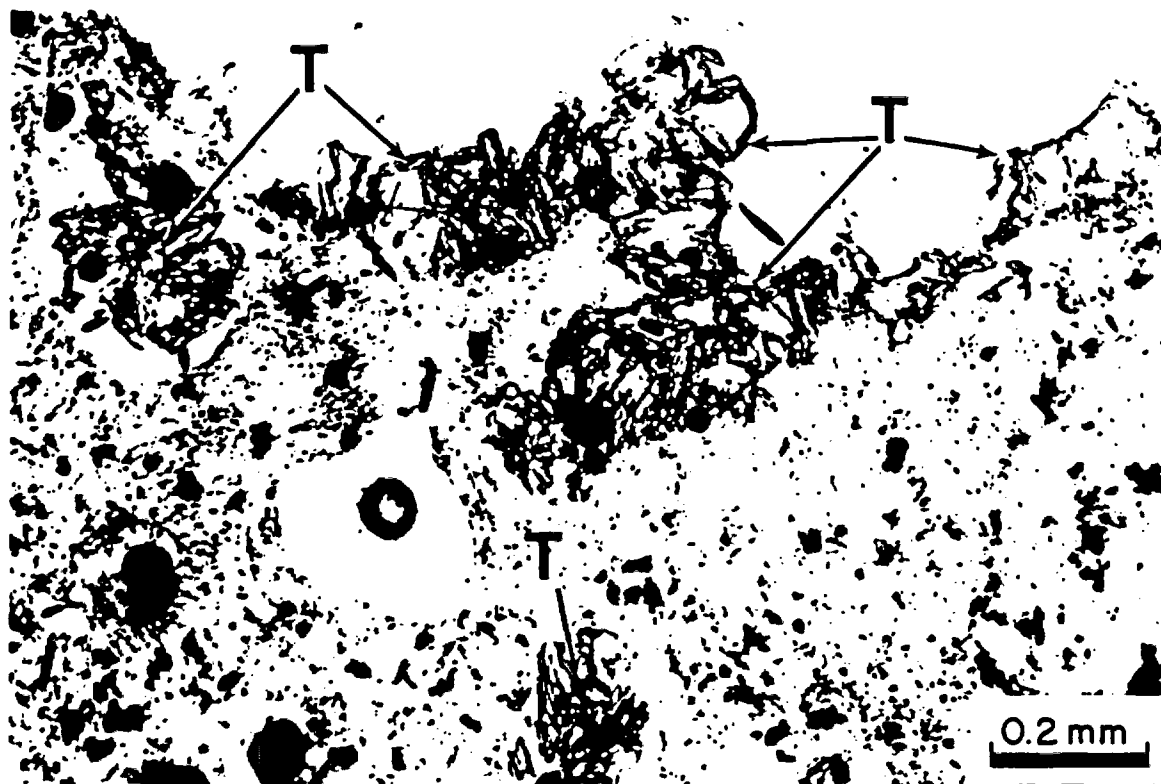


Figure 11.

Photomicrograph of vapor-phase-altered matrix, showing vapor-deposited tridymite (T) around a cavity rim and in pores in altered material. Sample 1D-1. Plane polarized, transmitted light.

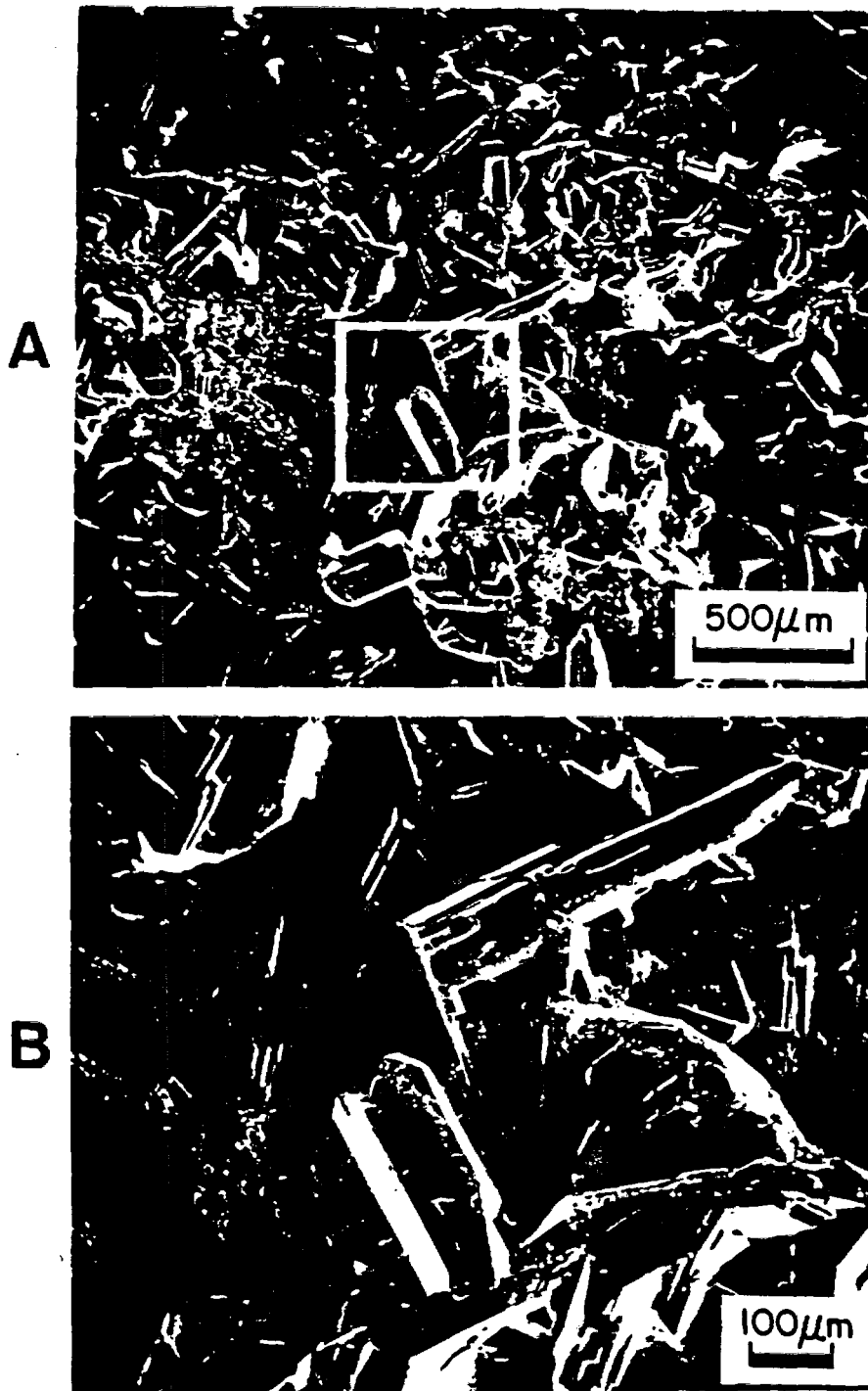


Figure 12.

Vapor-deposited tridymite in lithophysal tuff from 153.8 m (504.6 ft) depth in drill hole USW G-1. SEM secondary electron images of the wall of a lithophysal cavity. The square on [A] shows the approximate location of [B].

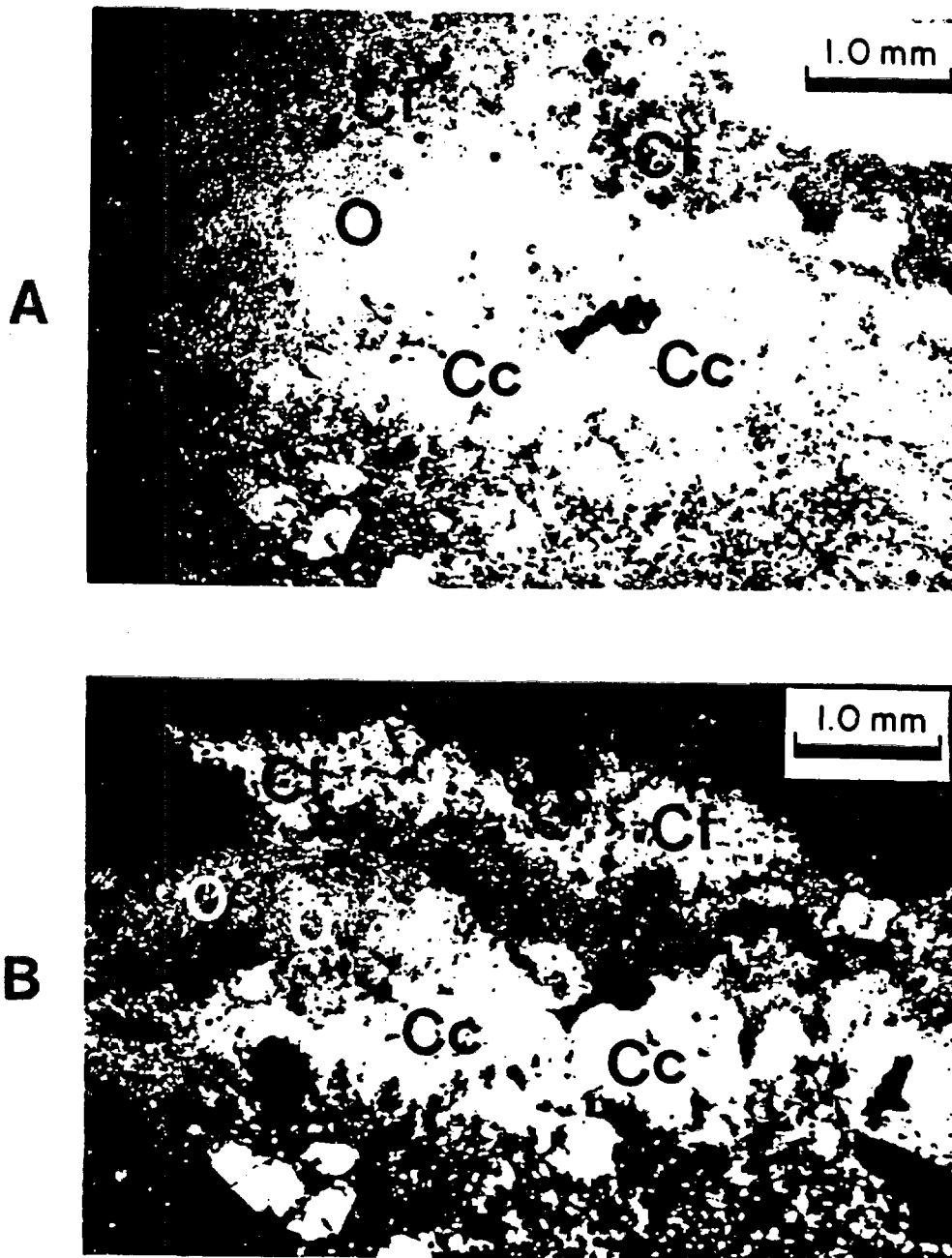


Figure 13.

Photomicrographs of surface-deposited fill material in lithophysal cavity including coarsely crystalline (Cc) and finely crystalline (Cf) calcite, and opal CT (O). Sample 2A-1. [A] Plane polarized, transmitted light. [B] Crossed polarizers, transmitted light.

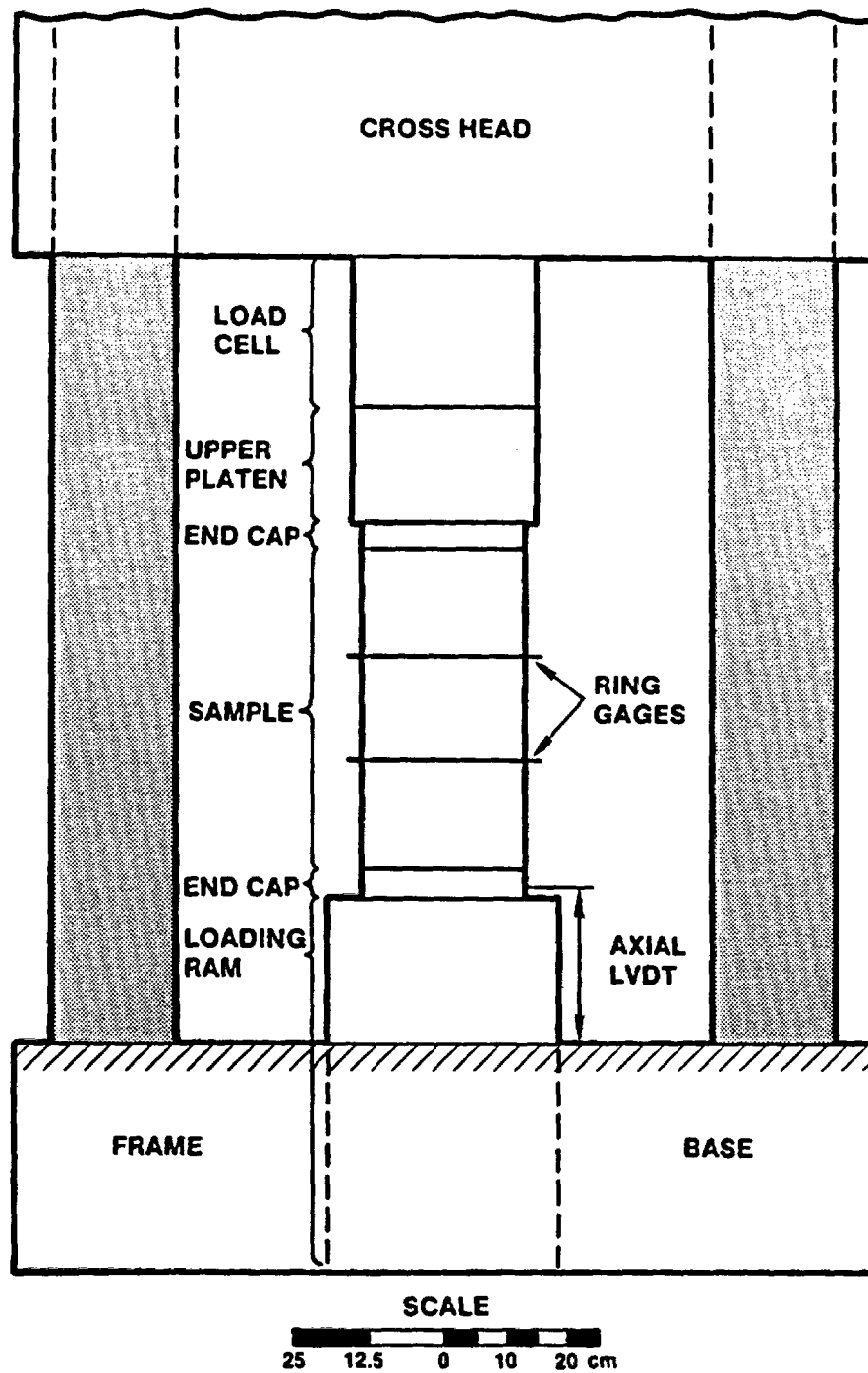


Figure 14.

Diagram of mechanical property test apparatus, including the relative size and location of the sample, and the location of the data acquisition devices.

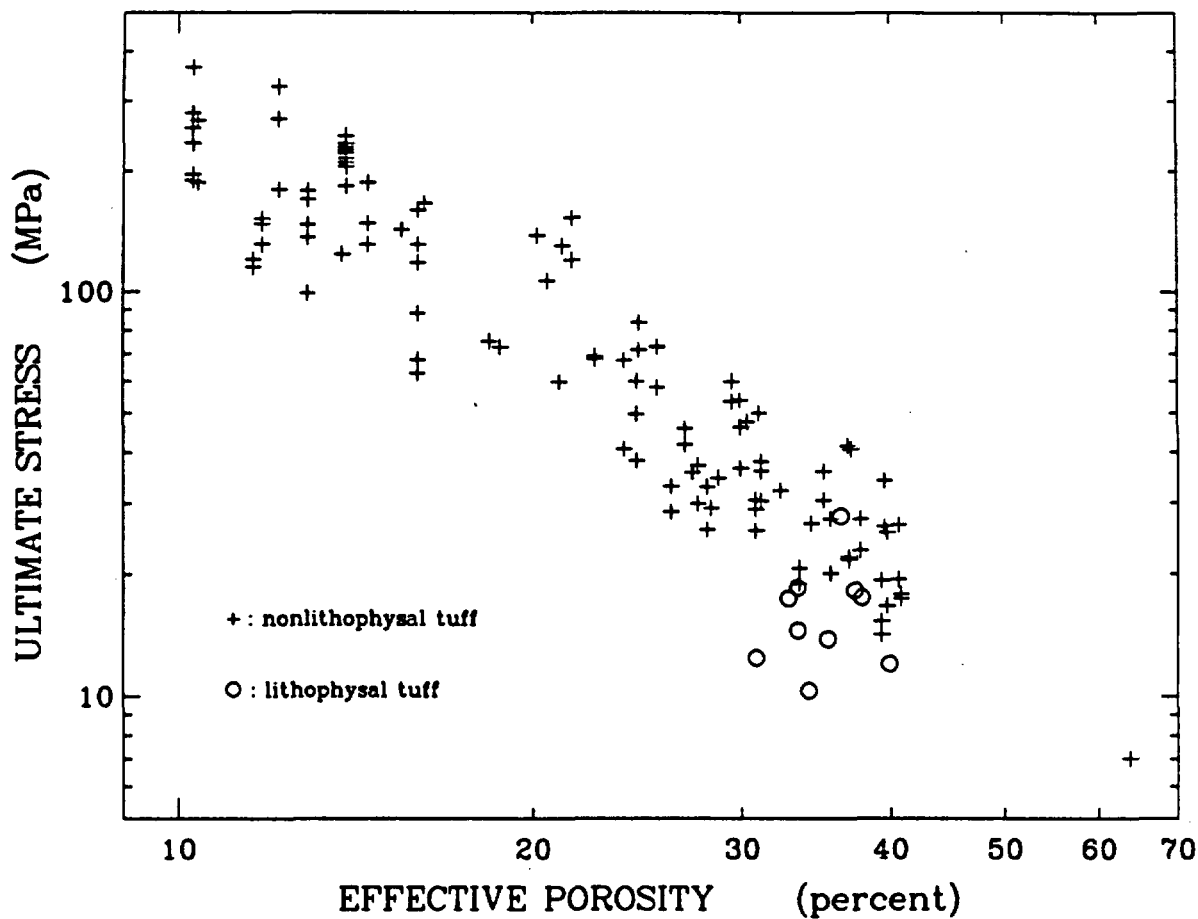


Figure 15.

A plot of ultimate stress as a function of effective porosity for both the nonlithophysal and lithophysal tuff. All experiments were run on saturated samples under unconfined, room temperature and 10^{-5} s^{-1} conditions.

APPENDIX A

This appendix exclusively consists of petrologic data tables from the individual studies on the Topopah Spring Member lithophysal samples. Table A-1 lists the XRD (x-ray powder diffraction) results, and Tables A-2 to A-9 present all of the electron microprobe analysis data.

Sample : 3A-Devit

Description: Obtained by crushing approximately 30 gram sample of homogeneous phenocryst poor, reddish-brown, devitrified matrix.

Peak locations degrees 2 θ

20.9 21.9 23.5 25.7 26.55 27.7 28.3 29.8 31.2

Relative intensities

10 100 27 19 40 70 15 15 15

The strongest peak at 21.9° and another peak at 28.3° and 31.2° are cristobalite.

The peaks at 26.55° and 20.9° are quartz.

The peaks at 23.5°, 25.7°, 27.7°, and 29.8° are feldspars, probably sanidine and an Na-rich alkali feldspar.

Sample : 8E-Devit

Description: Obtained by crushing approximately 30 gram sample of homogeneous, phenocryst-poor reddish brown devitrified matrix.

Peak locations- degrees 2 θ

21.9 23.55 25.75 26.6 26.95 27.7 29.85 31.3

Relative intensities

100 22 12 17 19 52 12 10

The strongest peak at 21.9° and another peak at 31.3° are cristobalite.

The peak at 26.6° is quartz.

The peaks at 25.75°, 26.95°, 27.7°, and 29.85° are feldspars, probably a K-rich sanidine and possibly albite.

Sample : 3A-Vap Ph

Description: Light gray powder scraped from vapor-phase altered rim from several small lithophysae.

Peak locations- degrees 2 θ

20.8 21.8 23.6 26.7 27.1 27.6 27.8 28.1 29.5

Relative intensities

5 100 8 11 6 9 11 5 5

Peaks at 21.8 , 20.8, and 26.7 are a tridymite-dominated mixed cristobalite/tridymite.

Relative intensities suggest this is strongly dominant.

Peaks at 26.6 , 27.1 , 27.6 , 27.8 , and 28.1 are feldspars, probably a sanidine and Na-rich plagioclase.

Sample : 1B-Vap Ph

Description: Light gray powder scraped from 1 by 2.3 cm altered area around lithophysae.

Peak locations- degrees 2θ

20.9 21.8 23.6 26.6 27.0 27.5 27.6 27.7

Relative intensities

20 100 40 90 35 50 50 50

The peaks at 20.9°, 21.8°, and 26.6° are tridymite and/or mixed cristobalite/tridymite.

The peak at 26.6° probably indicates some quartz present with tridymite.

Peaks at 23.6°, 27.0°, 27.5°, 27.6°, and 27.7° are feldspars, probably anorthoclase and a K-rich feldspar.

Sample : 8B-Vap Ph

Description: Scraped from vapor-phase altered material around lithophysae with abundant needle-like clear crystals (tridymite?).

Peak locations- degrees 2θ

20.8 21.8 23.4 23.6 26.65 27.0 27.65 27.75 29.4 29.9

Relative intensities

40 85 35 40 100 40 70 67 20 22

The peaks at 20.8°, 21.8°, 23.4°, 27.65° (in part), and numerous minor peaks not listed above are tridymite.

Peaks at 20.8° (in part) and 26.65° are quartz.

Peaks at 23.6°, 27.0°, 27.75°, and 29.9° are feldspar.

The peak at 29.4° is minor calcite.

Sample : 1D-Vap Ph

Description: Gray powder scraped from altered material around large (1 cm +) lithophysa.

Peak locations- degrees 2θ

20.75 20.85 21.8 23.7 26.7 27.0 27.1 27.6 27.7 29.45

Relative intensities

20 20 100 40 90 40 30 80 100 10

The peaks at 20.85°, 21.8°, and possibly 20.75° are tridymite.

Most remaining peaks (23.7°, 26.7°, 27.0°, 27.1°, 27.6°, and 27.7°) are

feldspars, probably an Na-rich anorthoclase and a K-rich alkali feldspar.

The minor peak at 29.45° is calcite.

Sample : 2A-Fill

Description: Pale buff to white material with local brown specks scraped from interior fill in two lithophysae.

Peak locations degrees 2 θ

7.3 20.6-20.7 21.6-21.8 26.6 27.95 29.45 34.85 36.0

Relative intensities

50 30 35 45 20 100 20 15

The peaks at 29.45° and 36.0° are calcite.

The peak at 7.3°, and subordinate peaks at 20.6°-20.7°, 27.95°, and 34.85° are a poorly crystalline 12 Å clay, probably a smectite.

The broad peak at 20.6°-20.7° is opal-CT.

Sample : 1B-Fill

Description: Pale buff to white powder scraped from 2.5 cm diameter pore. Material coats vapor-phase altered gray material.

Peak locations- degrees 2 θ

21.6 (very broad) 29.45 36.0 39.45

Relative intensities

25 100 15 15

The peaks at 29.45°, 36.0°, and 39.45° are calcite.

The broad peak centered at 21.6° is opal-CT.

Table A-2: Electron Microprobe Analyses (in wt. percent) and Molecular Endmembers of Alkali Feldspar Phenocrysts

<u>Analysis</u>	<u>1</u>	<u>2</u>	<u>3</u>	<u>4</u>	<u>5</u>	<u>6</u>	<u>7</u>	<u>8</u>	<u>9</u>	<u>10</u>	<u>11</u>
Sample	1B-2	1B-2	1B-1	1B-1	1D-1	1D-1	8C-1	8C-1	8F-1	8F-1	G1 448.9A
No. of points averaged	17	13	14	11	14	18	13	6	24	9	6
<u>Oxide</u>											
SiO ₂	65.8	65.9	65.4	65.7	65.6	65.5	65.2	65.7	65.4	65.2	67.8
Al ₂ O ₃	19.1	19.2	19.1	19.2	19.0	19.0	19.0	19.1	19.1	19.1	19.2
FeO	0.21	0.16	0.20	0.23	0.19	0.18	0.19	0.11*	0.17	0.17	0.16
BaO	0.18	0.23	0.17	0.22	0.11	0.17	0.15	0.12	0.11	0.09	0.09
CaO	0.62	0.68	0.63	0.69	0.60	0.55	0.63	0.59	0.56	0.61	0.52
Na ₂ O	5.19	5.44	5.41	5.63	5.35	5.39	5.47	5.39	5.40	5.58	5.45
K ₂ O	9.05	8.68	8.61	8.36	8.73	8.62	8.92	9.06	8.99	8.46	5.38
Total wt. %	100.2	100.3	99.5	100.0	99.6	99.4	99.6	100.0	99.7	99.2	98.6
An	3.0	3.3	3.0	3.3	2.9	2.7	3.0	2.8	2.7	2.9	3.1
Ab	45.2	47.2	47.4	48.9	46.8	47.4	46.8	46.2	46.4	48.6	58.7
Or	51.8	49.5	49.6	47.8	50.3	49.9	50.2	51.0	50.9	48.5	38.2
Molecular Na/K	0.872	0.952	0.955	1.02	0.931	0.950	0.932	0.904	0.913	1.00	1.54
Alpaite index	0.959	0.955	0.954	0.953	0.960	0.957	0.982	0.977	0.974	0.960	0.770
Notes:	1	2	1	2	1	2	1	2	1	2	1,2

Notes: * : Below detection limit, not included in analytical totals. MnO and MgO are below detection limit in all analyses.

1 : In devitrified matrix.

2 : In vapor phase altered material.

Table A 3: Electron Microprobe Analyses (in wt. percent) and Molecular Endmembers of Plagioclase Phenocrysts

Analysis	<u>1</u>	<u>2</u>	<u>3</u>	<u>4</u>	<u>5</u>	<u>6</u>	<u>7</u>	<u>8</u>	<u>9</u>	<u>10</u>	<u>11</u>	<u>12</u>	<u>13</u>	<u>14</u>	<u>15</u>
Sample	1B-2	1B-2	1B-1	1B-1	1D-1	1D-1	1D-1	8C-1	8C-1	8C-1	8F-1	8F-1	8F-1	GI-448.9A	GI-448.9A
No. of points averaged	5	1	10	14	9	6	1	2	10	1	1	10	3	6	2
Oxide															
SiO ₂	63.8	58.6	63.1	63.1	63.1	63.5	58.7	63.2	63.5	58.6	63.0	62.8	55.7	65.4	61.2
Al ₂ O ₃	22.0	25.6	22.2	22.3	22.2	22.1	25.3	22.5	21.9	26.0	22.7	22.2	27.0	21.9	24.9
FeO	0.28	0.0*	0.20	0.22	0.19	0.24	0.24	0.10*	0.10*	0.04*	0.10*	0.23	0.32	0.15	0.02*
BaO	0.07	0.07	0.04*	0.02*	0.04*	0.05	0.10	0.01*	0.05	0.01*	0.0*	0.01*	0.07	0.03*	0.06
CaO	3.77	7.77	3.93	4.04	3.88	3.64	7.38	3.92	3.58	7.60	4.08	3.98	9.35	2.72	5.25
Na ₂ O	8.51	6.98	8.59	8.51	8.72	8.44	7.08	8.82	8.87	6.98	9.01	8.82	6.19	8.28	7.07
K ₂ O	1.82	0.59	1.32	1.51	1.51	1.79	0.52	1.31	1.56	0.70	1.14	1.29	0.41	1.19	0.51
Total wt. %	100.3	99.6	99.3	99.7	99.6	99.8	99.3	99.8	99.5	99.9	99.9	99.3	99.0	99.6	99.0
An	17.7	36.8	18.7	19.0	18.1	17.3	35.4	18.3	16.7	36.1	18.8	18.5	44.5	14.2	28.1
Ab	72.2	59.9	73.8	72.5	73.5	72.6	61.6	74.4	74.7	60.0	75.0	74.3	53.2	78.4	68.6
Or	10.1	3.3	7.5	8.5	8.4	10.1	3.0	7.3	8.6	3.9	6.2	7.2	2.3	7.4	3.3
Molecular Na/K	7.11	17.9	9.89	8.56	8.78	7.16	20.7	10.2	8.64	15.2	12.0	10.4	22.9	10.6	21.1
Alpaitic index	0.726	0.473	0.701	0.701	0.720	0.716	0.482	0.708	0.743	0.471	0.707	0.716	0.393	0.681	0.489
Notes:	1	3	1	2	1	2	3	1	2	3	1	2	3	1,2	3

Notes: * : Below detection limit, not included in analytical totals. MnO and MgO are below detection limit in all analyses.
 1 : In devitrified matrix.
 2 : In vapor phase altered material.
 3 : Ca rich, K poor plagioclase, typically as distinct phenocryst core.

Table A 4: Electron Microprobe Analyses (in wt. percent) of Mafic Silicates

<u>Analysis</u>	<u>1</u>	<u>2</u>	<u>3</u>	<u>4</u>
Sample	8E-1	2A-2	2A-2	2A-2
No. of points averaged	10	2	2	3
<u>Oxide</u>				
SiO ₂	35.3	34.1	34.0	51.4
TiO ₂	4.01	4.61	3.98	0.22
Al ₂ O ₃	13.0	12.3	12.1	0.93
FeO	16.0	19.9	23.0	8.87
MnO	0.76	0.94	1.07	1.64
MgO	16.4	15.1	12.0	13.3
CaO	0.04	0.29	0.71	20.9
Na ₂ O	0.67	0.59	0.52	0.57
K ₂ O	7.00	7.67	7.38	0.0*
Total wt. %	93.2	95.5	94.8	97.8

Notes: * : Below detection limit, not included in analytical totals. Cr₂O₃ is below detection limit in all analyses.

1-3 : Biotite.

4 : Clinopyroxene.

Table A-5: Electron Microprobe Analyses (in wt. percent) of Allanite and Chevkinite

Analysis		<u>1</u>	<u>2</u>	<u>3</u>	<u>4</u>	<u>5</u>				
Sample		8D 2	8D-2	2A-2	G1-407.1	G1-407.1				
No. of points averaged		2	4	4	3	3				
<u>Oxide</u>										
SiO ₂		31.3	21.6	21.4	21.7	21.2				
ZrO ₂		0.0*	0.97	0.95	1.27	0.93				
TiO ₂		1.51	18.4	18.5	18.5	18.3				
Al ₂ O ₃		13.1	2.76	2.84	2.93	2.87				
La ₂ O ₃	Total 24.4	6.38	41.0	11.2	40.0	10.9	40.8	11.5	41.7	11.6
Ce ₂ O ₃	REE	12.1	19.3	18.8	19.2	20.2				
Pr ₂ O ₅		2.23	4.14	4.01	4.07	4.04				
Nd ₂ O ₃		3.68	6.31	6.29	6.00	5.90				
FeO		15.8	7.45	7.19	6.83	7.20				
MnO		0.60	0.28	0.24	0.17	0.25				
MgO		0.90	0.90	0.84	0.97	0.94				
CaO		9.45	5.38	5.63	5.85	5.41				
Total wt. %		97.1	98.7	97.6	99.0	98.8				
Total REE		24.4	41.0	40.0	40.8	41.7				

Notes: * : Below detection limit. Not included in analytical totals.

1 : Allanite.

2-5 : Chevkinite.

Table A-6: Electron Microprobe Analyses (in wt. percent) of Fe-Ti Oxides

Analysis	<u>1</u>	<u>2</u>	<u>3</u>	<u>4</u>	<u>5</u>	<u>6</u>	<u>7</u>	<u>8</u>	<u>9</u>	
Sample	8C-1	8C-1	8C-1	8C-1	8C-1	8C-1	8C-1	8C-1	8C-1	
Pt designation	O _{1A}	O _{1B}	O ₂	O ₄	O ₅	O ₆	O ₇	O ₈	VOX-1	
No. analyses averaged	3	1	1	3	2	1		1	21	
Magnetites										
SiO ₂	0.07	0.05	0.01	0.06	0.03	1.16		0.23	0.13	0.13
TiO ₂	8.66	7.95	2.78	9.17	2.00	6.11		2.94	3.35	3.35
Al ₂ O ₃	1.10	1.07	1.63	1.32	1.29	1.08		0.62	0.12	0.12
FeO	83.2	84.5	83.1	83.4	85.4	80.9		89.0	77.4	86.0 (Fe ₂ O ₃)
MnO	1.96	1.84	2.51	1.97	2.52	1.00		0.29	6.61	8.10 (MnO ₂)
MgO	0.27	0.19	0.25	0.09	0.17	0.12		0.02	1.09	1.09
CaO	<u>0.0*</u>	<u>0.0*</u>	<u>0.0*</u>	<u>0.0*</u>	<u>0.0*</u>	<u>0.09</u>		<u>0.02</u>	<u>0.0*</u>	<u>0.0*</u>
Total wt. %	95.3	95.6	90.3	96.0	91.4	90.5		93.1	88.7	98.8
Recalculated										
Fe ₂ O ₃	51.2	53.0	59.2	50.4	62.0	50.2		61.6		
FeO	37.1	36.8	29.8	38.1	29.6	35.8		33.6		
Total wt. %	100.4	100.9	96.2	101.1	97.6	95.5		99.3		
XUSP ⁷	0.247	0.226	0.082	0.264	0.057	0.195		0.088		
No. analyses averaged			3		3	3	3	2		
Ilmenites										
SiO ₂			0.06		0.0*	0.0*	0.02	0.02		
TiO ₂			32.7		33.3	45.4	47.2	44.7		
Al ₂ O ₃			1.62		1.88	0.05	0.03	0.07		
FeO			55.7		54.9	47.7	46.4	48.9		
MnO			1.51		1.95	4.25	4.24	3.82		
MgO			0.25		0.21	0.44	0.48	0.60		
CaO			<u>0.01*</u>		<u>0.0*</u>	<u>0.0*</u>	<u>0.01*</u>	<u>0.03</u>		
Total wt. %			91.8		92.2	97.8	98.4	98.1		
Recalculated										
Fe ₂ O ₃			34.3		30.3	13.3	10.1	15.2		
FeO			27.5		27.6	35.7	37.3	35.2		
Total wt. %			95.0		95.3	99.2	99.4	99.7		
XILM ⁸			0.669		0.678	0.865	0.898	0.846		
Notes:	1	1	4	1	4	3	2	3	5	5,6

Notes: * : Below detection limit; not included in analytical totals or recalculation procedures.
 Cr₂O₃ is always below detection limit; V₂O₅ not analyzed.
 1 : Magnetite, no notable exsolution.
 2 : Ilmenite, no notable exsolution.
 3 : Ilmenite, very slight exsolution.
 4 : Magnetite with exsolved ilmenite lamellae.
 5 : Secondary oxides in vapor-phase-altered material.
 6 : Recalculated all Fe as Fe₂O₃, all Mn as MnO₂.
 7 : XUSP is mole fraction ulvospinel in ulvospinel-magnetite solid solution.
 8 : XILM is mole fraction ilmenite in ilmenite-hematite solid solution.

Table A-7: Defocused Beam Electron Microprobe Analyses (in wt. percent) of Devitrified Matrix

Page 1 of 2

Analysis	1		2		3		4		5		
Sample	1D-1		1D-1		1B-2		1B-1		8C-1		
No. of points averaged	20		13		18		24		21		
<u>Oxide</u>											
SiO ₂	78.0 ± 7.2	78.9	79.4 ± 5.1	80.3	75.3 ± 4.4	78.4	76.5 ± 3.5	78.0	74.0 ± 6.3	75.6	
Al ₂ O ₃	11.4 ± 4.0	11.5	10.7 ± 2.8	10.8	11.2 ± 2.6	11.7	11.8 ± 1.9	12.0	12.7 ± 2.8	13.0	
FeO	0.51 ± 0.52	0.52	0.45 ± 0.38	0.46	0.99 ± 1.09	1.03	0.50 ± 0.32	0.51	0.83 ± 0.42	0.85	
MnO	0.03*	0.03*	0.01*	0.01*	0.03*	0.03*	0.01*	0.01*	0.07 ± 0.06	0.07	
MgO	0.03 ± 0.08	0.03	0.01*	0.01*	0.06 ± 0.06	0.06	0.05 ± 0.05	0.05	0.12 ± 0.10	0.12	
BaO	0.0*	0.0*	0.03*	0.03*	0.05*	0.05*	0.02*	0.02*	0.01*	0.01*	
CaO	0.25 ± 0.08	0.25	0.25 ± 0.07	0.25	0.51 ± 0.28	0.53	0.36 ± 0.18	0.37	0.43 ± 0.21	0.44	
Na ₂ O	3.28 ± 0.96	3.32	3.01 ± 0.73	3.04	3.43 ± 0.97	3.57	3.40 ± 0.67	3.47	3.88 ± 0.93	3.96	
K ₂ O	5.38 ± 2.32	5.45	5.09 ± 1.50	5.15	4.61 ± 1.72	4.80	5.47 ± 1.56	5.58	5.82 ± 1.74	5.94	
Total wt.%	98.8	100.0	98.9	100.0	96.1	100.0	98.1	100.0	97.9	100.0	
An**	2.0		2.1		4.2		2.8		3.0		
Ab**	47.1		46.3		50.8		47.2		48.8		
Or	50.9		51.6		45.0		50.0		48.2		
Na/K	0.926		0.899		1.13		0.945		1.01		
Alpaaitic index	0.984		0.977		0.949		0.975		0.988		
Notes:	1.5	1.4	2.5	2.4	3.5	3.4	3.5	3.4	3.5	3.4	

Notes: * : Below detection limit, not included in analytical totals.

** : Calculated from molecular ratios of CaO, Na₂O, and K₂O for comparison with feldspar analyses.

1 : Axialitic devitrified shard matrix.

2 : Spherulitic devitrified matrix.

3 : Devitrified matrix--all types combined.

4 : Analyses normalized to total of 100 wt.%.

5 : Variation shown (±) is 1 standard deviation for number of analyses averaged.

Table A-7: Defocused Beam Electron Microprobe Analyses (in wt. percent) of Devitrified Matrix Page 2 of 2

Analysis	6		7		8		9	
Sample	8E-1		8F-1		G1-448.9A		G1-504.6	
No. of points averaged	25		24		22		11	
Oxide								
SiO ₂	75.7 ± 2.7	77.6	76.0 ± 3.2	77.5	77.8 ± 4.1	79.3	72.6 ± 3.5	76.8
Al ₂ O ₃	11.9 ± 1.3	12.2	12.0 ± 1.9	12.2	12.1 ± 1.9	12.3	12.6 ± 0.88	13.3
FeO	0.52 ± 0.45	0.53	0.52 ± 0.23	0.53	0.87 ± 0.97	0.88	0.86 ± 1.10	0.91
MnO	0.01*	0.01*	0.03*	0.03*	0.04*	0.04*	0.03*	0.03*
MgO	0.11 ± 0.11	0.11	0.05 ± 0.05	0.05	0.14 ± 0.17	0.14	0.16 ± 0.15	0.17
BaO	0.03*	0.03*	0.01*	0.01*	0.01*	0.01*	0.02*	0.02*
CaO	0.34 ± 0.18	0.35	0.38 ± 0.18	0.39	0.44 ± 0.10	0.45	0.39 ± 0.17	0.42
Na ₂ O	3.57 ± 0.39	3.66	3.58 ± 0.71	3.65	3.67 ± 0.64	3.73	3.48 ± 0.53	3.68
K ₂ O	5.38 ± 1.26	5.51	5.55 ± 1.42	5.66	3.11 ± 0.74	3.17	4.41 ± 0.93	4.67
Total wt. %	97.5	100.0	98.1	100.0	98.1	100.0	94.5	100.0
An**	2.6		2.8		4.1		3.3	
Ab**	48.9		48.1		61.6		52.7	
Or**	48.5		49.1		34.3		44.0	
Na/K	1.01		0.980		1.79		1.20	
Alpaitic index	0.983		0.991		0.777		0.833	
Notes:	3.5	3.4	3.5	3.4	3.5	3.4	3.5	3.4

Notes: * : Below detection limit, not included in analytical totals.

** : Calculated from molecular ratios of CaO, Na₂O, and K₂O for comparison with feldspar analyses.

1: Axialitic devitrified shard matrix.

2: Spherulitic devitrified matrix.

3: Devitrified matrix--all types combined

4: Analyses normalized to total of 100 wt. %.

5: Variation shown (±) is 1 standard deviation for number of analyses averaged.

Table A-8: Defocused Beam Electron Microprobe Analyses (in wt. percent) of Vapor-Phase-Altered Matrix

Analysis	1		2		3		4		5	
Sample	1D-1		1D-1		1B-2		1B-4		8C-1	
No. of points averaged	16		21		10		18		14	
Oxide										
SiO ₂	73.1 ± 14.6	78.4	77.3 ± 16.8	82.9	78.9 ± 3.6	79.5	76.5 ± 11.9	79.0	63.1 ± 8.3	69.1
Al ₂ O ₃	11.2 ± 5.4	12.0	8.80 ± 6.50	9.44	10.8 ± 1.7	10.0	11.2 ± 6.6	11.6	15.6 ± 3.3	17.1
FeO	0.27 ± 0.23	0.29	0.21 ± 0.23	0.23	1.08 ± 1.61	1.09	0.42 ± 0.48	0.43	0.31 ± 0.22	0.34
MnO	0.0*	0.0*	0.0*	0.0*	0.03*	0.03*	0.01*	0.01*	0.04*	0.04*
MgO	0.01*	0.01*	0.01*	0.01*	0.0*	0.0*	0.02 ± 0.04	0.02	0.02*	0.02*
BaO	0.02*	0.02*	0.02*	0.02*	0.0*	0.0*	0.01*	0.01*	0.03*	0.03*
CaO	0.38 ± 0.17	0.41	0.30 ± 0.20	0.32	0.39 ± 0.16	0.39	0.45 ± 0.26	0.46	0.56 ± 0.14	0.61
Na ₂ O	3.39 ± 1.47	3.63	2.70 ± 1.81	2.90	3.19 ± 0.74	3.22	3.66 ± 1.96	3.78	5.22 ± 1.08	5.72
K ₂ O	4.95 ± 2.67	5.31	3.87 ± 3.05	4.15	4.82 ± 0.88	4.86	4.62 ± 3.23	4.77	6.51 ± 1.60	7.13
Total wt. %	93.3	100.0	93.2	100.0	99.2	100.0	96.9	100.0	91.3	100.0
An**	3.1		3.1		3.3		3.6		3.2	
Ab**	49.4		49.9		48.5		53.7		53.2	
Or**	47.5		47.0		48.2		43.7		43.6	
Na/K	1.04		1.06		1.01		1.20		1.22	
Alphatic index	0.976		0.981		0.969		0.984		1.00	
Notes:	2.5	2.4	1.5	1.4	1.3.5	1.3.4	1.3.5	1.3.4	1.5	1.4

Notes: *: Below detection limit, not included in analytical totals.

** : Calculated from molecular ratios of CaO, Na₂O, and K₂O for comparison with feldspar analyses.

1: Includes all analyses of randomly set points.

2: Excludes tridymite analyses (more than 90 wt % SiO₂)

3: Vapor-phase-altered material within devitrified matrix (not lithophysal).

4: Analyses normalized to total of 100 wt. %.

5: Variation (±) shown is 1 standard deviation for number of analyses averaged.

6: Includes very fine-grained clay (?) disseminated in matrix.

Table A-8: Defocused Beam Electron Microprobe Analyses (in wt. percent) of Vapor-Phase-Altered Matrix

Page 2 of 2

Analysis	6		7		8		9		10	
Sample	8E-1		8F-1		G1-448.9A		G1-448.9A		G1-504.6	
No. of points averaged	24		8		21		11		13	
Oxide										
SiO ₂	63.0 ± 12.2	77.5	65.3 ± 6.8	72.6	71.2 ± 15.1	78.3	56.1 ± 4.5	70.1	65.7 ± 11.0	72.1
Al ₂ O ₃	10.2 ± 3.3	12.5	13.6 ± 1.8	15.1	11.9 ± 6.0	13.1	15.4 ± 1.7	19.2	15.1 ± 3.8	16.5
FeO	0.14 ± 0.11	0.17	0.21 ± 0.18	0.23	0.38 ± 0.37	0.41	0.25 ± 0.05	0.31	0.38 ± 0.49	0.42
MnO	0.01*	0.01*	0.02*	0.02*	0.03 ± 0.03	0.04	0.0*	0.0*	0.01*	0.01*
MgO	0.01*	0.01*	0.02 ± 0.01	0.02	0.40 ± 0.96	0.44	1.50 ± 1.55	1.87	0.0*	0.0*
BaO	0.01*	0.01*	0.06*	0.06*	0.02*	0.02*	0.01*	0.01*	0.01*	0.01*
CaO	0.36 ± 0.13	0.44	0.38 ± 0.06	0.42	0.48 ± 0.39	0.52	0.94 ± 0.49	1.17	0.37 ± 0.11	0.40
Na ₂ O	3.39 ± 1.09	4.17	4.17 ± 0.40	4.64	2.87 ± 1.66	3.16	2.42 ± 1.44	3.02	4.43 ± 1.27	4.87
K ₂ O	4.20 ± 1.57	5.17	6.26 ± 1.00	6.96	3.64 ± 2.18	4.01	3.41 ± 1.99	4.26	5.15 ± 1.47	5.65
Total wt. %	81.3	100.0	89.9	100.0	90.9	100.0	80.0	100.0	91.1	100.0
An**	3.1		2.5		4.8		10.0		2.5	
Ab**	53.4		49.1		51.9		46.7		55.2	
Or**	43.5		48.4		43.3		43.3		42.3	
Na/K	1.23		1.01		1.20		1.08		1.31	
Alphatic index	0.992		1.00		0.728		0.498		0.852	
Notes:	1.5	1.4	2.5	2.4	1.5.6	1.4.6	5.6	4.6	1.5	1.4

Notes: *: Below detection limit, not included in analytical totals.

**: Calculated from molecular ratios of CaO, Na₂O, and K₂O for comparison with feldspar analyses.

1: Includes all analyses of randomly set points.

2: Excludes tridymite analyses (more than 90 wt. % SiO₂)

3: Vapor-phase-altered material within devitrified matrix (not lithophysal).

4: Analyses normalized to total of 100 wt. %.

5: Variation (±) shown is 1 standard deviation for number of analyses averaged.

6: Includes very fine-grained clay (?) disseminated in matrix.

Table A-9: Defocused Beam Electron Microprobe Analyses (in wt. percent) of Devitrified Fiamme

<u>Analysis</u>	<u>1</u>	<u>2</u>	<u>3</u>	<u>4</u>	<u>5</u>
Sample	8E-1	8E-1	8F-1	G1-448.9B	G1-504.6
No. of analyses averaged	9	12	9	21	11
<u>Oxide</u>					
SiO ₂	70.8± 0.8	68.7± 0.8	71.4± 1.5	71.8± 3.6	69.1± 1.5
Al ₂ O ₃	14.5± 0.2	14.8± 0.2	14.1± 0.8	14.9± 1.2	15.5± 0.6
FeO	1.10±0.08	1.11±0.32	0.87±0.23	1.04±0.59	1.13±0.23
MnO	0.02*	0.05±0.02	0.04*	0.07±0.04	0.07±0.02
MgO	0.12±0.09	0.15±0.08	0.12±0.07	0.28±0.72	0.09±0.05
BaO	0.02*	0.04*	0.0*	0.04±0.03	0.03*
CaO	0.46±0.04	0.54±0.06	0.47±0.10	0.45±0.10	0.66±0.38
Na ₂ O	4.45±0.16	4.61±0.25	4.23±0.47	4.17±0.51	4.70±0.62
K ₂ O	6.44±0.26	6.59±0.42	6.64±0.65	4.18±0.52	5.47±1.00
Total wt. %	97.9	96.6	97.9	96.9	96.7
An**	2.8	3.2	2.9	3.5	4.2
Ab**	49.8	49.9	47.7	58.2	54.2
Or**	47.4	46.9	49.3	38.3	41.6
Na/K	1.05	1.06	0.968	1.52	1.31
Agpaitic index	0.985	0.994	1.00	0.764	0.881

Notes: * : Below detection limit, not included in analytical totals.

** : Calculated from molecular ratios of CaO, Na₂O, and K₂O for comparison with other matrix types and feldspar phenocrysts.

All Analyses : In spherulitically devitrified areas of fiamme.

Variation (±) shown is one standard deviation for number of analyses averaged.

APPENDIX B.

POINT COUNTING

Analysis of Accuracy

An attempt has been made to determine the precision and accuracy of the point counting technique used on the test samples of lithophysal Topopah Spring Member. The ease of identification of the three components suggests that the precision of the procedure is very high. Determination of the accuracy is somewhat problematic. Discussions of error estimation associated with point counting available in the literature are in large part from studies of thin sections rather than large cored specimens. Most of the differences in error estimating formulae are associated with differing relationships between grain (or component) size and grid spacing. The simplest formulae, which use standard deviation as an error estimate (see Van der Plas and Tobi, 1965; Galehouse, 1971), require that all points counted be independent, which implies that the grid spacing be greater than the component size. Failure to meet this requirement results in the need to use more complicated error formulae (see Solomon and Brooks, 1966; Kelley, 1971; Neilson and Brockman, 1977).

The lithophysal samples have a component size which is much bigger than the grid spacing, thus invalidating the use of a simple standard deviation as an error estimate. The error estimating method for which the data on the lithophysal samples are both sufficient and relatively well suited is that given by Kelley (1971) for random samples from a multinomial distribution. The formula for the error estimate of the j^{th} component, S_j , may be written as :

$$S_j = [\chi_{(K-1, \alpha)}^2]^{1/2} \left[\frac{\lambda_j^2}{N} \right]^{1/2}, \quad (B1)$$

where $\chi^2_{(K-1)}$ is the upper-tail of the χ^2 distribution with $(K-1)$ degrees of freedom, K is the number of components, $(1-\alpha)$ is the degree of confidence associated with the volume percentage of the j^{th} component P_j , and N is the total number of counts made. The statistical measure $(\lambda_j)^2$ is defined by :

$$(\lambda_j)^2 = P_j(1 - P_j), \quad (B2)$$

where P_j is an estimate of P_j and is defined as :

$$P_j = \frac{n_j}{N}, \quad (B3)$$

where n_j is the number of points which fell on the j^{th} component.

For the lithophysal samples, the number of components, K , is three. Thus, for a 95 percent confidence in the value of P_j , the $\chi^2_{[(K-1),\alpha]}$ value is 5.991, and the resulting expression for the volume percentage of the j^{th} component is :

$$P_j = P_j \pm [5.991]^{\frac{1}{2}} \left[\frac{P_j(1 - P_j)}{N} \right]^{\frac{1}{2}}, \quad (B4)$$

(notice that the bracketed term is identical to the standard deviation which would be used if all points counted were independent).

APPENDIX C.

BULK PROPERTIES

Some of the bulk properties required by this study can be measured, while others are not directly measurable and thus need to be calculated. The remainder of this section describes the method of determination of each of the properties listed in Tables 4 and 5 of the text.

Saturation Procedure

All test samples were stored in a mixture of distilled water and water from well J-13 (NTS), from the completion of machining until mechanical testing began. While submerged, two of the samples (3A and 8F) were subjected to a series of three-step stages. Initially, an active vacuum of 600 Pa or less was drawn over the water surface in order to draw air out of the rock voids. Next, the submerged sample was left at ambient temperature and pressure. Finally, the sample was weighed several times (outside of the water). The vacuum and submerged times were at least 48 and 24 hours for the initial stage and 24 and 18 hours, respectively, for each succeeding stage. This was continued until the samples attained a constant weight (i.e., a weight change of less than 0.05 percent of the total weight). At the conclusion of these two saturation procedures, the second measurement showed no weight change within the resolution of the weighing device. Therefore, the eight remaining samples were subjected to only one saturation stage with vacuum and submerged times of at least 72 and 48 hours, respectively.

Measured Properties

Saturated Bulk Density of Samples $[(\rho_{sb})_T]$: The saturated weight and caliper volume of each sample were used to calculate a saturated bulk density. The weight measurements are not strictly accurate because the lithophysal voids intersecting the exterior of the samples were emptied of water before weighing, but subsequent calculations indicate

that the error was minor relative to other uncertainties. The error associated with this procedure is less than the precision of the weighings, which is approximately 450 to 900 g (1 to 2 lb), or about 1.5 %. The accuracy and precision of the measurements of machined sample volumes are very good (both approximately ± 0.3 %), so the main uncertainty in the saturated bulk density arises from inaccuracies in the weights. The values of the bulk density are expected to be accurate to ± 0.04 g/cm³, or about ± 1.9 %.

Grain Density of Samples $[(\rho_g)_T]$: The grain density of the test samples was measured on a randomly selected piece of scrap taken from the end of each sample during the machining process. In applying these grain densities to the large samples, the assumption is made that the material from the end is representative of the test sample as a whole. The grain densities are accurate to approximately ± 0.023 g/cm³ (Schwartz, 1983).

Porosity of Matrix Component $[\phi_M]$: The porosity of the matrix component was determined from measurements of bulk density on four small cores, two taken from scrap material at each end of a given test sample. The four cores per sample appeared to contain no significant quantity of altered material and no lithophysal voids. Each slug was 12.7 mm (0.5 in) in diameter and 6.40 to 12.7 mm (0.25 to 0.5 in) long. Procedures for sample saturation and measurement of dry and saturated bulk densities meet or exceed ASTM standards for such measurements.

Porosities of the matrix component were calculated by averaging the porosities of the four cores. The matrix porosity was calculated from saturated and dry bulk densities of the cores using the following formula :

$$\phi_M = \frac{(\rho_{sb})_M - (\rho_{db})_M}{\rho_{H_2O}}, \quad (C1)$$

where ϕ is the porosity, ρ_{db} is the dry bulk density, ρ_{sb} is the saturated bulk density and ρ_{H_2O} is the density of water, here assumed to be 1.0 g/cm³. The error in the porosities is estimated to be approximately ± 0.025 , based on expected errors in the bulk densities.

Grain Density of Matrix Component $[(\rho_g)_M]$: Grain densities were not measured on the cores. Matrix grain densities thus were assumed to be 2.55 g/cm³, the mean value of all grain densities measured as samples of nonlithophysal Topopah Spring Member. Experiments by Schwartz (1983) indicated a precision of ± 0.023 g/cm³ for grain density measurements.

Calculated Properties

Total Porosity of Samples [ϕ_T] : The total porosity of a test sample was calculated using the following equation :

$$\phi_T = \frac{(\rho_{sb})_T - (\rho_g)_T}{1 - (\rho_g)_T} \quad (C2)$$

Porosity of Vapor-Phase-Altered Material [ϕ_A] : The porosity of the altered material was calculated using the following equation :

$$\phi_A = \frac{\phi_T - P_L - P_M \phi_M}{P_A} \quad (C3)$$

where P_L is the volume fraction of lithophysal voids as determined by point counting, and P_M and P_A are the volume fractions of matrix and altered material, respectively, where by definition

$$P_L + P_M + P_A = 1. \quad (C4)$$

Grain Density of Vapor-Phase-Altered Material [$(\rho_g)_A$] : The grain density of the altered material, $(\rho_g)_A$, can be calculated using the following equation :

$$(\rho_g)_A = \frac{(\rho_g)_T [(1 - \phi_M)P_M + (1 - \phi_A)P_A] - (\rho_g)_M (1 - \phi_M)P_M}{(1 - \phi_A)P_A} \quad (C5)$$

APPENDIX D

This appendix presents calibration results and mechanical test results in two tables and twenty-five figures. Table D-1 lists calibration data for the individual measurement gages used in the mechanical experiments. Table D-2 lists and Figures D-1A to D-1E present the pre- and post-test system calibration results using 6061-T651 aluminum. The axial stress-axial strain and lateral strain-axial strain results from the mechanical experiments on the Topopah Spring Member lithophysal samples are plotted in Figures D-2A to D-2J and Figures D-3A to D-3J, respectively.

Table D-1. Load Cell, Axial LVDT and Lateral LVDT's Calibration Data

Load Cell			Axial LVDT		
f_a (kN)	f_m (kN)	e_m (%)	δ_a (mm)	δ_m (mm)	e_m (%)
445.00	448.78	.85	1.270	1.213	-4.5
890.00	892.45	.28	2.540	2.422	-4.7
1335.0	1336.3	.10	3.810	3.658	-4.0
1780.0	1780.2	.01	5.080	4.919	-3.2
2225.0	2223.4	-.07	6.350	6.100	-2.5
			7.620	7.473	-1.9
			8.890	8.769	-1.4
			10.16	10.06	-1.0
			11.43	11.42	-0.1
			12.70	12.70	0.0

Lateral LVDT 1			Lateral LVDT 2		
δ_a (mm)	δ_m (mm)	e_m (%)	δ_a (mm)	δ_m (mm)	e_m (%)
.6350	.6198	-2.4	.6350	.6045	-4.8
1.270	1.243	-2.1	1.270	1.224	-3.6
1.905	1.877	-1.5	1.905	1.847	-3.0
2.540	2.511	-1.1	2.540	2.468	-2.8
3.175	3.142	-1.0	3.175	3.096	-2.5
3.810	3.773	-1.0	3.810	3.730	-2.1
4.445	4.413	-0.7	4.445	4.375	-1.6
5.080	5.057	-0.5	5.080	5.029	-1.0
5.715	5.702	-0.2	5.715	5.685	-0.1
6.350	6.345	-0.1	6.350	6.346	-0.1

Notes:

f : Force
 δ : Displacement

a : Actual
m : Measured

e : Error

Table D-2. Aluminum Sample Calibration Data

Pre-Test Series			Post-Test Series			
σ_{ax} (MPa)	ϵ_{ax} (milli)	ϵ_{lat} (milli)	σ_{ax} (MPa)	ϵ_{ax} (milli)	ϵ_{lat1} (milli)	ϵ_{lat2} (milli)
0	0		0	0	0	0
2.660	.0406		2.647	.0442	-.0137	-.0087
4.015	.0600	-.0217	5.319	.0761	-.0314	-.0334
6.802	.0971		8.027	.1109	-.0340	-.0384
10.77	.1570		10.79	.1451	-.0532	-.0433
15.08	.2137		13.52	.1867	-.0576	-.0619
19.14	.2737		16.86	.2268	-.0735	-.0782
23.11	.3311		19.63	.2688	-.0826	-.0997
27.17	.3913		22.37	.3077	-.1052	-.1026
31.59	.4483		25.12	.3433	-.1183	-.1131
36.05	.5092		27.90	.3991	-.1296	-.1360
40.17	.5658		30.61	.4291	-.1352	-.1445
44.30	.6267		33.31	.4563	-.1526	-.1529
48.53	.6832		36.03	.4993	-.1584	-.1657
52.70	.7385	-.2490	38.75	.5359	-.1642	-.1729
53.00	.7433		43.78	.5736	-.1837	-.1785
57.46	.8011		44.73	.6180	-.2061	-.1947
60.36	.8427		47.40	.6633	-.2122	-.2090
			50.02	.6947	-.2232	-.2235
			52.56	.7337	-.2340	-.2346

Notes:

σ_{ax} : Axial stress

ϵ_{ax} : Axial strain

ϵ_{lat} : Lateral strain

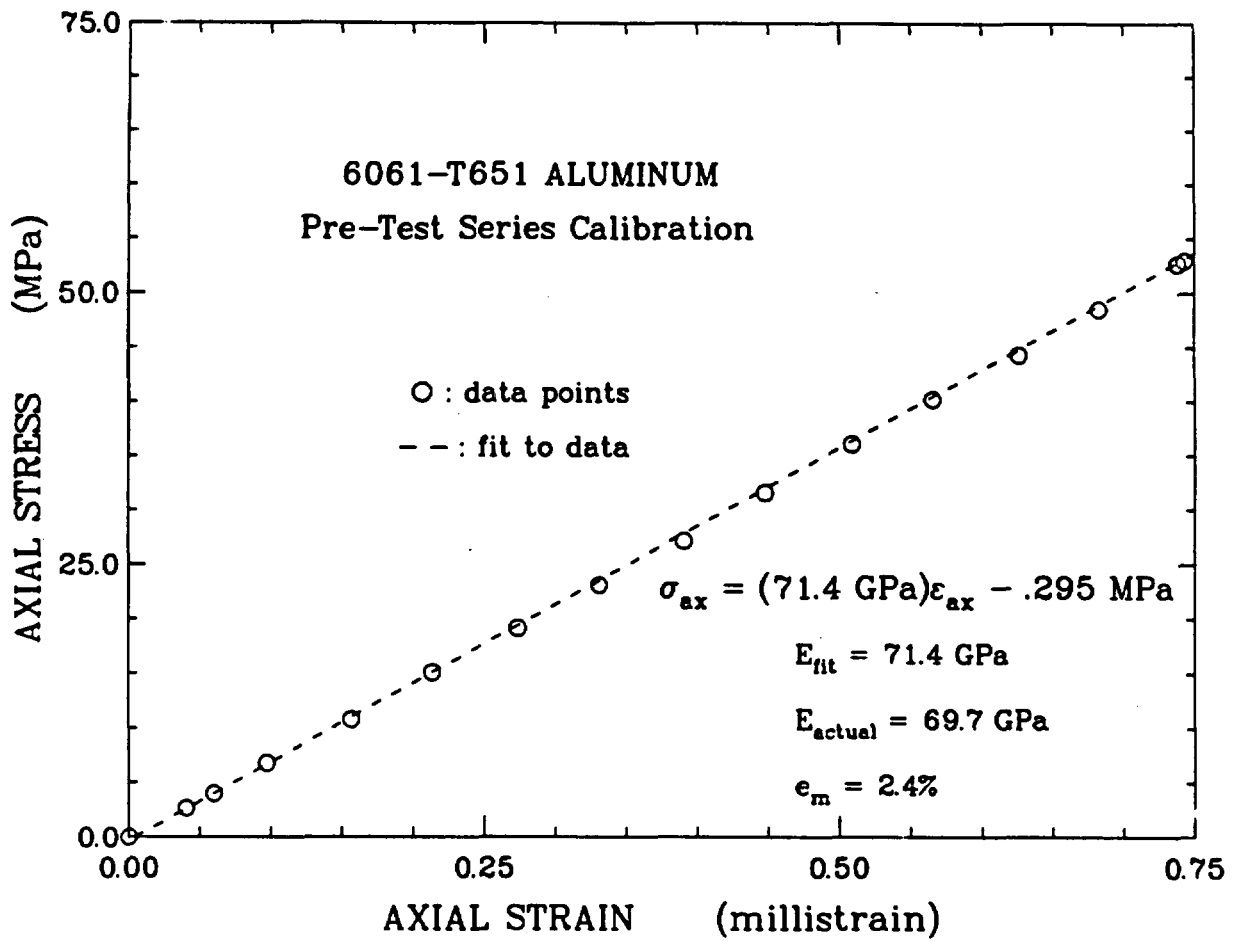


Figure D-1A.

Plot of axial stress-axial strain data with a linear, least-squares fit for pre-test series system calibration on a 6061-T651 aluminum sample.

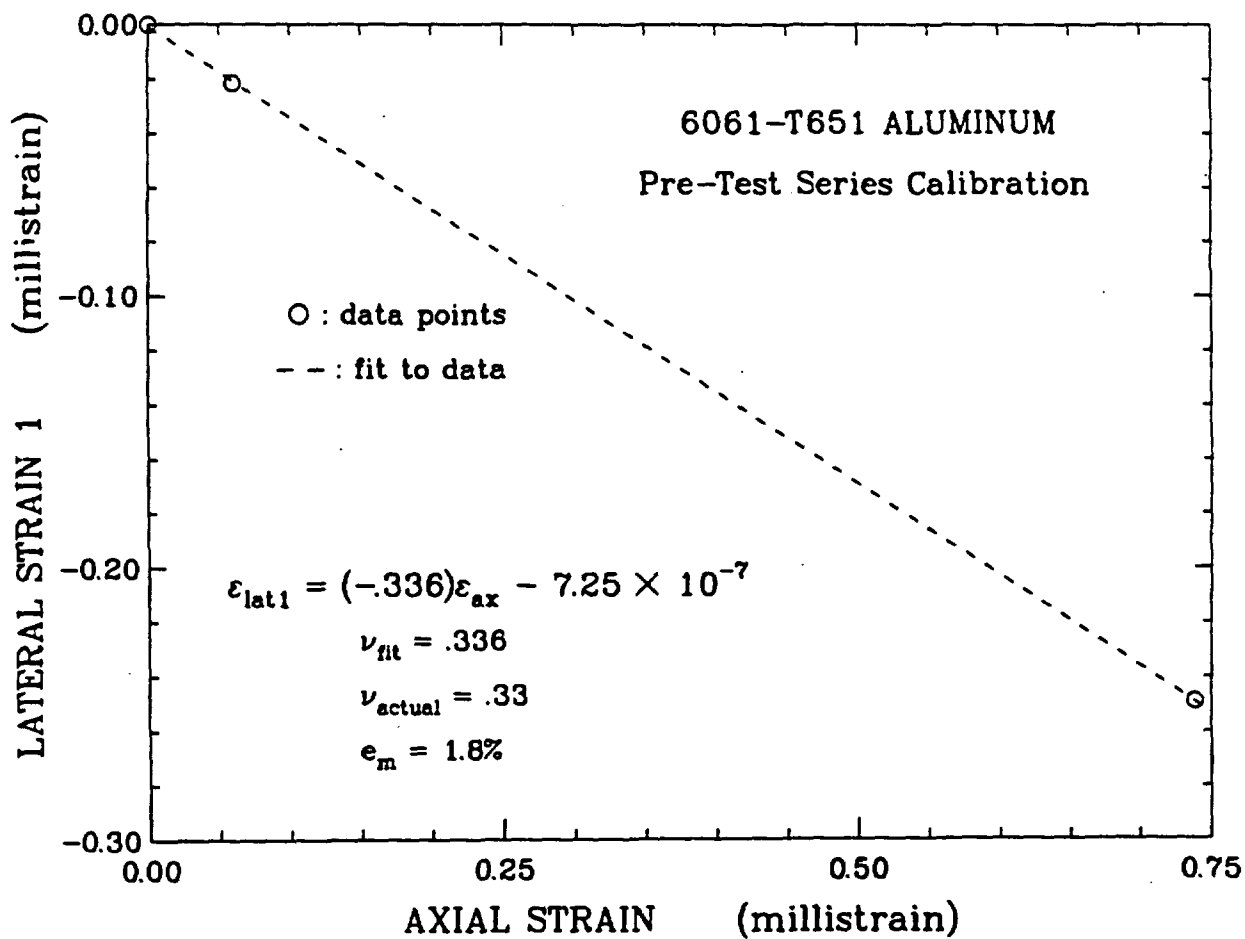


Figure D-1B.

Plot of axial strain-lateral strain data with a linear, least-squares fit for pre-test series system calibration on a 6061-T651 aluminum sample.

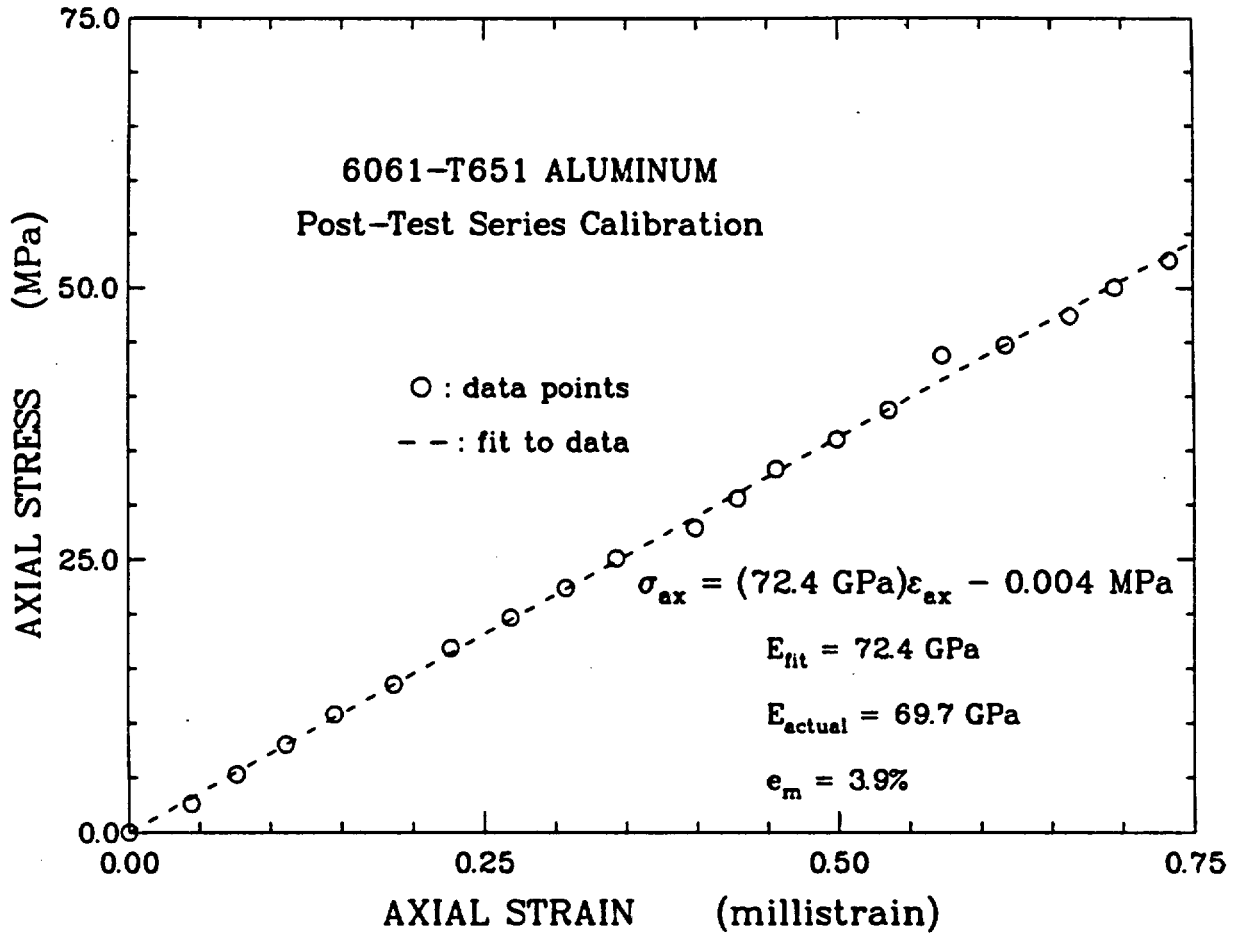


Figure D-1C.

Plot of axial stress-axial strain data with a linear, least-squares fit for post-test series system calibration on a 6061-T651 aluminum sample.

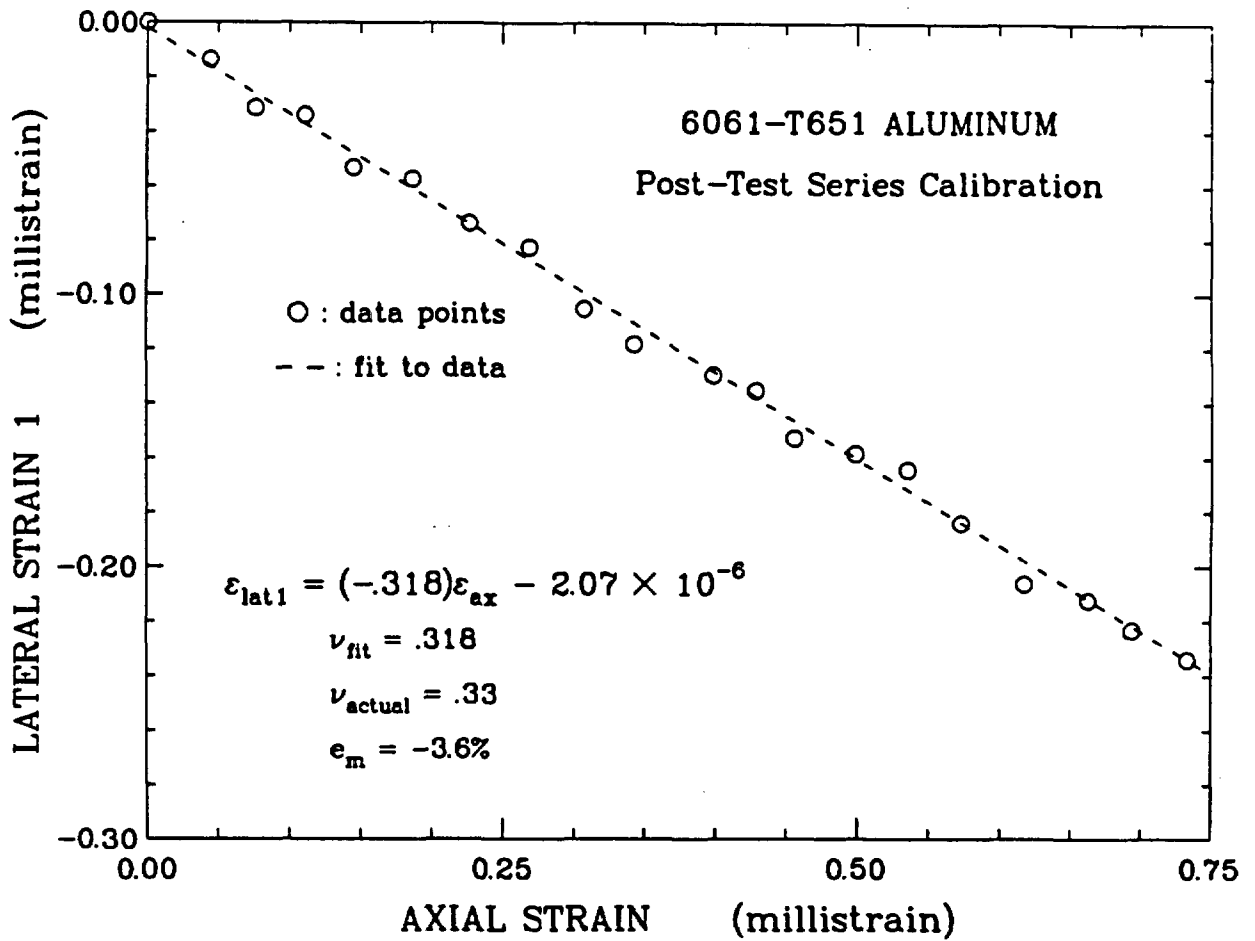


Figure D-1D.

Plot of axial strain-lateral strain 1 data with a linear, least-squares fit for post-test series system calibration on a 6061-T651 aluminum sample.

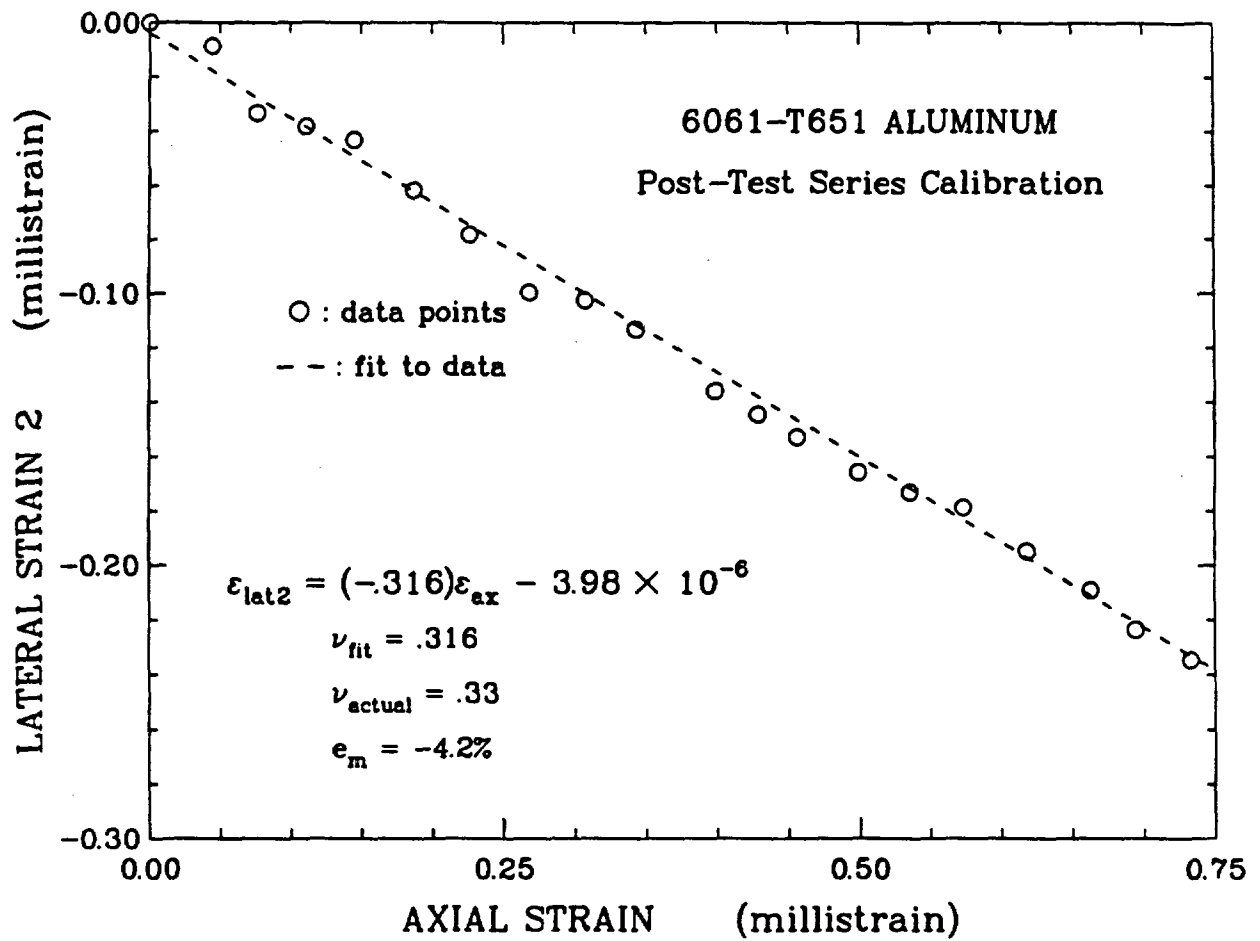


Figure D-1E.

Plot of axial strain-lateral strain 2 data with a linear, least-squares fit for post-test series system calibration on a 6061-T651 aluminum sample.

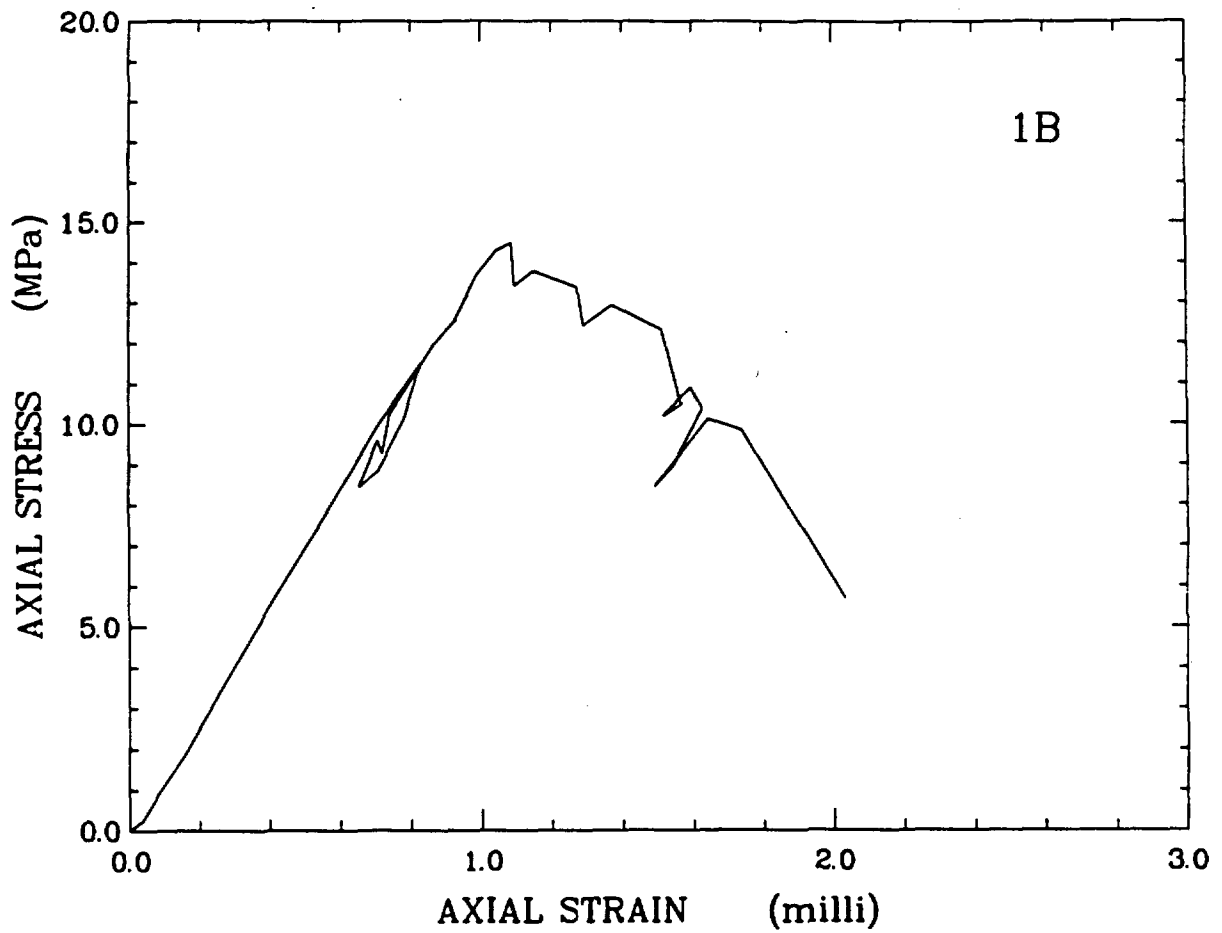


Figure D-2A.

Axial stress-axial strain curve for saturated sample 1B deformed in compression at atmospheric confining pressure, room temperature and a nominal strain rate of 10^{-5} s^{-1} .

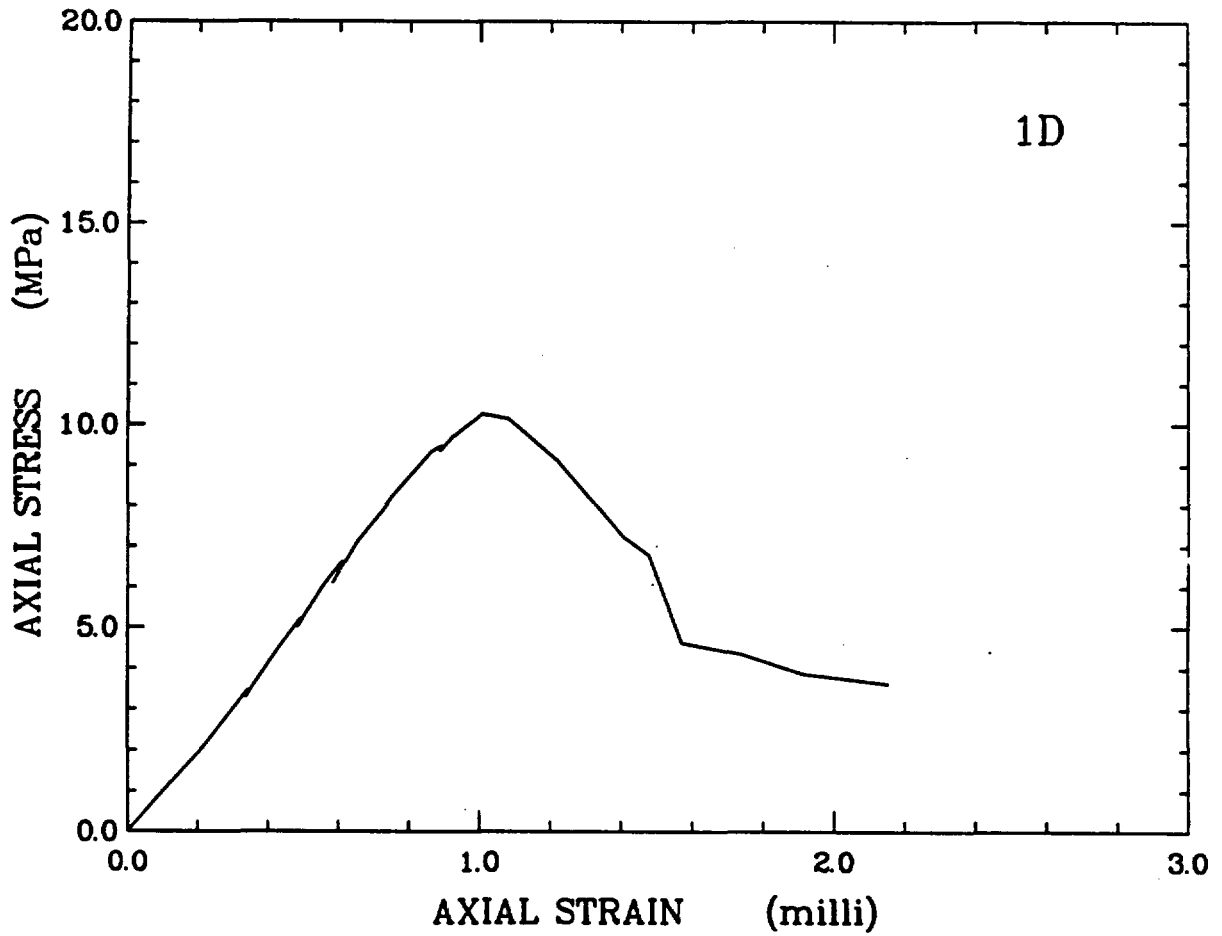


Figure D-2B.

Axial stress-axial strain curve for saturated sample 1D deformed in compression at atmospheric confining pressure, room temperature and a nominal strain rate of 10^{-5} s^{-1} .

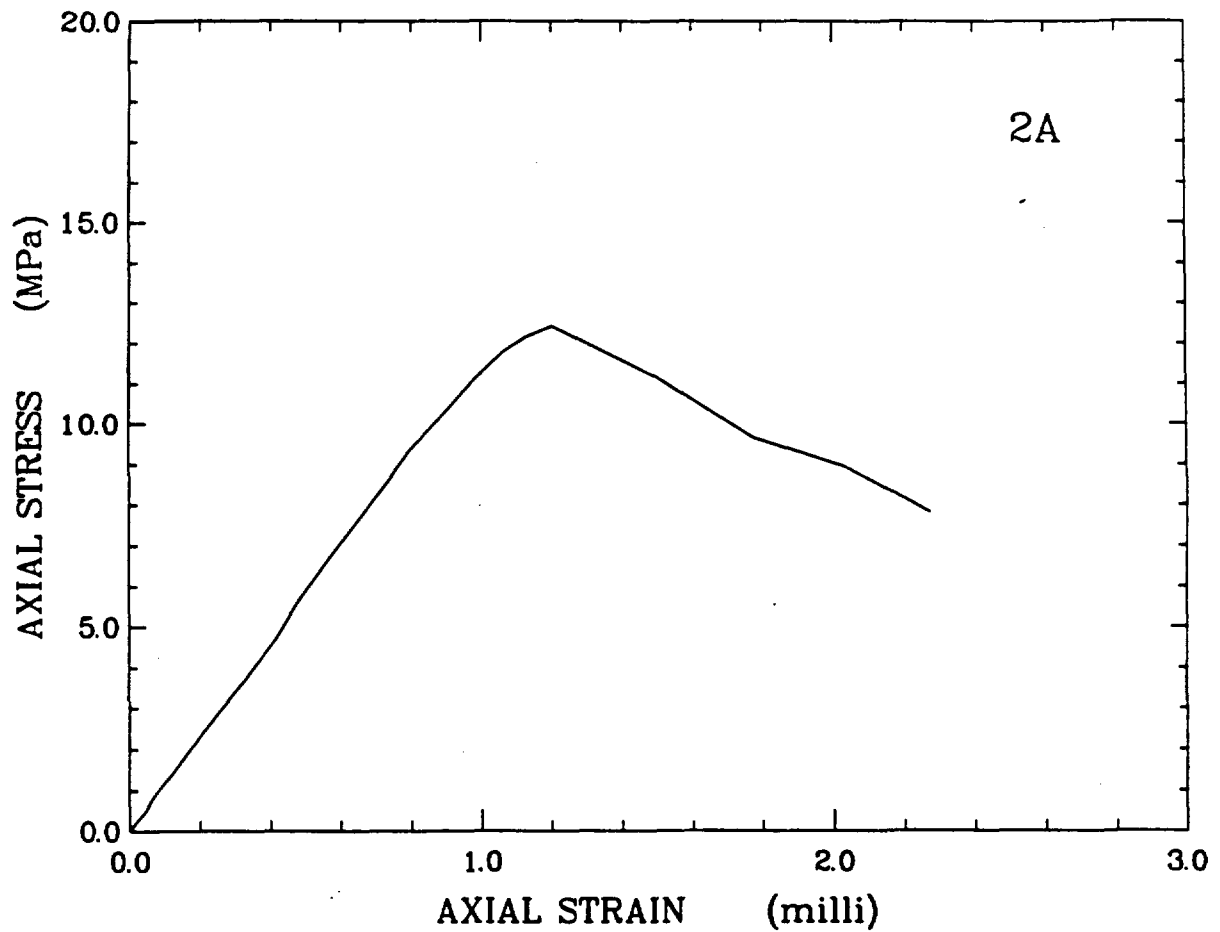


Figure D-2C.

Axial stress-axial strain curve for saturated sample 2A deformed in compression at atmospheric confining pressure, room temperature and a nominal strain rate of 10^{-6} s^{-1} .

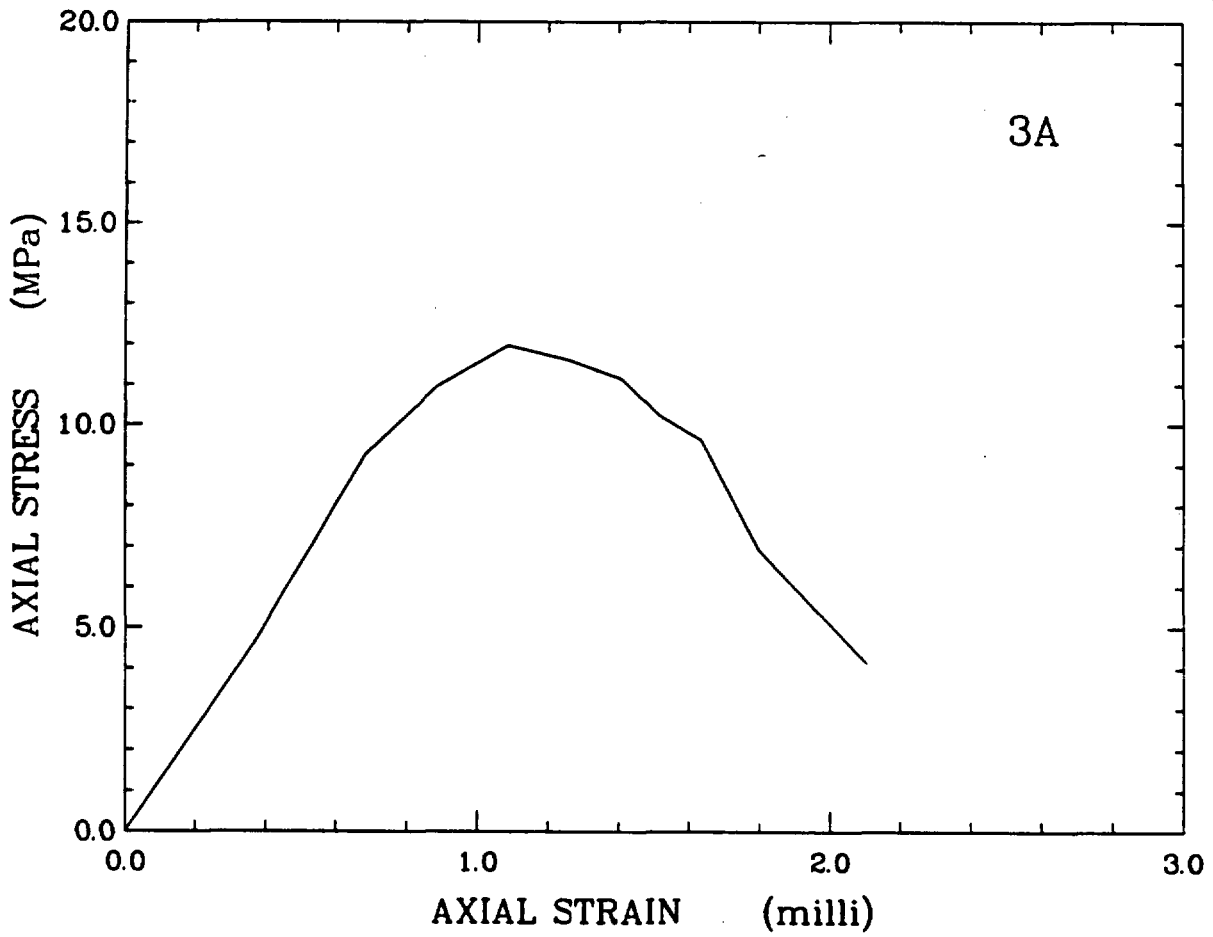


Figure D-2D.

Axial stress-axial strain curve for saturated sample 3A deformed in compression at atmospheric confining pressure, room temperature and a nominal strain rate of 10^{-5} s^{-1} .

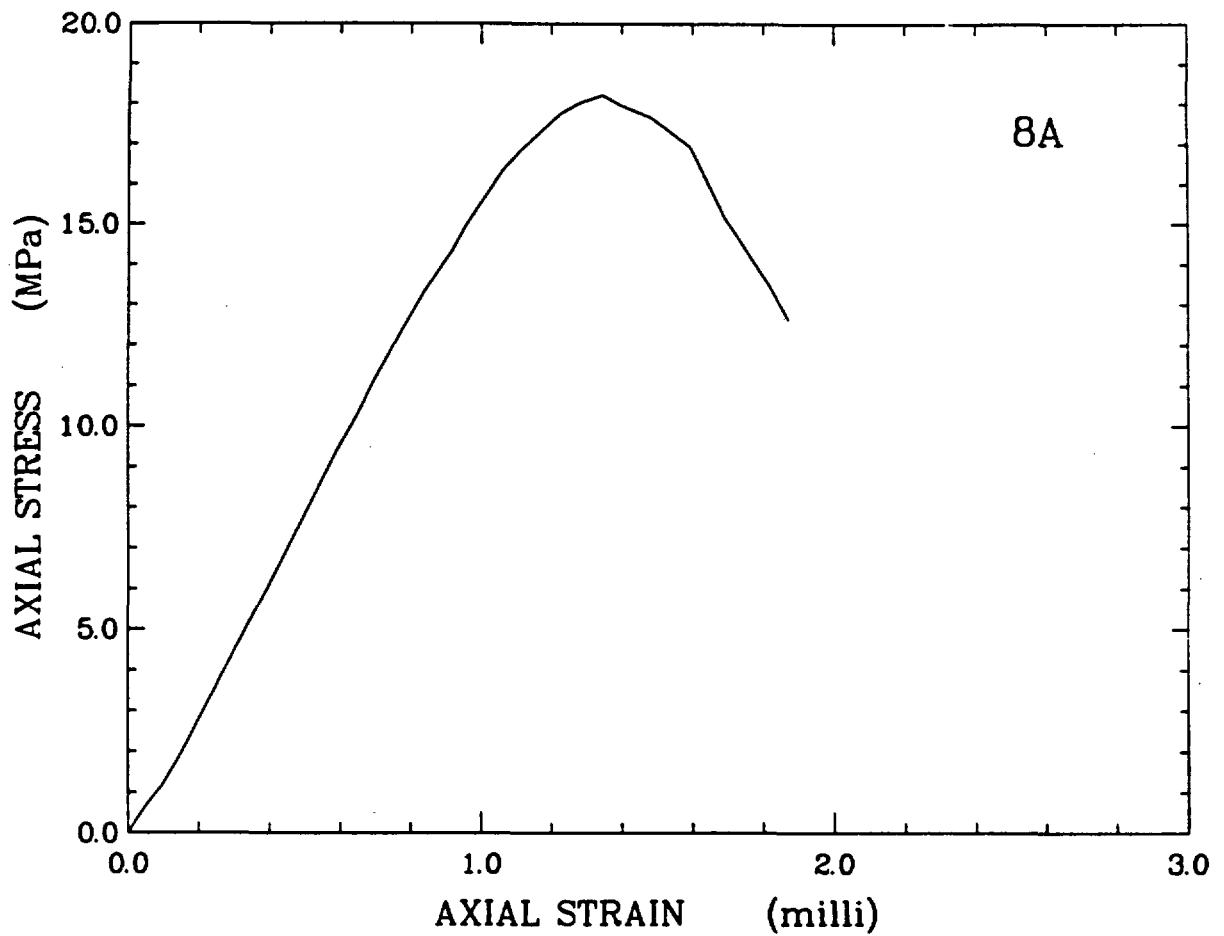


Figure D-2E.

Axial stress-axial strain curve for saturated sample 8A deformed in compression at atmospheric confining pressure, room temperature and a nominal strain rate of 10^{-5} s^{-1} .

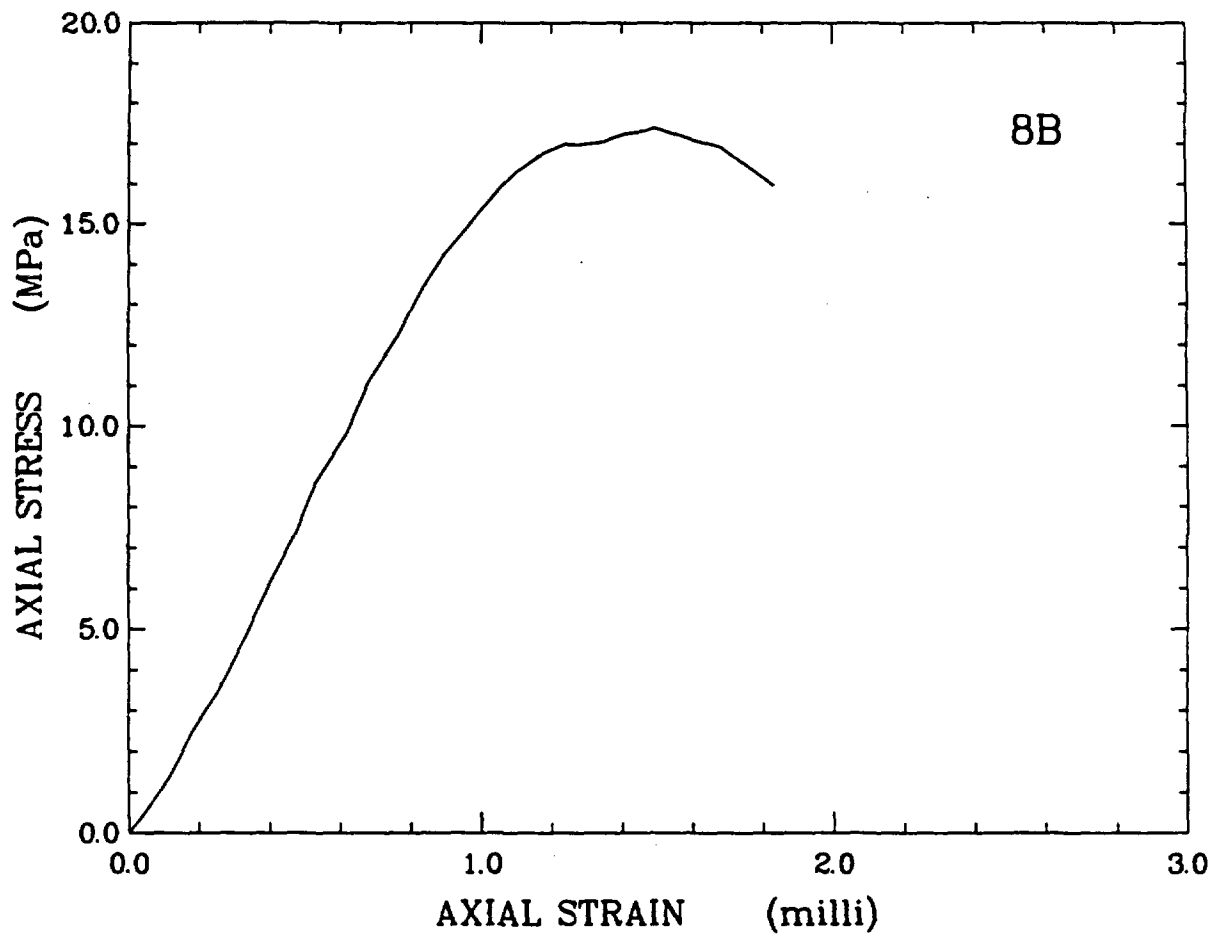


Figure D-2F.

Axial stress-axial strain curve for saturated sample 8B deformed in compression at atmospheric confining pressure, room temperature and a nominal strain rate of 10^{-5} s^{-1} .

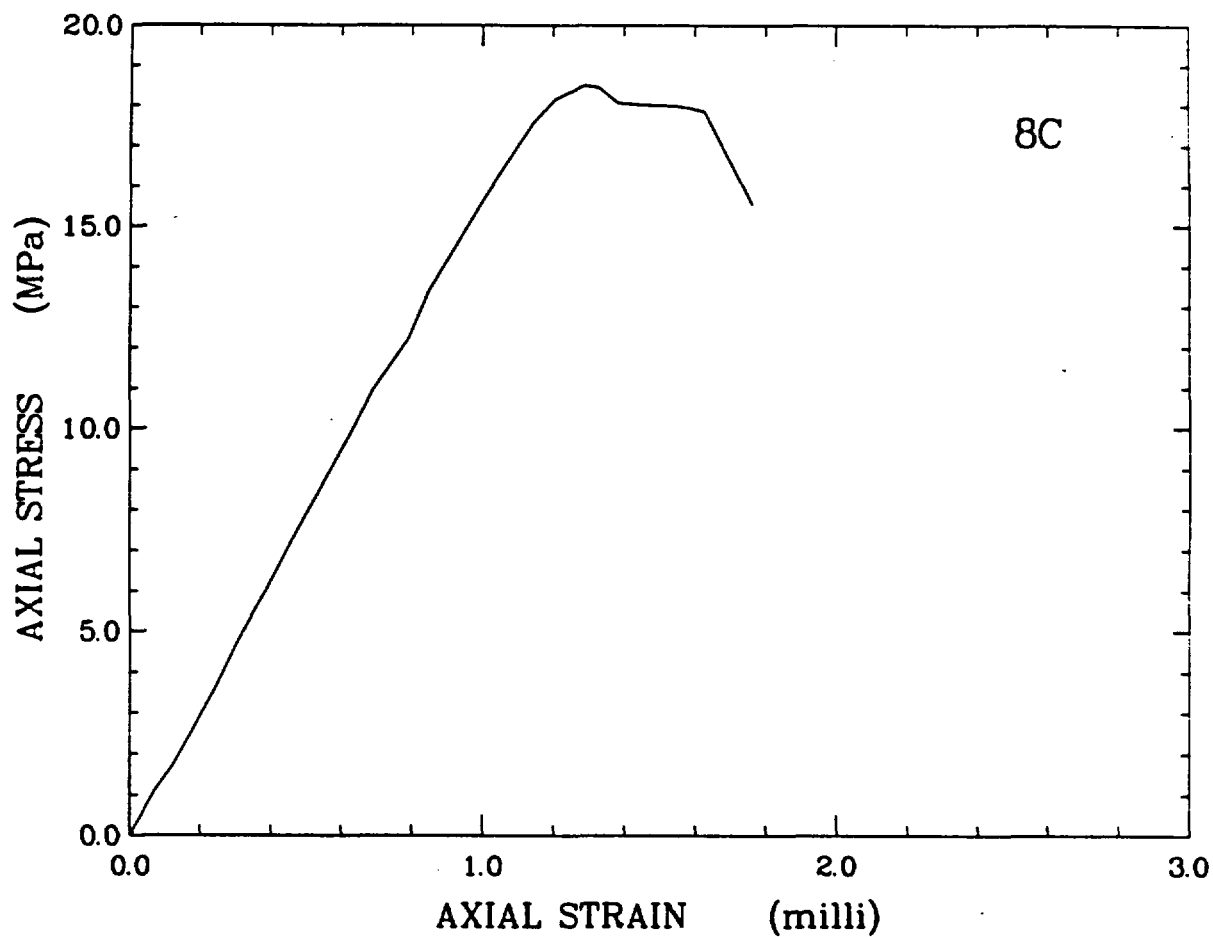


Figure D-2G.

Axial stress-axial strain curve for saturated sample 8C deformed in compression at atmospheric confining pressure, room temperature and a nominal strain rate of 10^{-5} s^{-1} .

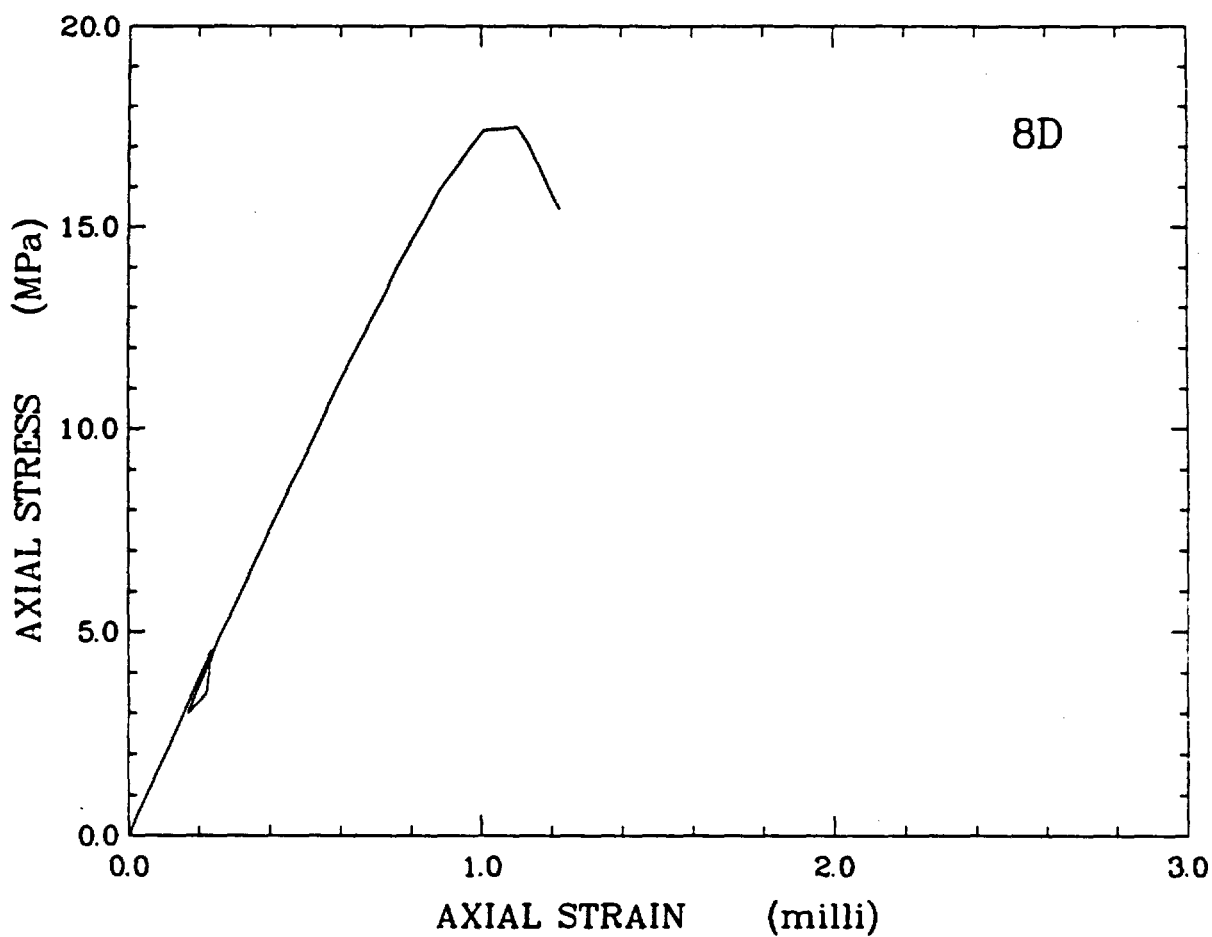


Figure D-2H.

Axial stress-axial strain curve for saturated sample 8D deformed in compression at atmospheric confining pressure, room temperature and a nominal strain rate of 10^{-5} s^{-1} .

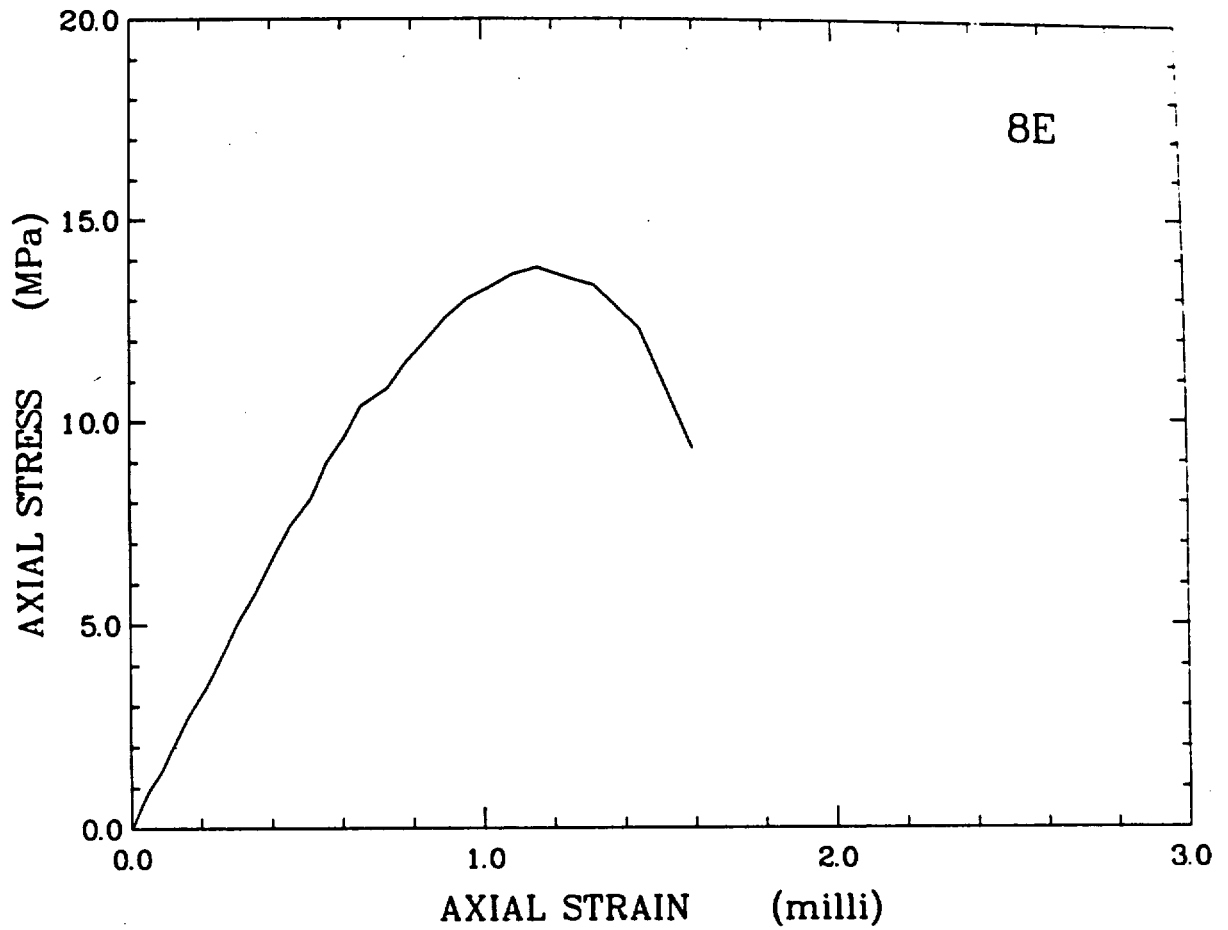


Figure D-2I.

Axial stress-axial strain curve for saturated sample 8E deformed in compression at atmospheric confining pressure, room temperature and a nominal strain rate of 10^{-6} s^{-1} .

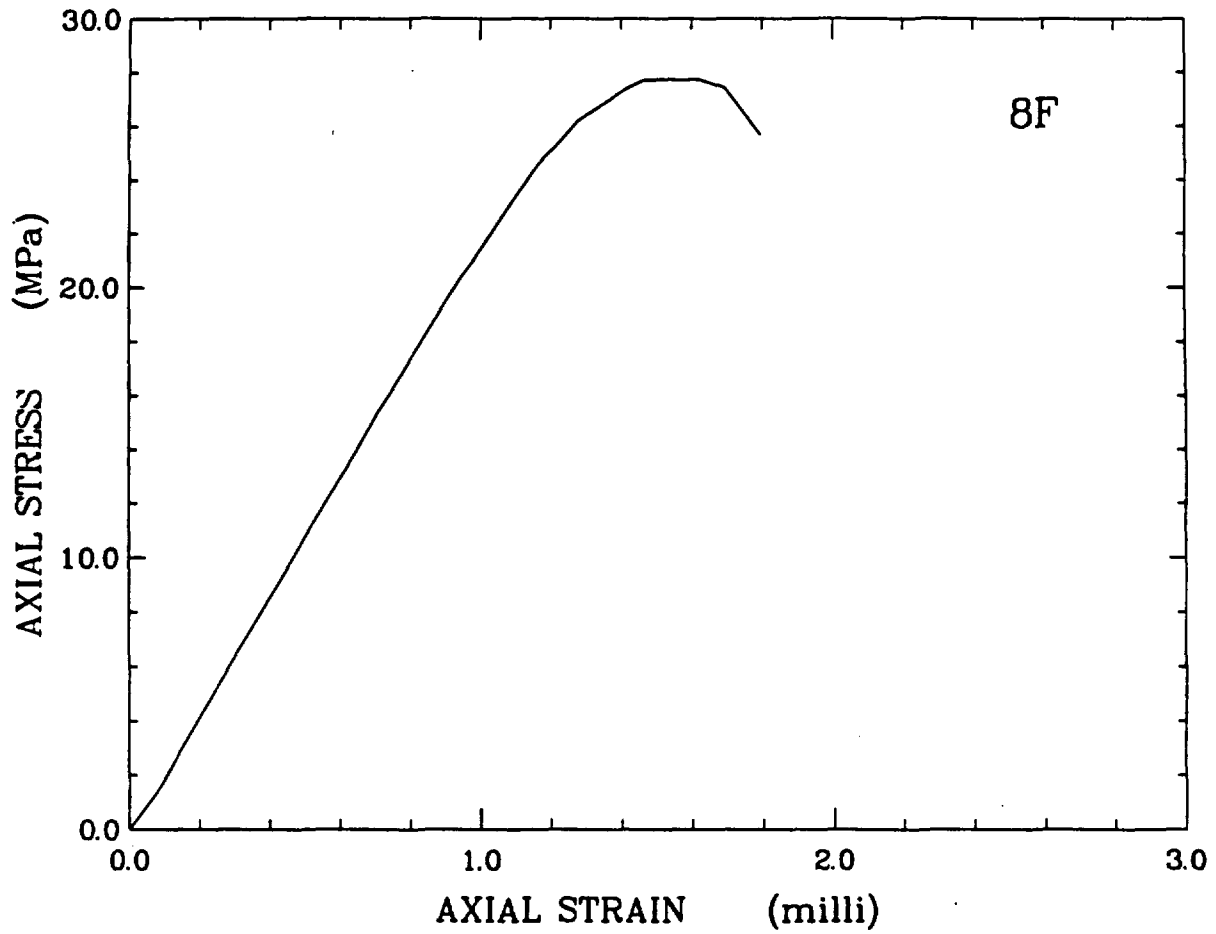


Figure D-2J.

Axial stress-axial strain curve for saturated sample 8F deformed in compression at atmospheric confining pressure, room temperature and a nominal strain rate of 10^{-5} s^{-1} .

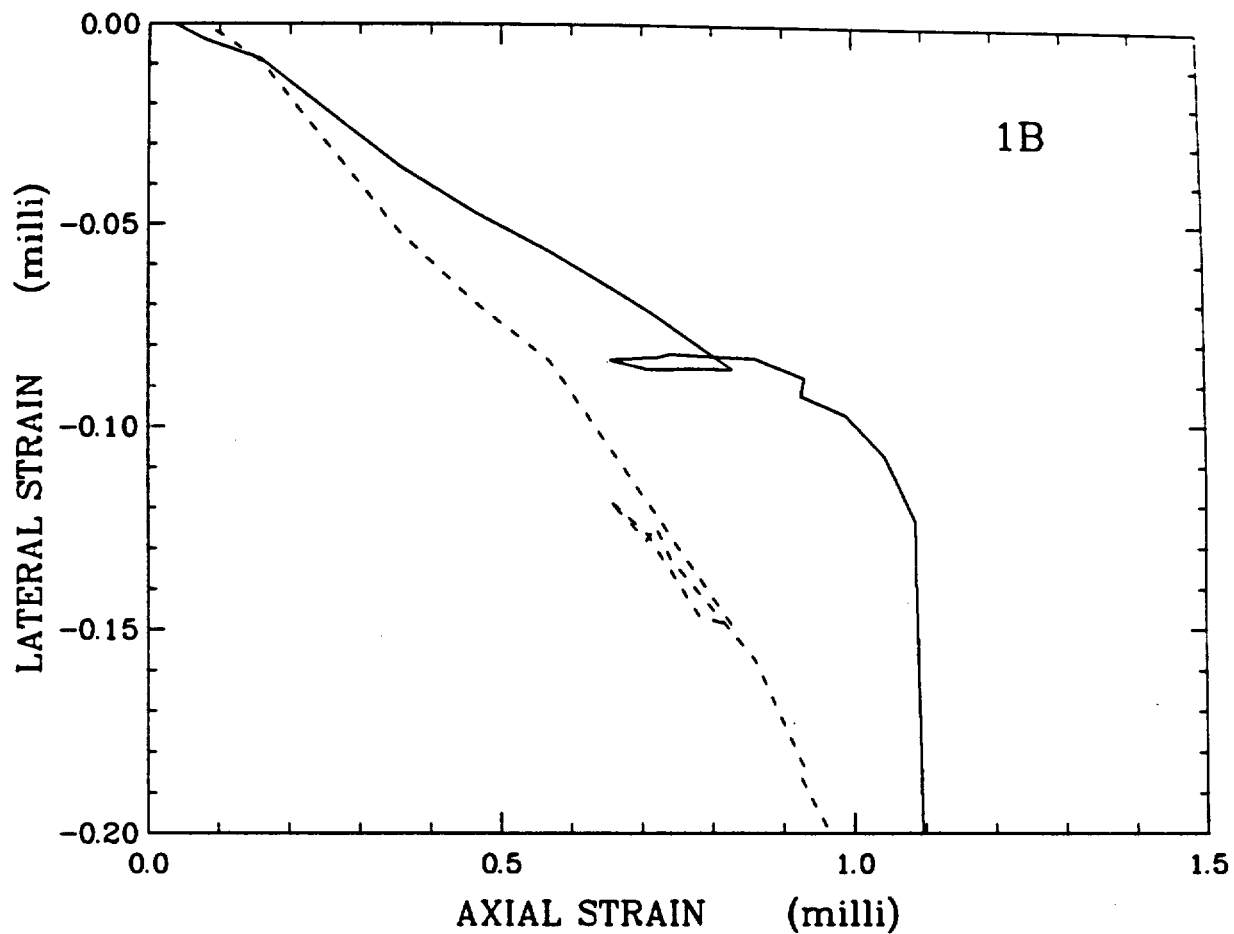


Figure D-3A.

Lateral strain-axial strain curve for saturated sample 1B deformed in compression at atmospheric confining pressure, room temperature and a nominal strain rate of 10^{-5} s^{-1} .

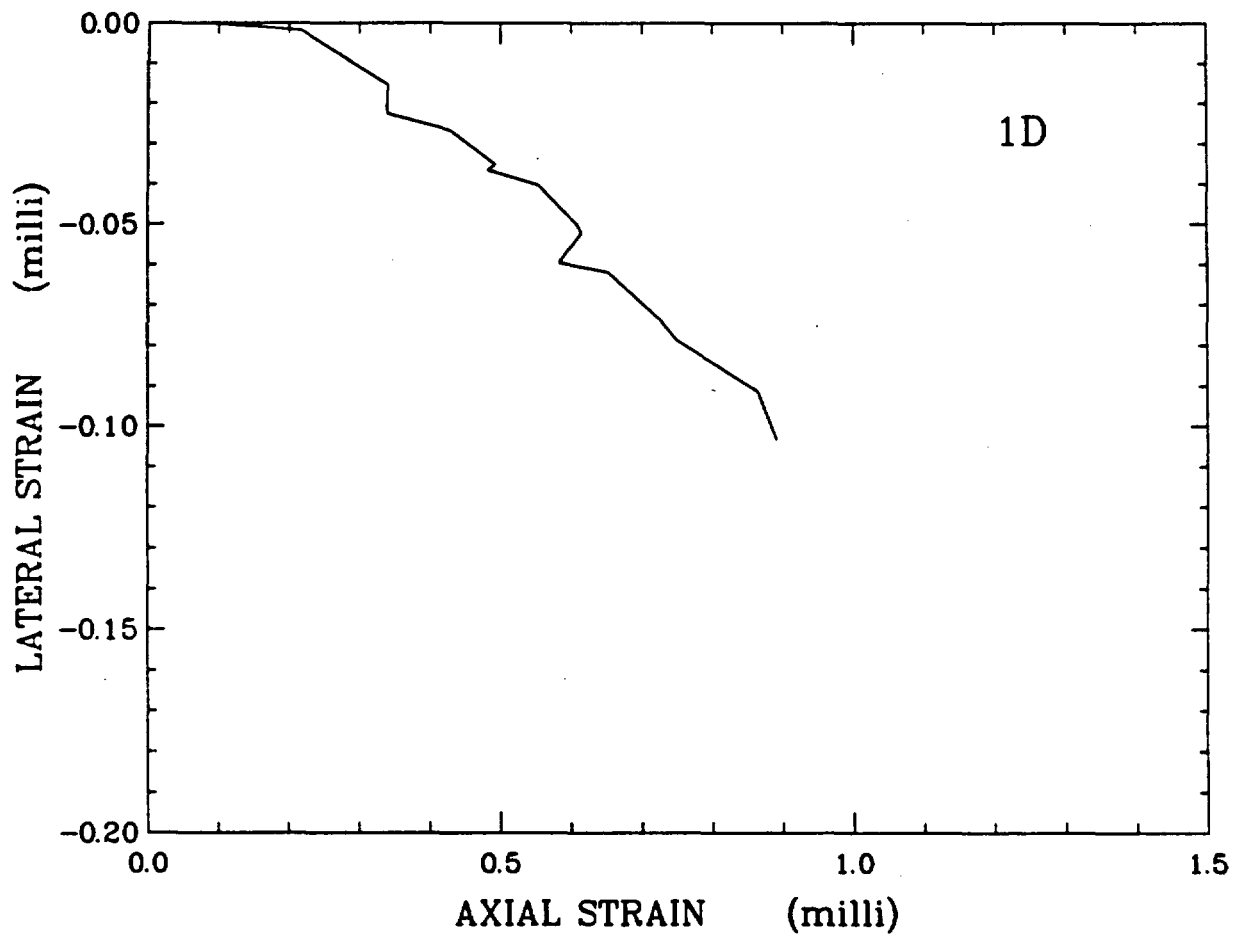


Figure D-3B.

Lateral strain-axial strain curve for saturated sample 1D deformed in compression at atmospheric confining pressure, room temperature and a nominal strain rate of 10^{-6} s^{-1} .

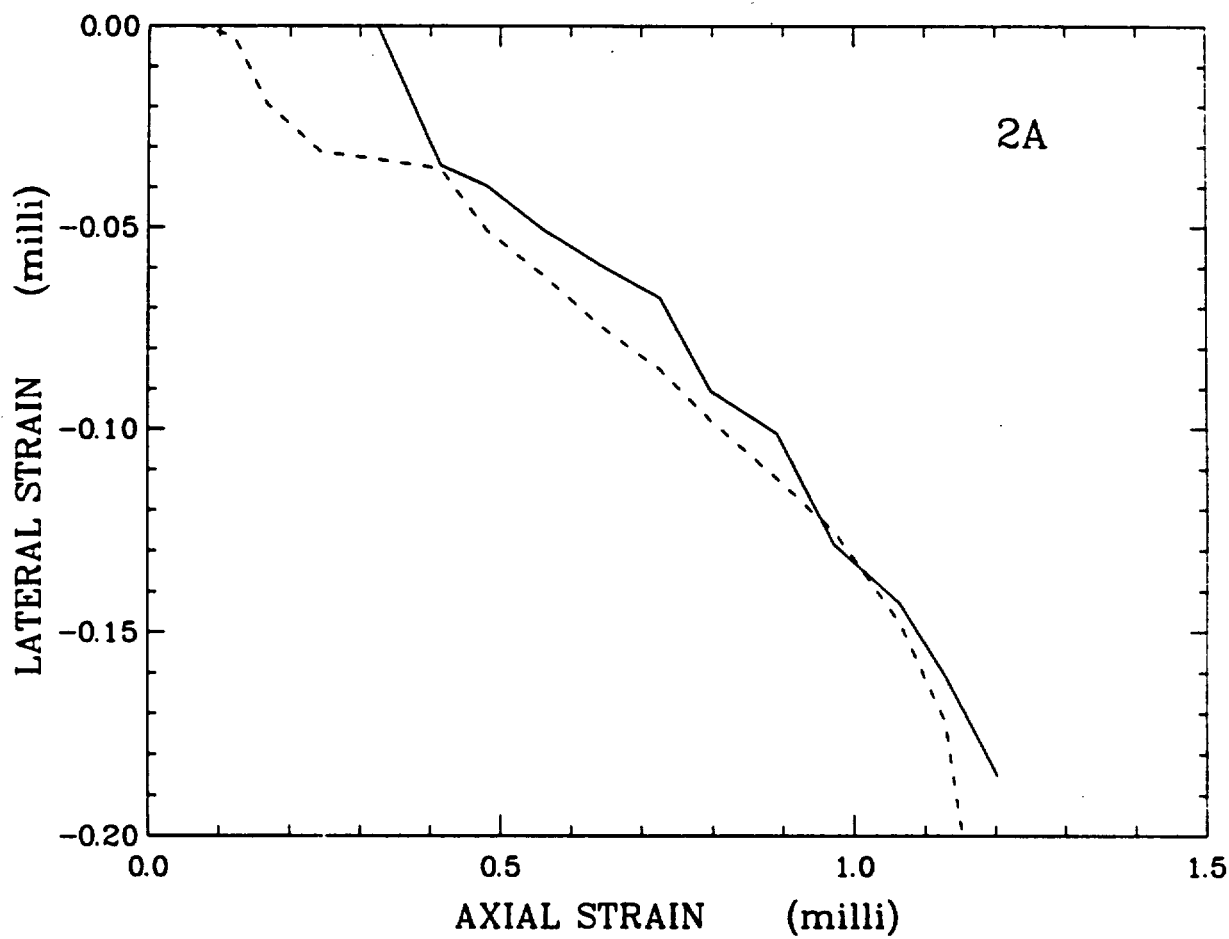


Figure D-3C.

Lateral strain-axial strain curve for saturated sample 2A deformed in compression at atmospheric confining pressure, room temperature and a nominal strain rate of 10^{-5} s^{-1} .

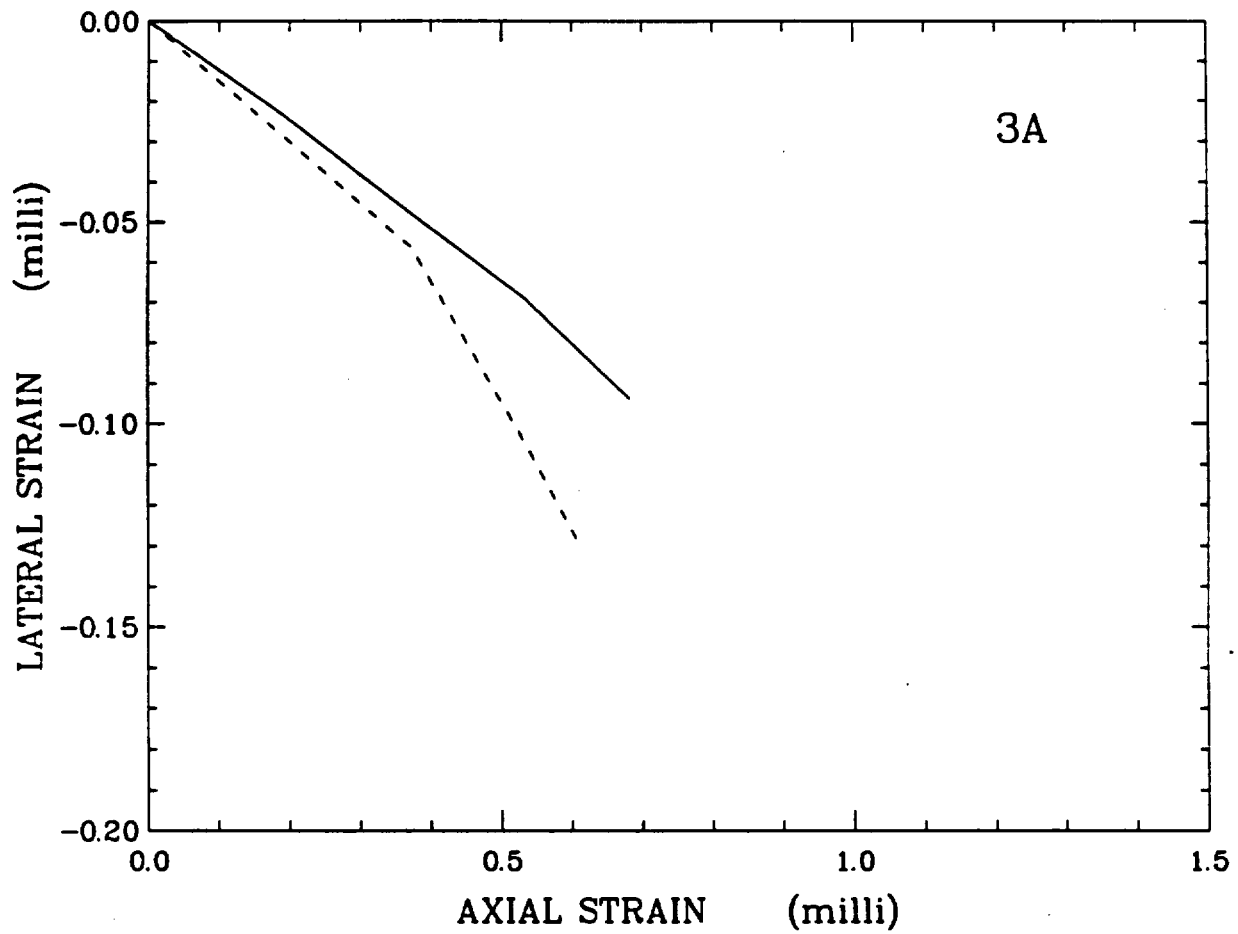


Figure D-3D.

Lateral strain-axial strain curve for saturated sample 3A deformed in compression at atmospheric confining pressure, room temperature and a nominal strain rate of 10^{-5} s^{-1} .

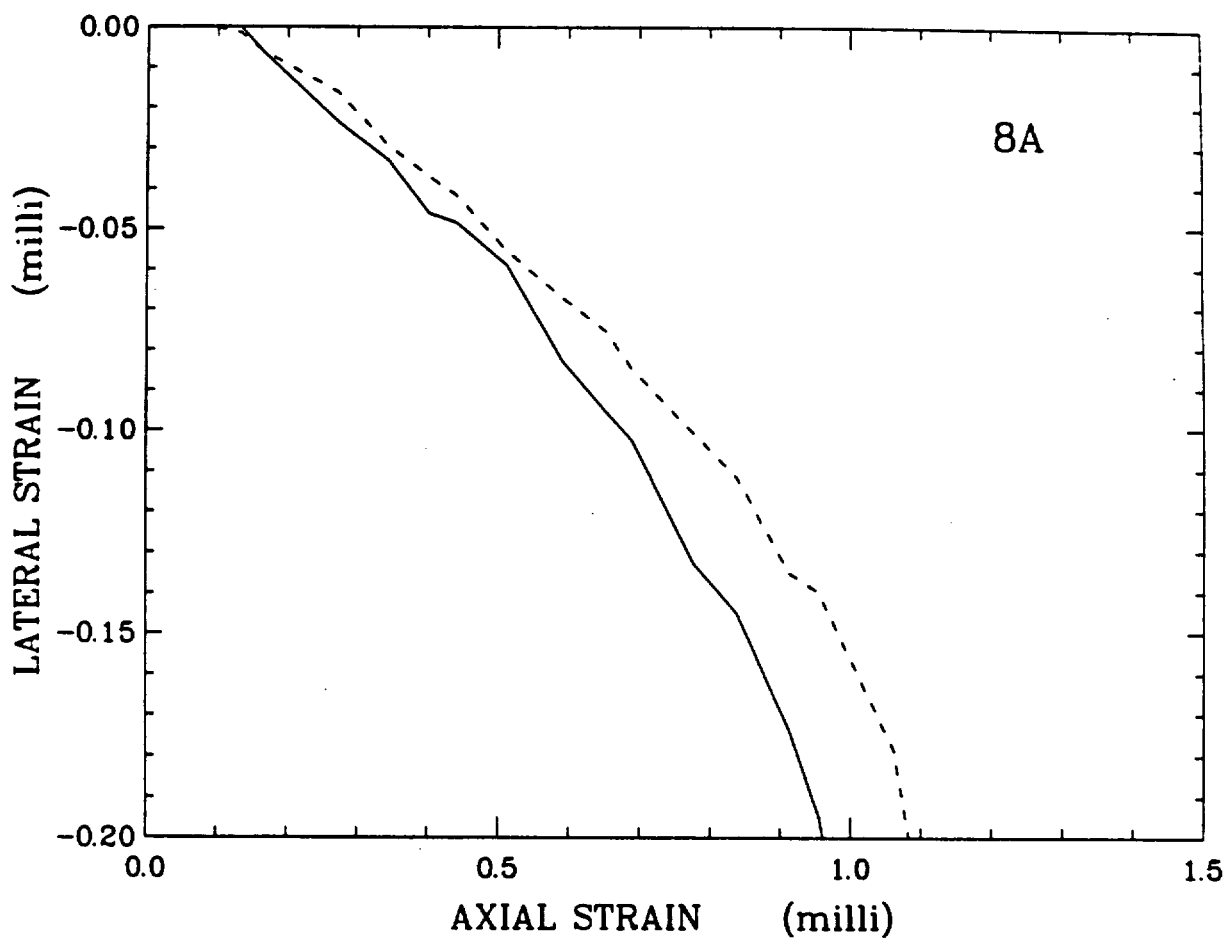


Figure D-3E.

Lateral strain-axial strain curve for saturated sample 8A deformed in compression at atmospheric confining pressure, room temperature and a nominal strain rate of 10^{-6} s^{-1} .

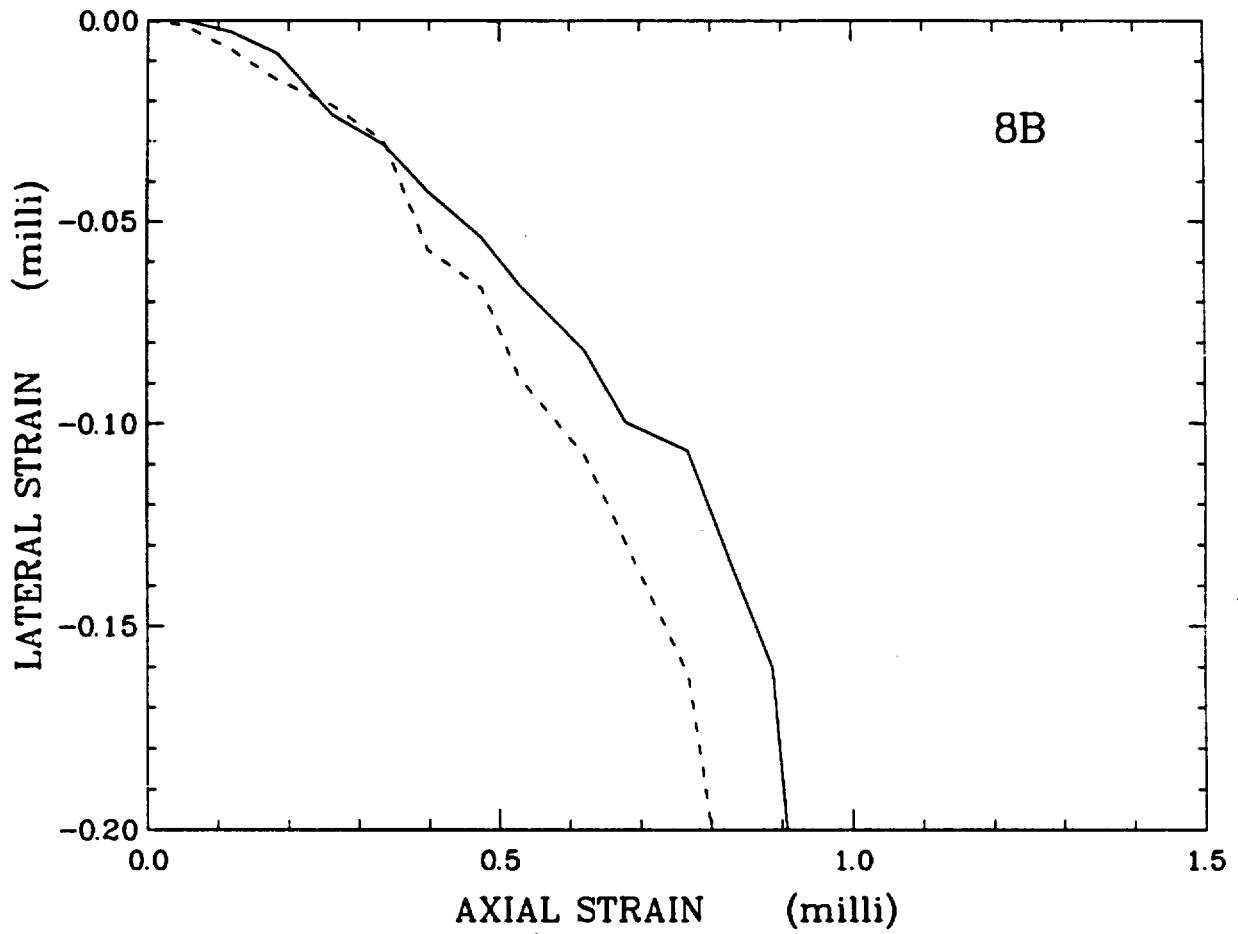


Figure D-3F.

Lateral strain-axial strain curve for saturated sample 8B deformed in compression at atmospheric confining pressure, room temperature and a nominal strain rate of 10^{-6} s^{-1} .

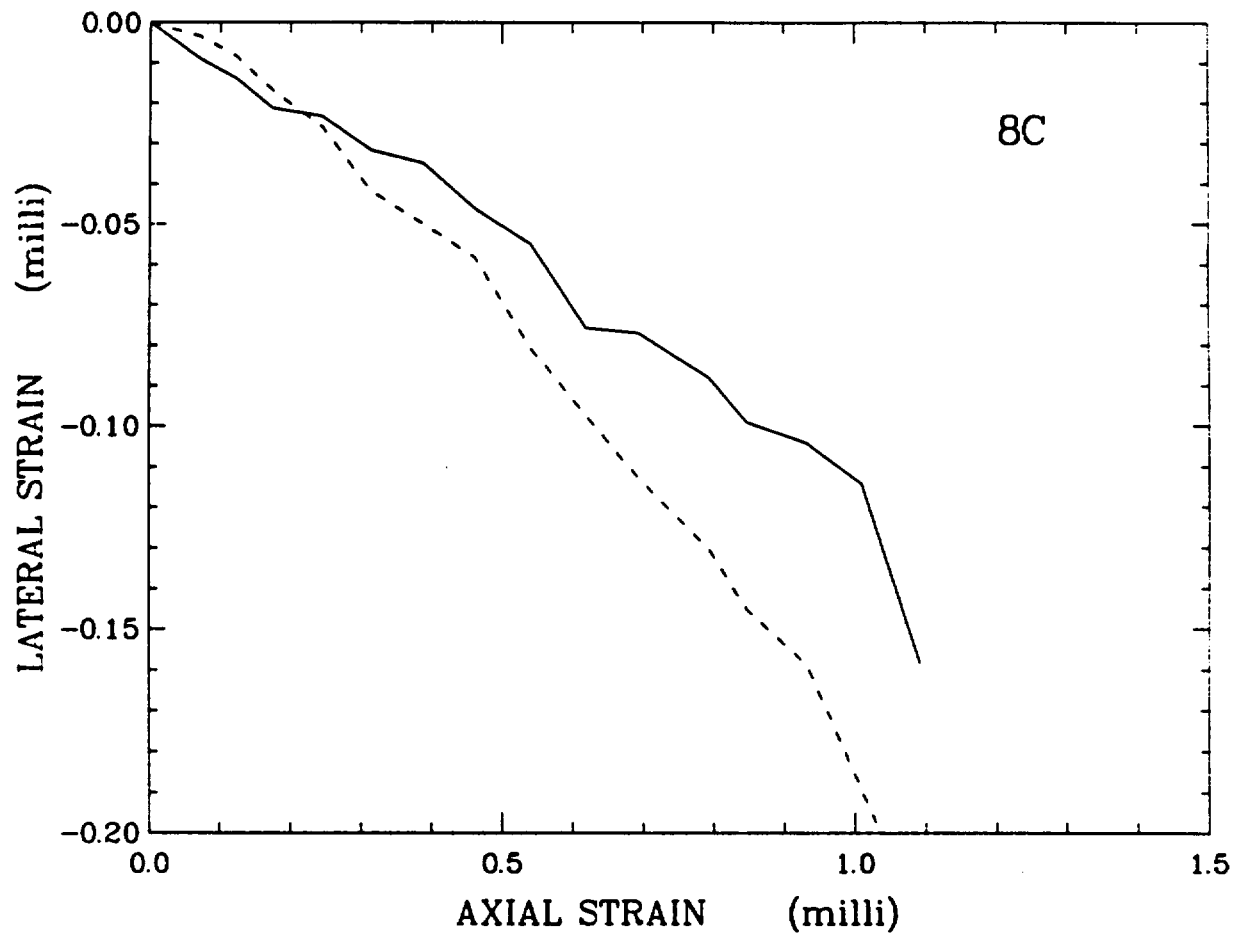


Figure D-3G.

Lateral strain-axial strain curve for saturated sample 8C deformed in compression at atmospheric confining pressure, room temperature and a nominal strain rate of 10^{-5} s^{-1} .

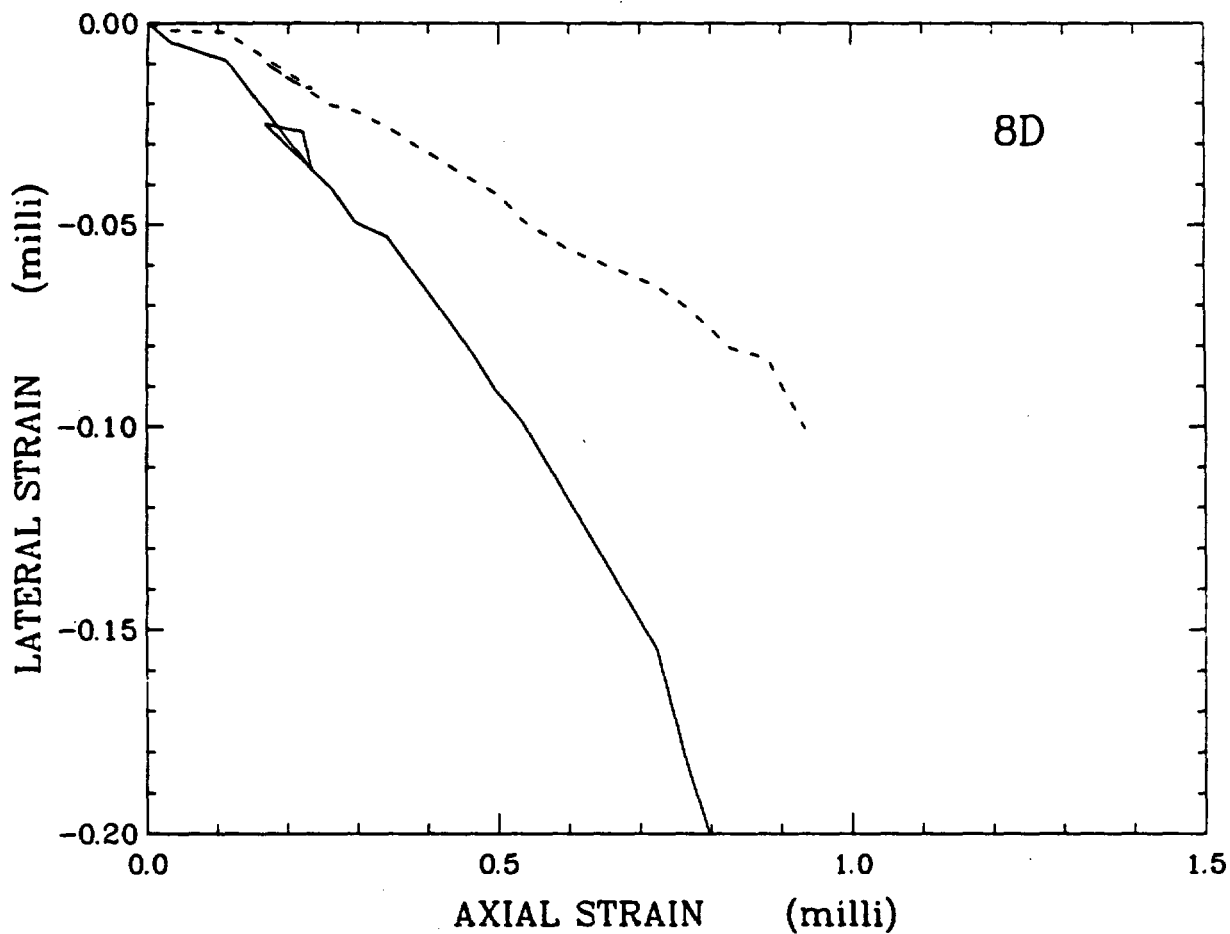


Figure D-3H.

Lateral strain-axial strain curve for saturated sample 8D deformed in compression at atmospheric confining pressure, room temperature and a nominal strain rate of 10^{-6} s^{-1} .

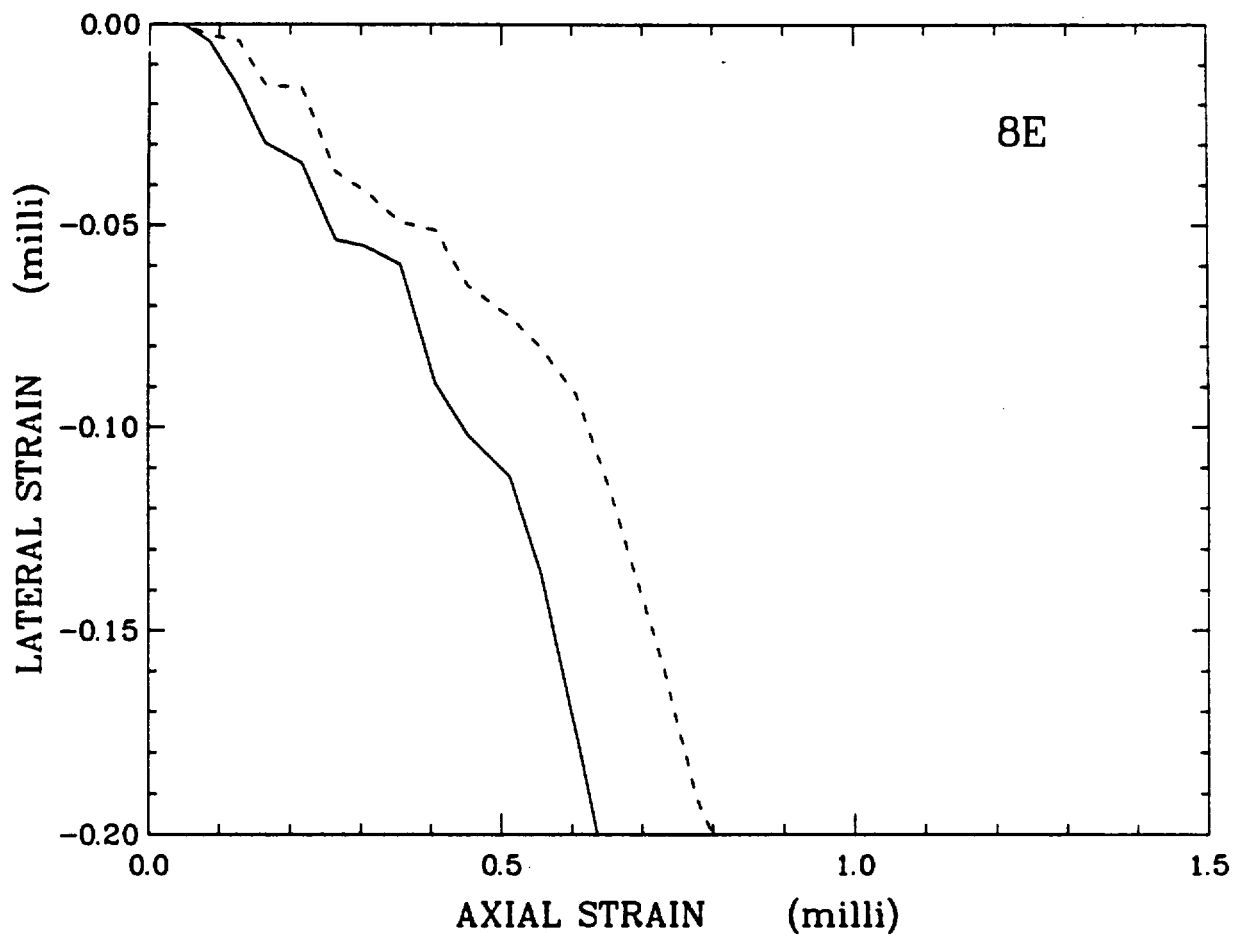


Figure D-3I.

Lateral strain-axial strain curve for saturated sample 8E deformed in compression at atmospheric confining pressure, room temperature and a nominal strain rate of 10^{-5} s^{-1} .

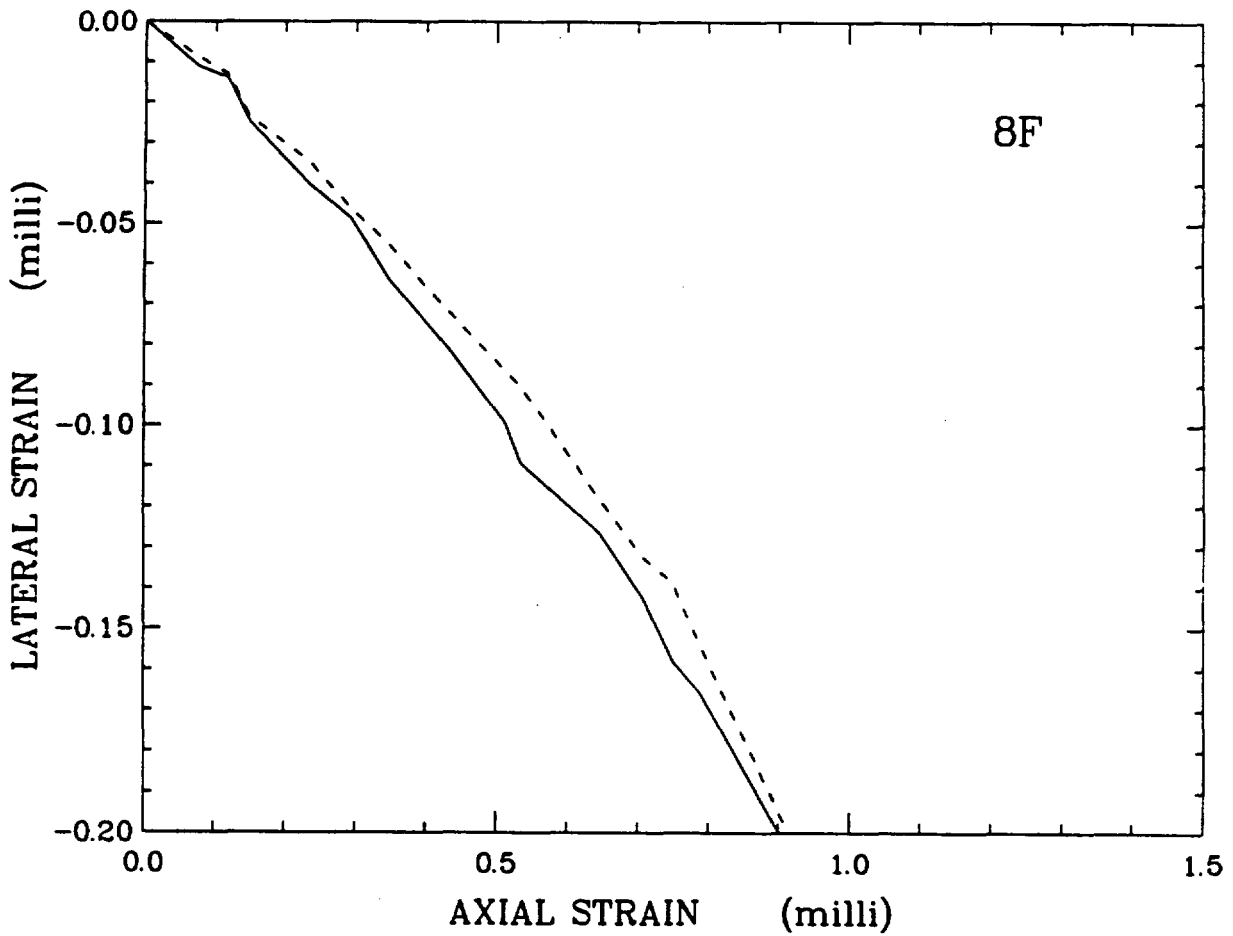


Figure D-3J.

Lateral strain-axial strain curve for saturated sample 8F deformed in compression at atmospheric confining pressure, room temperature and a nominal strain rate of 10^{-6} s^{-1} .

Distribution List

B. C. Rusche, Director (RW-1)
Office of Civilian Radioactive Waste Management
U. S. Department of Energy
Forrestal Building
Washington, D. C. 20585

J. W. Bennett (RW-22)
Office of Geologic Repositories
U. S. Department of Energy
Forrestal Building
Washington, D. C. 20585

R. Stein (RW-23)
Office of Geologic Repositories
U. S. Department of Energy
Forrestal Building
Washington, D. C. 20585

J. J. Fiore (RW-22)
Program Management Division
Office of Geologic Repositories
U. S. Department of Energy
Forrestal Building
Washington, D. C. 20585

M. W. Frei (RW-23)
Engineering & Licensing Division
Office of Geologic Repositories
U. S. Department of Energy
Forrestal Building
Washington, D. C. 20585

E. S. Burton (RW-25)
Siting Division
Office of Geologic Repositories
U. S. Department of Energy
Forrestal Building
Washington, D. C. 20585

C. R. Cooley (RW-24)
Geosciences & Technology Division
Office of Geologic Repositories
U. S. Department of Energy
Forrestal Building
Washington, D. C. 20585

D. C. Newton (RW-23)
Engineering & Licensing Division
Office of Geologic Repositories
U. S. Department of Energy
Forrestal Building
Washington, D. C. 20585

T. P. Longo (RW-25)
Program Management Division
Office of Geologic Repositories
U. S. Department of Energy
Forrestal Building
Washington, D. C. 20585

J. O. Neff
Salt Repository Project Office
U. S. Department of Energy
505 King Avenue
Columbus, OH 43201

S. A. Mann, Manager
Crystalline Rock Project Office
U. S. Department of Energy
9800 South Cass Avenue
Argonne, IL 60439

R. J. Blaney (RW-22)
Program Management Division
Office of Geologic Repositories
U. S. Department of Energy
Forrestal Building
Washington, D. C. 20585

R. W. Gale (RW-40)
Office of Policy, Integration, and Outreach
U. S. Department of Energy
Forrestal Building
Washington, D. C. 20585

J. E. Shaheen (RW-44)
Outreach Programs
Office of Policy, Integration, and Outreach
U. S. Department of Energy
Forrestal Building
Washington, D. C. 20585

C. Klingsberg (RW-24)
Geosciences & Technology Division
Office of Geologic Repositories
U. S. Department of Energy
Forrestal Building
Washington, D. C. 20585

Chief, Repository Projects Branch
Division of Waste Management
U. S. Nuclear Regulatory Commission
Washington, DC 20555

NTS Section Leader
Repository Projects Branch
Division of Waste Management
U. S. Nuclear Regulatory Commission
Washington, DC 20555

B. G. Gale (RW-25)
Siting Division
Office of Geologic Repositories
U. S. Department of Energy
Forrestal Building
Washington, D. C. 20585

O. L. Olson, Manager
Basalt Waste Isolation Project Office
U. S. Department of Energy
Richland Operations Office
Post Office Box 550
Richland, WA 99352

D. L. Vieth, Director (4)
Waste Management Project Office
U. S. Department of Energy
Post Office Box 14100
Las Vegas, NV 89114

D. F. Miller, Director
Office of Public Affairs
U. S. Department of Energy
Post Office Box 14100
Las Vegas, NV 89114

D. A. Nowack (14)
Office of Public Affairs
U. S. Department of Energy
Post Office Box 14100
Las Vegas, NV 89114

B. W. Church, Director
Health Physics Division
U. S. Department of Energy
Post Office Box 14100
Las Vegas, NV 89114

Document Control Center
Division of Waste Management
U. S. Nuclear Regulatory Commission
Washington, DC 20555

P. T. Prestholt
NRC Site Representative
1050 East Flamingo Road
Suite 319
Las Vegas, NV 89109

K. Street, Jr.
Lawrence Livermore National Laboratory
Post Office Box 808
Mail Stop L-209
Livermore, CA 94550

L. D. Ramspott (3)
Technical Project Officer for NNWSI
Lawrence Livermore National Laboratory
Post Office Box 808
Mail Stop L-204
Livermore, CA 94550

W. J. Purcell (RW-20)
Office of Geologic Repositories
U. S. Department of Energy
Forrestal Building
Washington, D. C. 20585

D. T. Oakley (3)
Technical Project Officer for NNWSI
Los Alamos National Laboratory
Post Office Box 1663
Mail Stop F-671
Los Alamos, NM 87545

W. W. Dudley, Jr. (4)
Technical Project Officer for NNWSI
U. S. Geological Survey
Post Office Box 25046
418 Federal Center
Denver, CO 80225

V. M. Glanzman
U. S. Geological Survey
Post Office Box 25046
913 Federal Center
Denver, CO 80225

J. B. Wright
Technical Project Officer for NNWSI
Westinghouse Electric Corporation
Waste Technology Services Division
Nevada Operations
Post Office Box 708
Mail Stop 703
Mercury, NV 89023

M. E. Spaeth
Technical Project Officer for NNWSI
Science Applications International, Corp.
2769 South Highland Drive
Las Vegas, NV 89109

SAI-T&MSS Library (2)
Science Applications International, Corp.
2950 South Highland Drive
Las Vegas, NV 89109

W. S. Twenhofel, Consultant
Science Applications International, Corp.
820 Estes Street
Lakewood, CO 80215

H. D. Cunningham, General Manager
Reynolds Electrical & Engineering Company, Inc.
Post Office Box 14400
Mail Stop 555
Las Vegas, NV 89114

A. E. Gurrola, General Manager
Energy Support Division
Holmes & Narver, Inc.
Post Office Box 14340
Las Vegas, NV 89114

J. A. Cross, Manager
Las Vegas Branch
Fenix & Scisson, Inc.
Post Office Box 15408
Las Vegas, NV 89114

Dr. M. Miffin
Desert Research Institute
Water Resources Center
Suite 201
1500 East Tropicana Avenue
Las Vegas, NV 89109

C. H. Johnson, Technical Program Manager
Nuclear Waste Project Office
State of Nevada
Capitol Complex
Carson City, NV 89710

J. Fordham
Desert Research Institute
Water Resources Center
Post Office Box 60220
Reno, NV 89506

**T. Hay, Executive Assistant
Office of the Governor
State of Nevada
Capitol Complex
Carson City, NV 89710**

**R. R. Loux, Jr., Director (8)
Nuclear Waste Project Office
State of Nevada
Capitol Complex
Carson City, NV 89710**

**Department of Comprehensive Planning
Clark County
225 Bridger Avenue, 7th Floor
Las Vegas, NV 89155**

**Lincoln County Commission
Lincoln County
Post Office Box 90
Pioche, NV 89043**

**Community Planning and Development
City of North Las Vegas
Post Office Box 4086
North Las Vegas, NV 89030**

**Planning Department
Nye County
Post Office Box 153
Tonopah, NV 89049**

**Economic Development Department
City of Las Vegas
400 East Stewart Avenue
Las Vegas, NV 89101**

**N. E. Carter
Battelle Columbus Laboratory
Office of Nuclear Waste Isolation
505 King Avenue
Columbus, OH 43201**

**ONWI Library (2)
Battelle Columbus Laboratory
Office of Nuclear Waste Isolation
505 King Avenue
Columbus, OH 43201**

**W. M. Hewitt, Program Manager
Roy F. Weston, Inc.
2301 Research Blvd., 3rd. Floor
Rockville, MD 20850**

**Dr. N. L. Carter, Director
Center for Tectonophysics
Texas A&M University
College Station, TX 77843**

**RE/SPEC, Inc. (2)
Post Office Box 725
Rapid City, SD 57701
Attention:
P. F. Gnirk
P. E. Senseny**

**RE/SPEC, Inc. (2)
Post Office Box 14984
Albuquerque, NM 87191
Attention:
S. W. Key
D. K. Parrish**

**R. Coppage, Senior Mining Engineer
Fenix & Scisson, Inc.
Post Office Box 498
Mercury, NV 89023**

**Christopher Barton
U. S. Geological Survey
Post Office Box 327
Mercury, NV 89023**

**Eric Larsen
Fenix & Scisson Geology Building
Post Office Box 498
Mercury, NV 89023**

**J. R. Connolly and K. Keil (25)
Department of Geology
Institute of Meteoritics
University of New Mexico
Albuquerque, NM 87131**

1510 J. W. Nunziato
1520 D. J. McCloskey
1521 R. D. Krieg
1524 K. W. Schuler
1524 W. W. Sullivan
1530 L. W. Davison
1534 J. R. Asay
1540 W. C. Luth
1541 H. C. Hardee
1542 B. M. Butcher
1542 L. S. Costin
1542 D. J. Holcomb
1542 W. A. Olsson
1542 R. H. Price (25)
1542 S. J. Spence (2)
1542 L. W. Teufel
1542 W. R. Wawersik
1542 D. H. Zeuch
1543 T. M. Gerlach
3141 C. M. Ostrander (5)
3151 W. L. Garner (3)
3154-3 C. H. Dalin (28)
6300 R. W. Lynch
6310 T. O. Hunter
6311 L. W. Scully
6311 L. Perrine (2)
6312 F. W. Bingham
6312 B. S. Langkopf
6313 F. B. Nimick (20)
6313 B. M. Schwartz (2)
6313 R. M. Zimmerman
6314 S. J. Bauer
6314 B. L. Ehgartner
6314 L. M. Ford
6314 A. J. Mansure
6314 J. R. Tillerson (15)
6330 NNWSICF
6332 WMP Library
6430 N. R. Ortiz
7417 F. L. McFarling
8424 M. A. Pound